# The Multipole Description of Complex Plasmonic Nanostructures

Dissertation zur Erlangung des akademischen Grades
*doctor rerum naturalium (Dr. rer. nat.)*

vorgelegt dem Rat der Physikalisch-Astronomischen Fakultät
der Friedrich-Schiller-Universität Jena

von Dipl.-Phys. Jörg Petschulat
geboren am 12.02.1981 in Zwickau.

*For Nadja and Mathilde.*

# Contents

# 1 Introduction

The peculiarities of the interaction of light with confined metal inclusions have been of interest for a long time. The most prominent examples are the coloring effects achieved by certain noble metals included in windows in churches[1]. The theoretical description of such effects has been performed by *G. Mie* [Mie08]. Furthermore, the theoretical prediction of bound electromagnetic modes at metal dielectric interfaces by *R. H. Ritchie* [Rit57] comprises another important milestone. In the following decades many interesting applications have been investigated, e.g., extra-ordinary transmission of light through metal films perforated with holes of sub-wavelength dimensions [ELG+98, BDE03].

During the last years, the subject of light-matter interaction with metal objects of sub-wavelength size has been experienced further interest [BFL+07, Ram05, Sha07]. The reasons for this development are manyfold. On one side the fabrication processes have been continuously improved due to the growing demands for smaller circuit sizes in the semiconductor industry. Among other fabrication schemes, mostly *top-down* approaches[2], such as electron beam lithography, have successfully been applied to realize highly reproducible structures covering large areas. Thus, versatile fabrication methods have been established to provide structures with feature sizes far below the wavelength of optical radiation. On the other side, the classical electrodynamic description of light-matter interaction with arbitrarily-shaped objects got enriched by the exploration and application of powerful numerical techniques. These methods allow the verification of experimental findings in the same manner as new effects can be predicted and finally observed in application-oriented realizations of specific structures. Moreover, the numerical methods are valuable tools to bridge the gap between the physics, taking place at the scale of nanometers, and the macroscopic observation.

The dramatical developments in these two fields provided the optimal breeding ground for the emerging field of *metamaterials*. Eventually, everything that was required to launch this topic was a *physical idea*.

Exactly this idea was presented in the work of *J. B. Pendry* in 1999 [PHRS99]. He proposed the concept of artificial materials, i.e., *metamaterials*[3], that are composed of *sub-wavelength structures*, acting similarly as atoms and molecules do in ordinary matter. These structures were termed *metamolecules* and have in common that their dimensions are much smaller than the wavelength of the impinging radiation. Thus, in a simplified picture, the illumination cannot resolve the structural details and behaves like in an effective medium with propagation

---

[1]The *Lycurcus Cup*, exposed in the British museum in London, is a frequently referred example for its different color appearance depending on the illumination conditions.

[2]The term *top-down* accounts for fabrication schemes for which the entire structure is created starting from a predefined arrangement, e.g., a stack of layers, that is finally processed, typically by electron or ion beam lithography. Differently, *bottom-up* approaches denote schemes that are starting with entities at a smaller scale than the final structure. Examples are chemical synthesis of gold spheres and other self-organized fabrication schemes.

[3]The term *metamaterial* originates from the greek word "meta" which can be translated by "beyond". Hence, the expression metamaterials should account for materials beyond the capabilities of natural matter.

properties dictated by the elementary metamolecules. These metamolecules, similar to ordinary matter, predominantly interact with electromagnetic waves by their carriers. In contrast to ordinary matter, for which the carrier dynamics is determined by the atomic assembly of the respective element, the carrier dynamics can be tailored by the geometry of the metamolecules in metamaterials. Due to their high electron density and mobility, noble metals such as gold or silver are typically selected as composite materials for metamolecules. The associated resonant carrier excitations are so-called *localized surface plasmon-polaritons* that can be controlled by adjusting the shape and the composition of the metamolecule. As it may be anticipated from the terminology, such excitations are located at the surface of the respective metamolecule, due to the limited penetration depth in the metal on the one side and an evanescent decay in the ambient dielectric medium on the other side. Furthermore, they are *hybrid excitations*, since the electron dynamics (*plasmon*) induces an electric field (*polariton*) and *vice versa*. With these considerations it becomes clear that a resonance in the carrier dynamics is accompanied with a resonant and thus enhanced local electromagnetic field in the vicinity of the structure.

In contrast to the research associated with metamaterials, localized surface plasmon-polaritons have been known for a long time. A famous and fundamental theoretical description related to such resonances is the work published by *G. Mie* [Mie08] which has been already mentioned above. Although *Mie* did not use the terminology of localized surface plasmon-polaritons, he developed a rigorous electrodynamic formalism to solve the scattering problem of electromagnetic waves at isolated spheres with arbitrary diameter and composition. With this approach he was able to predict the resonances occurring in the scattering spectra of colloidal gold solutions. These resonances have been observed in the form of coloring effects mentioned in the beginning.

Hence, the physics of metal structures with sub-wavelength dimensions has been known for decades and was subject of intense investigations. The dramatic new feature of structures that are typically investigated in the field of metamaterials is the possibility to additionally create a magnetic response besides the electrical one. Exactly this intriguing difference can be considered as the major achievement during the last years, since metamaterials can exhibit *optical magnetism*, i.e., magnetic light-matter interaction at optical frequencies [PHRS99]. Such an effective magnetic response has never been observed in natural matter before and opens the gate to alter both, the magnetic and the electric properties for light propagation by structured materials with an unprecedented diversity.

Among other famous works which investigated a potential magnetic response there is one publication that is of particular importance in the field of metamaterials. This work has been presented by *V. G. Veselago* [Ves68, Boa11] who theoretically investigated what impact a potential magnetic response would have early in 1968. As the most important consequence, *Veselago* considered the case of a *negative refractive index* [Ves68]. However, only in combination with the structures and the concepts proposed by *Pendry*, realizations of such effects became feasible [BdWPA10, DWSL07, SCC+05, VZZ+08].

Although the ability to create a magnetic response in addition to the electrical seems to

be only an incremental development, the consequences of such an apparently slight change are enormous. For instance, the resolution limit of *E. Abbe* [Abb73], which is approximately one half of the irradiating wavelength, can be circumvented by *perfect lenses* [Pen00, SE06, JAN06]. Recently, much smaller details have been resolved with the use of metamaterials [LLX$^+$07, SHD07]. Finally, the fascinating concept of *cloaking*[4] shall be mentioned which is also related to the control of electric and magnetic properties of electromagnetic waves in metamaterials [Leo06, SMJ$^+$06, NMMB07].

## Motivation

During the last years of metamaterial research significant progress has been made in altering the propagation properties of electromagnetic fields, see, e.g., the above-mentioned examples. For this purpose mainly numerical methods have been established to design the metamolecules of the metamaterial exhibiting the desired functionality. In turn, the underlying physics for the realized functionality is quite often explained in a phenomenological manner. A frequently applied explanation originates from the circuit theory which deals with $LC$-circuits possessing a magnetic inductance $L$ and an electric response due to the capacitance $C$ [AE06, BFL$^+$07]. Indeed, the early metamaterials with a magnetic response were based on such considerations [SPV$^+$00, SSS01]. A second possibility to explain magnetic effects at optical frequencies is that microscopic ring currents are induced creating a magnetic dipole moment [SFVK09, LLZG09]. These microscopic magnetic moments give rise to a macroscopic magnetization, i.e., an effective magnetic permeability. The description on the basis of such multipole moments is much more related to the understanding of nanostructures that had been developed before metamaterials were explored. It immediately allows to apply standard textbook knowledge, i.e., the electrodynamic multipole expansion, and thus gives physicists a clear picture of the underlying microscopic and macroscopic mechanisms. Furthermore, it is the consequent advancement from the description of nanostructures operating in the first-order, i.e., the electric dipole, regime. Therefore, the sub-wavelength objects are described by a microscopic electric dipole moment giving rise to a macroscopic polarizability. For such understanding, analytical models have already been developed which allow the prediction of the ensemble response.

## Scope of this work

The scope of this work is to include the electric and the magnetic response of metamaterials in a unified description of metamolecules. As will be shown, this can be performed by a multipole expansion, taking into account multipole moments up to second-order. For this reason, a carrier ansatz will be applied to account for the microscopic dynamics of the metal's free charges inside each metamolecule. This microscopic formalism is similar to the description of atomic lattices in solid state physics where a set of coupled oscillators is applied as a first approximation. By describing the carrier dynamics of a metamolecules with such a set of

---

[4]The term *cloaking* is used to describe the guiding of electromagnetic fields around an object which does not interact with the light and thus, remains undetectable, i.e., *cloaked*.

oscillators, the oscillation eigenmodes can be directly related to the localized eigenmodes of the respective metamolecule. Moreover, the explicit knowledge of the carriers' motions immediately allows the application of the multipole expansion. With this step, the microscopic properties, i.e., the oscillation eigenmodes of the isolated metamolecule, will be translated into macroscopic properties, such as the dispersion relation and the effective material parameters. Hence, metamolecules will be considered, whose interaction with light can be conceptually reduced to the excitation of multipole moments. A necessary condition for such an approach is that the metamolecule, i.e., the metamaterial's building blocks, are represented by isolated objects for which a multipole expansion is meaningful. For metamaterials whose functionality originates from extended or connected building blocks this expansion up to the second order might not be sufficient at all. A prototypical and decisive metamaterial with such building blocks is the *double fishnet structure* [ZFM+05, ZFP+05].

The analysis in this work will be focussed on the properties of localized two- and three-dimensional metamolecules. Therefore this work is organized as follows. At first, a brief summary of experimental and theoretical basics, applied in this work, will be given. The most important routine mentioned therein is the *averaging procedure*, i.e., the transition from the microscopic Maxwell's equations to their macroscopic representation. Within the averaging procedure, the role of multipolar moments will be stressed. In addition, this known approach will be discussed in the context of metamolecules in contrast to natural molecules for which the averaging process is applied in ordinary matter [Jac75, Rus70]. With this concept it is possible to connect isolated metamolecules with the optical response of the entire metamaterial. In the following parts, this work is conceptually organized similar to the multipole expansion itself.

Hence, in part 3 metamolecules will be considered in the electric dipole regime. The optical properties of dipole nanostructures that are relevant for this work will be examined, i.e., the near-field enhancement as well as the excitation conditions in terms of the incident polarization. Furthermore, it will be shown how ensemble properties, i.e., effective material parameters, can be controlled with particular arrangements of such dipole nanostructures which finally allows for the simultaneous excitation of another class of plasmonic excitations, i.e., *propagating surface plasmon polaritons*. Moreover, the experimental verification of numerically predicted optical far-field properties for such arrangements will be performed by applying far-field spectroscopy in this part. Finally, it will be shown how the fabricated samples can be applied to improve the *Surface-Enhanced Raman Scattering* of adsorbed chemical analytes. The simultaneous excitation of a localized surface plasmon-polariton at the excitation frequency and a propagating surface plasmon-polariton at the detected Stokes frequency represents a novel approach for improved Surface-Enhanced Raman Scattering substrates.

In part 4 metamaterials displaying the before-mentioned electric *and* magnetic response will be considered. Examples for metamaterials operating in the linear optical regime will be investigated firstly. Furthermore, the oscillator equations will be prepared to account for *conductively* as well as *capacitively* coupled metamolecules, e.g., the *split-ring resonator* [LEW+04] and the *cut-wire* metamolecule [SZO01], respectively. Next, the transition from metamaterials with linearly polarized eigenstates toward elliptically polarized eigenstates will

be performed. Due to the symmetry of the metamolecules, the metamaterials investigated up to this point display solely linearly polarized eigenstates. Hence, particular modifications on the metamolecules will be performed to break these symmetries which again can be described by the microscopic oscillator approach. As will be shown, the macroscopic response obtained by the multipole expansion shows elliptically polarized eigenstates. As a consequence, asymmetric transmission for circularly polarized light can be observed. Furthermore, it will be shown that the far-field reflection and transmission coefficients for the modified metamolecules can be predicted on the basis of the metamolecules' properties before the modification that comprise linearly polarized eigenstates.

Since second-order multipole moments are also accompanied with *nonlinear* optical properties, multipole-induced nonlinear effects will be the subject of this part as well. As an example, the *second-harmonic generation* will be investigated. The quadratic nonlinear properties associated with the appearance of second-order multipoles are shown to be consistent with the structural nonlinearities predicted by another approach applied in metamaterial research, i.e., the *hydrodynamic theory of electrons* [FLK+08, ZHL+09].

Finally, the electromagnetic near-fields of individual metamolecules will be rigorously decomposed into their multipolar components. This final step will prove that the applied description of metamaterials in terms of multipole moments holds for ensembles of metamolecules in the same manner as for the individual ones.

Lastly, all results collected in this work will be summarized and potential perspectives will be given.

# 2 Theoretical and experimental basics

## 2.1 Theory

Throughout this chapter essential mathematical techniques describing the physics of light interaction with metal nanostructures in the framework of classical electrodynamics are reviewed. The fundamental set of equations spanning the entire physical space of observable phenomena investigated in this work is formed by microscopic and macroscopic Maxwell's equations. More specifically this fundamental set of equations can be solved numerically as well as analytically for the case of light interaction with nanoparticles incorporating approximations that will be discussed herein. The detailed investigation of both procedures will allow for a correct and physically thorough theoretical investigation of light interaction processes of metal nanostructures in the following chapters.

### 2.1.1 Averaging microscopic Maxwell's equations - the role of multipole moments

Microscopic Maxwell's equations represent the fundamental set of linear differential equations connecting the electromagnetic vector fields to microscopic carrier and current densities[1]

$$\nabla \times \mathfrak{E}(\mathbf{r}, t) + \frac{\partial}{\partial t} \mathfrak{B}(\mathbf{r}, t) = 0, \tag{2.1}$$

$$\nabla \times \mathfrak{B}(\mathbf{r}, t) - \frac{1}{c^2} \frac{\partial}{\partial t} \mathfrak{E}(\mathbf{r}, t) = \mu_0 \mathfrak{j}(\mathbf{r}, t), \tag{2.2}$$

$$\nabla \cdot \mathfrak{B}(\mathbf{r}, t) = 0, \tag{2.3}$$

$$\nabla \cdot \mathfrak{E}(\mathbf{r}, t) = \frac{1}{\epsilon_0} \mathfrak{r}(\mathbf{r}, t). \tag{2.4}$$

In Eqs.(2.1-2.4) $\mathfrak{E}(\mathbf{r}, t)$ and $\mathfrak{B}(\mathbf{r}, t)$ represent the electric field and the magnetic induction, whereas $\mathfrak{j}(\mathbf{r}, t)$ and $\mathfrak{r}(\mathbf{r}, t)$ account for the microscopic current and charge density, respectively. These equations can be applied to describe the electromagnetic fields emitted and absorbed upon temporal and spatial current and carrier dynamics. Moreover, the fields themselves react on the carriers and currents again. The electromagnetic force acting on a particular carrier distribution of $N$ charges $q_l$ located at $\mathbf{r}_l$ is described by the important connection of mechanics and electrodynamics: the Lorenz force

$$\mathbf{F}(t) = \sum_{l=1}^{N} q_l \left[ \mathfrak{E}(\mathbf{r}_l, t) + \frac{\partial}{\partial t} \mathbf{r}_l \times \mathfrak{B}(\mathbf{r}_l, t) \right] = \sum_{l=1}^{N} \left[ q_l \mathfrak{E}(\mathbf{r}_l, t) + \mathfrak{j}_l \times \mathfrak{B}(\mathbf{r}_l, t) \right]. \tag{2.5}$$

---

[1]Here the differential form of Maxwell's equations has been selected, since solely this representation will be applied for numerical techniques and analytical models in the following sections.

Hence, the Lorenz force (2.5) can be considered as the *microscopic constitutive relation* or *material equation*, since it represents the physical connection between media, in terms of carriers (with the charge $q_l$) or currents ($j_l$), and electromagnetic fields. Combining Eq.(2.5) and Eqs.(2.1-2.4) the interaction of incident electromagnetic fields with a carrier distribution of $N$ charges becomes a self-consistent many-particle task.

In order to overcome this mathematical burden for electromagnetic field interaction with objects consisting of large numbers of carriers and the numerous interactions among themselves, *microscopic* Maxwell's equations can be averaged yielding *macroscopic* Maxwell's equations

$$\nabla \times \mathbf{E}(\mathbf{r},t) + \frac{\partial}{\partial t}\mathbf{B}(\mathbf{r},t) = 0, \tag{2.6}$$

$$\nabla \times \mathbf{H}(\mathbf{r},t) - \frac{\partial}{\partial t}\mathbf{D}(\mathbf{r},t) = \mathbf{j}(\mathbf{r},t), \tag{2.7}$$

$$\nabla \cdot \mathbf{B}(\mathbf{r},t) = 0, \tag{2.8}$$

$$\nabla \cdot \mathbf{D}(\mathbf{r},t) = \rho(\mathbf{r},t). \tag{2.9}$$

Comparing Eqs.(2.1-2.4) with Eqs.(2.6-2.9) the homogeneous equations (2.1,2.3,2.6,2.8 as well as the inhomogeneous equations (2.2,2.4,2.7,2.9) remain formally invariant. However, in contrast to the microscopic representation the *microscopic* variables $\mathfrak{E}, \mathfrak{B}, \mathfrak{r}$, and $\mathfrak{j}$ have been replaced by the *averaged* or *macroscopic* observables $\mathbf{E}$, $\mathbf{B}$, $\rho$, and $\mathbf{j}$ and amended by two new variables: the *electric displacement* $\mathbf{D}$ and the *magnetic field* $\mathbf{H}$. This averaging procedure is discussed in detail in Refs. [MN53, Jac75]. The principle idea of this procedure is that the microscopic fields, currents and charge densities can be averaged in order to describe electric field interactions on a macroscopic scale, e.g., in optical and plasmonic systems. It turns out to be sufficient to carry out this averaging procedure only spatially rather than spatio-temporally. There are two frequently applied arguments for that. First, the atomic time scales for nuclear vibrations ($10^{-13}$ s) and for electron motion ($10^{-17}$ s) are already in the same order compared with optical light cycles ($\lambda = 550$ nm $\rightarrow T = 1.83 \cdot 10^{-15}$s) making an averaging inappropriate. Second, these temporal fluctuations occur in an uncorrelated manner over the typical averaging distances. Hence, the dominant time dependence is mainly dictated by the frequency components of the incident light, whereas the spatial carrier distribution is washed out for averaging volumes investigated herein, which are in the order of $> (10 \text{ nm})^3$.

At this stage it shall be mentioned that this situation changes if ultra-short light pulses are interacting with matter. Thereby the temporal excitation can resolve or even be below the time scales of electron and nuclear dynamics. Thus, the isolated temporal dynamics of the molecule becomes important. Since in such experiments very diluted gases or even single molecules or ions are illuminated the spatial averaging becomes meaningless. Beyond such limitations of ultra-short light-matter interactions the averaging procedure is adequate and well-established for the description of electrodynamic interactions with condensed matter nanostructures, i.e., metals or dielectrics, at optical frequencies.

In order to quantify the above-mentioned restrictions a gold nanoparticle will be considered

in the following to motivate the averaging procedure for the case of nanostructures. Starting with a nanosphere radius of $R = 5$ nm the associated sphere volume is $V_{\text{sphere}} = 4\pi R^3/3 = 523.6$ nm$^3$. The known radius of a gold atom [Sla64] is $R_{\text{Au}} = (135 \pm 5) \cdot 10^{-3}$ nm yielding an atomic volume of $V_{\text{atom}} = 4\pi R_{\text{Au}}^3/3 = 0.0103$ nm$^3$. Assuming highest sphere packing density of $\approx 0.74$ the gold sphere comprises an estimated number of $0.74 \cdot V_{\text{sphere}}/V_{\text{atom}} \approx 3.8 \cdot 10^4$ atoms, a too large number for a microscopic analysis. This consideration shows that even tiny nanostructures, typical structures are larger than the example discussed here, contain a considerable amount of carriers making a macroscopic description desirable.

In the following the main steps of the spatial averaging of matter are re-examined in order to reveal the role of multipole moments in the transition from the microscopic to the macroscopic representation, an important routine that will be applied for various nanostructures throughout this work. Afterwards the peculiarities occurring for ensembles of nanostructures as well as similarities to a historical approach are discussed. For this purpose the notation of G. Russakoff is recapitulated [Rus70, Jac75]. Spatial averaging of any temporally and spatially dependent function can be expressed as the convolution with the test function $G(\mathbf{r})$ [Yan66]

$$\langle \psi(\mathbf{r}, t) \rangle = \int_{\mathbb{R}^3} d^3\mathbf{r}' \psi(\mathbf{r} - \mathbf{r}', t) G(\mathbf{r}'). \tag{2.10}$$

The test function $G(\mathbf{r})$ can be arbitrarily chosen with the restriction that it is normalized to unity. For the case of the nanosphere example from above the test function could be

$$G(\mathbf{r}) = \begin{cases} \frac{3}{4\pi R^3}, & \forall |\mathbf{r}| < R, \\ 0, & \forall |\mathbf{r}| > R. \end{cases} \tag{2.11}$$

Applying the averaging [Eq.(2.10)] to time and space derivatives for continuously differentiable functions $\psi(\mathbf{r}, t)$ yields

$$\frac{\partial}{\partial \mathbf{r}_i} \langle \psi(\mathbf{r}, t) \rangle = \left\langle \frac{\partial}{\partial \mathbf{r}_i} \psi(\mathbf{r}, t) \right\rangle, \tag{2.12}$$

$$\frac{\partial}{\partial t} \langle \psi(\mathbf{r}, t) \rangle = \left\langle \frac{\partial}{\partial t} \psi(\mathbf{r}, t) \right\rangle. \tag{2.13}$$

Thus, the electric field $\mathfrak{E}(\mathbf{r}, t)$ and the magnetic induction $\mathfrak{B}(\mathbf{r}, t)$ can be straightforwardly rewritten applying the respective averaged quantities. The homogeneous microscopic equations (2.1,2.3) then read as

$$\nabla \times \langle \mathfrak{E}(\mathbf{r}, t) \rangle + \frac{\partial}{\partial t} \langle \mathfrak{B}(\mathbf{r}, t) \rangle = 0, \tag{2.14}$$

$$\nabla \cdot \langle \mathfrak{B}(\mathbf{r}, t) \rangle = 0, \tag{2.15}$$

which can be transformed into macroscopic equations (2.6,2.8) by substituting

$$\langle \mathfrak{E}(\mathbf{r}, t) \rangle = \mathbf{E}(\mathbf{r}, t), \tag{2.16}$$

$$\langle \mathfrak{B}(\mathbf{r}, t) \rangle = \mathbf{B}(\mathbf{r}, t). \tag{2.17}$$
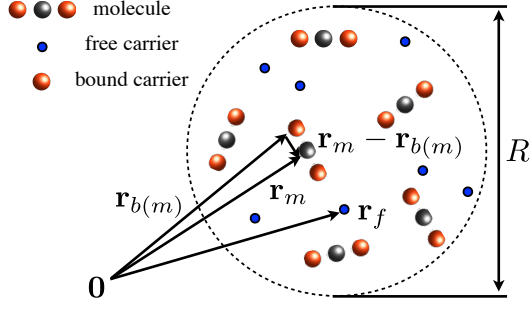
**Figure 2.1:** Sketch of the averaging volume embedding *bound* (molecules) as well as *free* (electrons and ions) carriers.

The remaining inhomogeneous equations

$$\nabla \times \langle \mathfrak{B}(\mathbf{r}, t) \rangle - \frac{1}{c^2} \frac{\partial}{\partial t} \langle \mathfrak{E}(\mathbf{r}, t) \rangle = \mu_0 \langle \mathbf{j}(\mathbf{r}, t) \rangle, \tag{2.18}$$

$$\nabla \cdot \langle \mathfrak{E}(\mathbf{r}, t) \rangle = \frac{1}{\epsilon_0} \langle \mathfrak{r}(\mathbf{r}, t) \rangle, \tag{2.19}$$

contain next to the averaged macroscopic fields $\mathbf{E}(\mathbf{r}, t)$, $\mathbf{B}(\mathbf{r}, t)$ also the averaged current $\langle \mathbf{j}(\mathbf{r}, t) \rangle$ and charge $\langle \mathfrak{r}(\mathbf{r}, t) \rangle$ densities that have to be considered in detail. Applying the averaging procedure [Eq.(2.10)] to the charge density $\mathfrak{r}(\mathbf{r}, t)$ one obtaines

$$\langle \mathfrak{r}(\mathbf{r}, t) \rangle = \int_{\mathbb{R}^3} d^3\mathbf{r}' \mathfrak{r}(\mathbf{r} - \mathbf{r}', t) G(\mathbf{r}'). \tag{2.20}$$

Any microscopic carrier distribution corresponding to a realistic natural material may then be separated into two contributions: *bound* and *free* carriers, see Fig.2.1. Both can be considered as point charges in the form of

$$\mathfrak{r}(\mathbf{r}, t) = \mathfrak{r}_{\text{bound}}(\mathbf{r}, t) + \mathfrak{r}_{\text{free}}(\mathbf{r}, t) \tag{2.21}$$

$$= \sum_{m=1}^{N_{\text{molecules}}} \sum_{b(m)=1}^{N_{\text{bound}}} q_{b(m)} \delta(\mathbf{r} - \mathbf{r}_m - \mathbf{r}_{b(m)}) + \sum_{f=1}^{N_{\text{free}}} q_f \delta(\mathbf{r} - \mathbf{r}_f). \tag{2.22}$$

Bound carriers can be considered in terms of charges of atoms, molecules or valence electrons, respectively. For the case of metamolecules bound carriers are associated with ensembles of free electrons which are bound by the geometry of the metamolecule and that can be driven into resonance upon external illumination. Therefore, noble metals are typically used as building blocks, because of their high density of conduction band carriers. Averaging of Eq.(2.22) then reads as

$$\langle \mathfrak{r}(\mathbf{r}, t) \rangle = \sum_{m=1}^{N_{\text{molecules}}} \sum_{b(m)=1}^{N_{\text{bound}}} q_{b(m)} G(\mathbf{r} - \mathbf{r}_m - \mathbf{r}_{b(m)}) + \sum_{f=1}^{N_{\text{free}}} q_f G(\mathbf{r} - \mathbf{r}_f). \tag{2.23}$$

In a final step, it is assumed that the typical dimensions over which the averaging is performed are much larger than the molecular dimensions. If this applies, a Taylor expansion of the bound

contribution of Eq.(2.23) up to the second order in the vicinity of $|\mathbf{r} - \mathbf{r}_m|$ yields for the $m-$th molecule

$$\langle \mathfrak{r}_{\text{bound}}(\mathbf{r}, t)\rangle_m = \sum_{b(m)=1}^{N_{\text{bound}}} q_{b(m)} G(\mathbf{r} - \mathbf{r}_m - \mathbf{r}_{b(m)}) \tag{2.24}$$

$$\approx \sum_{b(m)=1}^{N_{\text{bound}}} q_{b(m)} \left\{ G(\mathbf{r} - \mathbf{r}_m) - \mathbf{r}_{b(m)} \cdot \nabla G(\mathbf{r} - \mathbf{r}_m) \right.$$

$$\left. + \frac{1}{2} \sum_{\alpha,\beta} [\mathbf{r}_{b(m)}]_\alpha [\mathbf{r}_{b(m)}]_\beta \frac{\partial^2}{\partial r_\alpha \partial r_\beta} G(\mathbf{r} - \mathbf{r}_m) \right\}. \tag{2.25}$$

Regarding the series expansion Eq.(2.25) one can define the electric multipole moments [section 2.1.2] yielding an averaged carrier density that can be expressed as

$$\langle \mathfrak{r}_{\text{bound}}(\mathbf{r}, t)\rangle_m \approx \tilde{q}_m G(\mathbf{r} - \mathbf{r}_m) - \mathbf{p}_m \cdot \nabla G(\mathbf{r} - \mathbf{r}_m)$$

$$+ \frac{1}{6} \sum_{\alpha,\beta} (Q_m)_{\alpha\beta} \frac{\partial^2}{\partial r_\alpha \partial r_\beta} G(\mathbf{r} - \mathbf{r}_m). \tag{2.26}$$

In Eq.(2.26) $\tilde{q}_m$, $\mathbf{p}_m$, and $\hat{\mathbf{Q}}_m$ represent the *bound* or *molecular* quantities: charge, electric dipole, and electric quadrupole moment, associated with the $m-$th molecule, respectively

$$\tilde{q}_m = \sum_{b(m)=1}^{N_{\text{bound}}} q_{b(m)}, \tag{2.27}$$

$$\mathbf{p}_m = \sum_{b(m)=1}^{N_{\text{bound}}} q_{b(m)} \mathbf{r}_{b(m)}, \tag{2.28}$$

$$(Q_m)_{\alpha\beta} = 3 \sum_{b(m)=1}^{N_{\text{bound}}} q_{b(m)} (r_{b(m)})_\alpha (r_{b(m)})_\beta. \tag{2.29}$$

In passing it is mentioned that a primitive quadrupole tensor has been applied in order to obtain Maxwell's equations which are origin-independent [GPR92, dLR05]. Considering Eq.(2.26) one would end up at exactly the same expression, if the charge distribution would have been

$$\mathfrak{r}_{\text{bound}}(\mathbf{r}, t) = \sum_{m=1}^{N_{\text{molecules}}} \left[ \tilde{q}_m \delta(\mathbf{r} - \mathbf{r}_m) - \nabla \cdot \mathbf{p}_m \delta(\mathbf{r} - \mathbf{r}_m) \right.$$

$$\left. + \frac{1}{6} \sum_{\alpha,\beta} \frac{\partial^2}{\partial r_\alpha \partial r_\beta} (Q_m)_{\alpha\beta} \delta(\mathbf{r} - \mathbf{r}_m) \right]. \tag{2.30}$$

With the averaging procedure according to Eq.(2.20) and Eqs.(2.12,2.13) one obtains

$$\langle \mathfrak{r}_{\text{bound}}(\mathbf{r}, t) \rangle = \sum_{m=1}^{N_{\text{molecules}}} \left\langle \tilde{q}_m \delta(\mathbf{r} - \mathbf{r}_m) \right\rangle - \nabla \cdot \left\langle \mathbf{p}_m \delta(\mathbf{r} - \mathbf{r}_m) \right\rangle$$
$$+ \frac{1}{6} \sum_{\alpha, \beta} \frac{\partial^2}{\partial r_\alpha \partial r_\beta} \left\langle (Q_m)_{\alpha\beta} \delta(\mathbf{r} - \mathbf{r}_m) \right\rangle \Big]. \tag{2.31}$$

The explicit application of the convolution [Eq.(2.20)] reflects Eq.(2.26), but solely by considering Eq.(2.31) one has an intuitive physical interpretation of the averaging procedure at hand. Any microscopic molecular or atomic carrier ensemble will result in a collection of electric point multipoles in the averaged macroscopic domain. For the first inhomogeneous equation (2.19) the averaged charge density (2.31) gives

$$\epsilon_0 \nabla \cdot \langle \mathfrak{E}(\mathbf{r}, t) \rangle = \langle \mathfrak{r}(\mathbf{r}, t) \rangle,$$
$$\sum_\alpha \frac{\partial}{\partial r_\alpha} \left[ \epsilon_0 \langle \mathfrak{E}_\alpha(\mathbf{r}, t) \rangle + P_\alpha(\mathbf{r}, t) - \frac{\partial}{\partial r_\beta} Q_{\alpha\beta}(\mathbf{r}, t) \right] = \rho(\mathbf{r}, t). \tag{2.32}$$

Whereby in Eq.(2.32) the *macroscopic charge density*

$$\rho(\mathbf{r}, t) = \sum_{m=1}^{N_{\text{molecules}}} \left\langle \tilde{q}_m \delta(\mathbf{r} - \mathbf{r}_m) \right\rangle + \sum_{f=1}^{N_{\text{free}}} \left\langle \tilde{q}_f \delta(\mathbf{r} - \mathbf{r}_f) \right\rangle, \tag{2.33}$$

the *macroscopic polarization*

$$\mathbf{P}(\mathbf{r}, t) = \sum_{m=1}^{N_{\text{molecules}}} \left\langle \mathbf{p}_m \delta(\mathbf{r} - \mathbf{r}_m) \right\rangle, \tag{2.34}$$

and the *macroscopic quadrupole density*

$$Q_{\alpha\beta}(\mathbf{r}, t) = \frac{1}{6} \sum_{m=1}^{N_{\text{molecules}}} \left\langle (Q_m)_{\alpha\beta} \delta(\mathbf{r} - \mathbf{r}_m) \right\rangle, \tag{2.35}$$

have been introduced. Hence, the electric displacement $\mathbf{D}(\mathbf{r}, t)$ can be introduced formally on the basis of Eq.(2.23) as

$$\mathbf{D}(\mathbf{r}, t) = \epsilon_0 \mathbf{E}(\mathbf{r}, t) + \mathbf{P}(\mathbf{r}, t) - \nabla \cdot \hat{\mathbf{Q}}(\mathbf{r}, t), \text{ with } [\nabla \cdot \hat{\mathbf{Q}}]_\alpha \equiv \sum_\beta \frac{\partial}{\partial r_\beta} Q_{\alpha\beta}. \tag{2.36}$$

To finalize the transition from microscopic to macroscopic Maxwell's equations, the microscopic current density needs to be averaged. Averaging microscopic free and molecular currents

in the form of

$$\mathbf{j}(\mathbf{r}, t) \quad = \quad \langle \mathbf{j}_{\text{bound}}(\mathbf{r}, t) \rangle + \langle \mathbf{j}_{\text{free}}(\mathbf{r}, t) \rangle \qquad (2.37)$$

$$= \quad \sum_{m=1}^{N_{\text{molecules}}} \sum_{b(m)=1}^{N_{\text{bound}}} q_{b(m)} [\mathbf{v}_m + \mathbf{v}_{b(m)}] \delta(\mathbf{r} - \mathbf{r}_m - \mathbf{r}_{b(m)}) + \sum_{f=1}^{N_{\text{free}}} q_f \mathbf{v}_f \delta(\mathbf{r} - \mathbf{r}_f), \quad (2.38)$$

will lead, similar to the charge density Eq.(2.23), to

$$\langle \mathbf{j}(\mathbf{r}, t) \rangle \quad = \quad \sum_{m=1}^{N_{\text{molecules}}} \sum_{b(m)=1}^{N_{\text{bound}}} q_{b(m)} [\mathbf{v}_m + \mathbf{v}_{b(m)}] G(\mathbf{r} - \mathbf{r}_m - \mathbf{r}_{b(m)}) + \sum_{f=1}^{N_{\text{free}}} q_f \mathbf{v}_f G(\mathbf{r} - \mathbf{r}_f) \quad (2.39)$$

Now, the bound carrier contribution of Eq.(2.39) consists of two parts, the velocity of the $m$-th molecule $\mathbf{v}_m$ together with the relative velocity of the bound charges $\mathbf{v}_{b(m)}$ and the free carrier motion $\mathbf{v}_f$ which are simply added in the non-relativistic regime. Again the expression can be analyzed in terms of a Taylor expansion up to second order

$$\langle \mathbf{j}_{\text{bound}}(\mathbf{r}, t) \rangle_m \quad = \quad \sum_{b(m)=1}^{N_{\text{bound}}} q_{b(m)} [\mathbf{v}_m + \mathbf{v}_{b(m)}] G(\mathbf{r} - \mathbf{r}_m - \mathbf{r}_{b(m)}) \qquad (2.40)$$

$$\approx \quad \sum_{b(m)=1}^{N_{\text{bound}}} q_{b(m)} [\mathbf{v}_m + \mathbf{v}_{b(m)}] \Big[ G(\mathbf{r} - \mathbf{r}_m) - \mathbf{r}_{b(m)} \cdot \nabla G(\mathbf{r} - \mathbf{r}_m) $$

$$+ \sum_{\alpha\beta} [r_{b(m)}]_\alpha [r_{b(m)}]_\beta \frac{\partial^2}{\partial r_\alpha \partial r_\beta} G(\mathbf{r} - \mathbf{r}_m) \Big]. \qquad (2.41)$$

Similarly to the procedure applied for the charge density the molecular current density (2.41) can be transformed into [Rus70]

$$\langle j_\alpha(\mathbf{r}, t) \rangle \quad = \quad j_\alpha(\mathbf{r}, t) + \frac{\partial}{\partial t} \Big[ P_\alpha(\mathbf{r}, t) - \frac{\partial}{\partial r_\beta} Q_{\alpha\beta}(\mathbf{r}, t) \Big] + [\nabla \times \mathbf{M}(\mathbf{r}, t]_\alpha$$

$$+ \sum_\beta \frac{\partial}{\partial r_\beta} \sum_{m=1}^{N_{\text{molecules}}} \Big\langle \Big[ (p_m)_\beta (v_m)_\alpha - (p_m)_\alpha (v_m)_\beta \Big] \delta(\mathbf{r} - \mathbf{r}_m) \Big\rangle$$

$$+ \frac{1}{6} \sum_{\beta\gamma} \frac{\partial^2}{\partial r_\beta \partial r_\gamma} \sum_{m=1}^{N_{\text{molecules}}} \Big\langle \Big[ (Q_m)_{\alpha\beta} (v_m)_\gamma - (Q_m)_{\gamma\beta} (v_m)_\alpha \Big] \delta(\mathbf{r} - \mathbf{r}_m) \Big\rangle,$$

$$(2.42)$$

where the *macroscopic current density*

$$\mathbf{j}(\mathbf{r}, t) = \sum_{f=1}^{N_{\text{free}}} \Big\langle q_f \mathbf{v}_f \delta(\mathbf{r} - \mathbf{r}') \Big\rangle + \sum_{m=1}^{N_{\text{molecules}}} \Big\langle q_m \mathbf{v}_m \delta(\mathbf{r} - \mathbf{r}') \Big\rangle, \qquad (2.43)$$

the *macroscopic magnetization*

$$\mathbf{M}(\mathbf{r}, t) = \sum_{m=1}^{N_{\text{molecules}}} \left\langle \mathbf{m}_m \delta(\mathbf{r} - \mathbf{r}') \right\rangle, \tag{2.44}$$

as well as the *molecular magnetic dipole moment*

$$\mathbf{m}_m = \frac{1}{2} \sum_{b(m)=1}^{N_{\text{bound}}} q_{b(m)} [\mathbf{r}_{b(m)} \times \mathbf{v}_{b(m)}], \tag{2.45}$$

have been introduced. The last two terms of Eq.(2.42) are usually negligible since for many optical systems the molecular velocity is assumed to be zero or at least much smaller than the localized velocities of the bound carriers [Jac75]. These contributions have been taken into account just for being consistent, but are formally dropped in the following by setting $\mathbf{v}_m = 0$. It is convenient to write the current density in this form, because it is then easily possible to evaluate the remaining inhomogeneous Maxwell's equation (2.18)

$$
\begin{aligned}
\frac{1}{\mu_0} \nabla \times \langle \mathfrak{B}(\mathbf{r}, t) \rangle - \epsilon_0 \frac{\partial}{\partial t} \langle \mathfrak{E}(\mathbf{r}, t) \rangle &= \langle \mathbf{j}(\mathbf{r}, t) \rangle, \\
\frac{1}{\mu_0} \nabla \times \mathbf{B}(\mathbf{r}, t) - \frac{\partial}{\partial t} \left[ \epsilon_0 \mathbf{E} + \mathbf{P}(\mathbf{r}, t) - \nabla \times \hat{\mathbf{Q}}(\mathbf{r}, t) \right] &= \mathbf{j}(\mathbf{r}, t) + \nabla \times \mathbf{M}(\mathbf{r}, t), \\
\nabla \times \left[ \frac{1}{\mu_0} \mathbf{B}(\mathbf{r}, t) - \mathbf{M}(\mathbf{r}, t) \right] - \frac{\partial}{\partial t} \mathbf{D}(\mathbf{r}, t) &= \mathbf{j}(\mathbf{r}, t),
\end{aligned} \tag{2.46}
$$

which is equal to Eq.(2.7) if the macroscopic magnetic field is defined by

$$\mathbf{H}(\mathbf{r}, t) = \frac{1}{\mu_0} \mathbf{B}(\mathbf{r}, t) - \mathbf{M}(\mathbf{r}, t). \tag{2.47}$$

This concise discussion of the averaging procedure provides an easy understanding of the macroscopic Maxwell's equations for natural media. Moreover the multipole moments up to second order are defined and their contribution to the macroscopic *constitutive relations*, i.e., Eqs.(2.36,2.47) has been retraced.

Performing the averaging procedure and determining the constitutive relations in the above manner is the method of choice in various textbooks but not the only possibility. For several reasons the magnetic dipole response can be included within the macroscopic current density. Using another definition of the macroscopic current density that is based on Eq.(2.42) one obtains

$$\mathbf{j}(\mathbf{r}, t) = \left\langle \sum_{f=1}^{N_{\text{free}}} q_f \mathbf{v} \delta(\mathbf{r} - \mathbf{r}_f) \right\rangle + \nabla \times \mathbf{M}(\mathbf{r}, t). \tag{2.48}$$

The current density (2.48) with the related macroscopic charge density $\rho$ must satisfy the

equation of continuity

$$\frac{\partial}{\partial t}\rho(\mathbf{r}, t) + \nabla \cdot \mathbf{j}(\mathbf{r}, t) = 0. \tag{2.49}$$

With the current density (2.48) the charge density remains equal to that in Eq.(2.33), because $\nabla \cdot [\nabla \times \mathbf{M}] = 0$. The main difference caused by the above definition of the current is the constitutive relation for the magnetic field when compared with Eq.(2.47)

$$\mathbf{H}(\mathbf{r}, t) = \frac{1}{\mu_0}\mathbf{B}(\mathbf{r}, t). \tag{2.50}$$

Hence, there is a certain degree of freedom in defining the macroscopic current density. The influence of such modifications will result in different constitutive relations, e.g., Eq.(2.50) and thus in differing boundary conditions at the interface of the averaged media compared with the standard boundary conditions [Jac75]. In the same manner as the magnetic dipole moment has been included in $\mathbf{j}$ also the electric multipole contributions could be included yielding another constitutive relation for the electric field [Per63], when compared with Eq.(2.36). So it is important to keep this ambiguity in mind when reading articles or books where differing constitutive relations or averaging procedures have been used.

In order to conveniently describe a macroscopic medium, for which the averaging is performed, material parameters can be introduced. This is typically done in the Fourier domain to which the transformations may be defined as

$$\mathbf{X}(t) = \frac{1}{2}\left[\int_{\omega \in \mathbb{R}} d\omega \mathbf{X}(\omega)e^{-i\omega t} + \text{c.c.}\right], \tag{2.51}$$

$$\mathbf{X}(\mathbf{r}, t) = \frac{1}{2}\left[\int_{\omega \in \mathbb{R}} d\omega \int_{\mathbf{k} \in \mathbb{R}^3} d\mathbf{k} \mathbf{X}(\mathbf{k}, \omega)e^{i\mathbf{k}\mathbf{r} - i\omega t} + \text{c.c.}\right]. \tag{2.52}$$

Applying the temporal Fourier transformation (2.51) to Eq.(2.36) and Eq.(2.47) the constitutive relations become

$$\mathbf{D}(\mathbf{r}, \omega) = \epsilon_0 \mathbf{E}(\mathbf{r}, \omega) + \mathbf{P}(\mathbf{r}, \omega) - \nabla \cdot \hat{\mathbf{Q}}(\mathbf{r}, \omega), \tag{2.53}$$

$$\mathbf{H}(\mathbf{r}, \omega) = \frac{1}{\mu_0}\mathbf{B}(\mathbf{r}, \omega) - \mathbf{M}(\mathbf{r}, \omega). \tag{2.54}$$

Now that all multipole moments are related to carrier dynamics induced by the impinging fields, a linear dependence of all moments on the electric field can be assumed[2]. Due to the presence of spatial derivatives in the dielectric displacement, e.g., in front of the electric quadrupole tensor in Eq.(2.53), the general response will show *non-local effects*. Hence, for a linear relation between the field and the moments, the application of the Fourier transform (2.52) will immediately result in a $k$-dependence in the constitutive relations[3]. Thus, in general

---

[2]This assumption of course only holds in the linear optical regime. For the considerations of multipole induced nonlinearities the dependence is different [PCT⁺09].

[3]The same holds for the magnetic constitutive relation, if the magnetization, i.e., the magnetic dipole moment, is induced by the electric field as well.
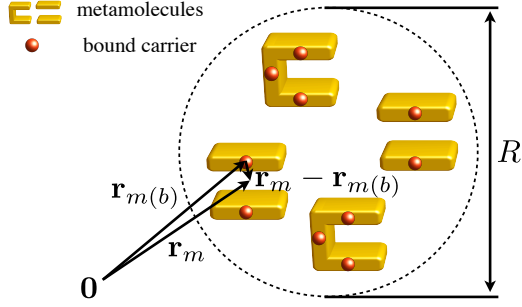
**Figure 2.2:** Illustration of the averaging volume including nanoparticles that represent artificial molecules.

second order moments will induce *spatial dispersion* and for Eqs.(2.53, 2.54) the following expressions can be introduced

$$\mathbf{D}(\mathbf{k},\omega) = \epsilon_0 \hat{\epsilon}(\mathbf{k},\omega)\mathbf{E}(\mathbf{k},\omega), \qquad (2.55)$$

$$\mathbf{B}(\mathbf{k},\omega) = \mu_0 \hat{\mu}(\mathbf{k},\omega)\mathbf{H}(\mathbf{k},\omega). \qquad (2.56)$$

Here $\hat{\epsilon}(\mathbf{k},\omega)$ corresponds to the *electric permittivity* while $\hat{\mu}(\mathbf{k},\omega)$ represents the *magnetic permeability* for the averaged medium. These equations complete the averaging process since they allow to treat any macroscopic, i.e., averaged medium, by the knowledge of its microscopic constituents. Such constituents are averaged multipole moments that account for light-matter interactions with bound and free molecular carriers. Having arrived at the macroscopic level, e.g., Eqs.(2.55, 2.56), the basics of the averaging procedure are no longer of interest for many applications, since for various macroscopic media these values are obtained experimentally [JC72].

The purpose of the detailed recapitulation in this section was to repeat the fundamental principles which in the following will facilitate the understanding of ensembles of nanostructures. These are acting as artificial atoms or molecules, termed *metamolecules*, forming a new material class that will be considered in complete analogy throughout this work (Fig.2.2).

The most appealing difference in the averaging of nanoparticles representing artificial metamolecules in comparison to ordinary molecules is that all multipole moments in nanoparticles are induced by an electromagnetic field. Hence, all moments in metamolecules vanish without an external field. In contrast, real molecules can possess permanent multipole contributions even in the absence of any external fields. A prominent example for a material with a permanent molecular quadrupole moment is carbon dioxide being the first experimentally measured molecular quadrupole [BD63]. This example shows that higher-order multipolar response has been observed and investigated before. But in order to realize this higher-order response at arbitrary frequencies, e.g., in the range of optical frequencies, induced multipoles are required. In metamolecules induced higher-order multipoles can be achieved at will. To obtain second-order effects in metamolecules it has been shown above that effects such as *non-locality*, i.e., *spatial dispersion* in the Fourier domain, must exist. For this purpose, each metamolecule must comprise a certain dimension in propagation direction. On the other side, metamolecules are

supposed to be as small as possible to make the averaging and the multipole expansion meaningful. Thus, metamolecules should possess sub-wavelength dimensions [ZDU+08]. These two competing issues led to the concept of *mesoscopic structures* [PHSY96, MPR+10], which applies to metamolecules exhibiting particularly prepared optical effects, e.g., artificial magnetism occurring at optical wavelengths [PHRS99, BOK+09, GV09].

### 2.1.2 Multipole radiation

In order to classify and identify individual multipolar material interactions beyond effective material responses, i.e., a non-vanishing magnetic permeability of an ensemble, etc. the characteristic near-field distributions for molecular multipole moments are considered in this section as an adequate tool. Multipolar near-field contributions up to the second order of an arbitrary molecular carrier and current distribution are considered in this section. The motivation for the detailed analysis is to determine multipolar excitations from an individual metamolecule's near-field pattern. Such field distributions represent an important subject of this work in the following chapters. The derivation starts with the vector potential $\mathbf{A}$ and the scalar potential $\phi$, which are related to the fields [Jac75] as

$$\mathfrak{E}(\mathbf{r},t) \equiv -\nabla\phi(\mathbf{r},t) - \frac{\partial}{\partial t}\mathbf{A}(\mathbf{r},t), \tag{2.57}$$

$$\mathfrak{B}(\mathbf{r},t) \equiv \nabla \times \mathbf{A}(\mathbf{r},t). \tag{2.58}$$

Together with the microscopic Maxwell's equations (2.1-2.4) and assuming Lorenz gauging $(\nabla \cdot \mathbf{A} + c^{-2}\frac{\partial}{\partial t}\phi = 0)$ the defining wave equations for both potentials become

$$\Delta\mathbf{A}(\mathbf{r},t) - \frac{1}{c^2}\frac{\partial^2}{\partial t^2}\mathbf{A}(\mathbf{r},t) = -\mu_0\mathbf{j}(\mathbf{r},t), \tag{2.59}$$

$$\Delta\phi(\mathbf{r},t) - \frac{1}{c^2}\frac{\partial^2}{\partial t^2}\phi(\mathbf{r},t) = -\frac{1}{\epsilon_0}\mathfrak{r}(\mathbf{r},t), \tag{2.60}$$

which can be solved in general by the retarded potential

$$\mathbf{A}(\mathbf{r},t) = \frac{\mu_0}{4\pi}\int_{V_0} d\mathbf{r}'^3 \frac{\mathbf{j}(\mathbf{r}-\mathbf{r}',t-\frac{|\mathbf{r}-\mathbf{r}'|}{c})}{|\mathbf{r}-\mathbf{r}'|}. \tag{2.61}$$

The vector potential (2.61) together with Eqs.(2.57,2.58) describes the creation of radiation due to temporal current dynamics in a localized volume $V_0$. In order to evaluate this expression the current density is Fourier transformed via Eq.(2.51)

$$\mathbf{j}\left(\mathbf{r}',t-\frac{|\mathbf{r}-\mathbf{r}'|}{c}\right) = \mathbf{j}(\mathbf{r}')e^{-i\omega(t-\frac{|\mathbf{r}-\mathbf{r}'|}{c})}, \tag{2.62}$$

and is translated to the vector potential [Nol02]

$$\mathbf{A}(\mathbf{r},t) = \mathbf{A}(\mathbf{r},\omega)e^{-i\omega t} = \frac{\mu_0}{4\pi}\int_{V_0} d\mathbf{r}'^3 \frac{\mathbf{j}(\mathbf{r}')}{|\mathbf{r}-\mathbf{r}'|}e^{ik|\mathbf{r}-\mathbf{r}'|}e^{-i\omega t}, \qquad \text{with } k \equiv \frac{\omega}{c}. \tag{2.63}$$

The magnetic field (2.58) can be regarded as the source inducing electric fields radiated by the carrier and current distribution ($\mathfrak{r} = 0, \mathfrak{j} = 0$) according to Eq.(2.2)

$$\mathfrak{E}(\mathbf{r}, \omega) = i\frac{c^2}{\omega}\nabla \times \nabla \times \mathbf{A}(\mathbf{r}, \omega). \tag{2.64}$$

Hence, it is sufficient to consider the vector potential $\mathbf{A}(\mathbf{r}, \omega)$ to determine the radiated fields. Now the integral kernel of Eq.(2.63) can be expanded near the origin of the current density by a Tailor series

$$\frac{e^{ik|\mathbf{r}-\mathbf{r}'|}}{|\mathbf{r} - \mathbf{r}'|} \approx \frac{e^{ikr}}{r}\left[1 + \mathbf{n} \cdot \mathbf{r}'\left(\frac{1}{r} - ik\right)\right], \qquad \text{with } \mathbf{n} \equiv \frac{\mathbf{r}}{r}. \tag{2.65}$$

And the vector potential can be obtained as

$$\begin{aligned} \mathbf{A}(\mathbf{r}, \omega) &\approx \frac{\mu_0}{4\pi}\frac{e^{ikr}}{r}\int_{V_0} d^3r'\mathbf{j}(\mathbf{r}') + \frac{\mu_0}{4\pi}\left(\frac{1}{r} - ik\right)\frac{e^{ikr}}{r}\int_{V_0} d^3r'\mathbf{j}(\mathbf{r}')(\mathbf{n} \cdot \mathbf{r}') \\ &\equiv \mathbf{A}^{(1)}(\mathbf{r}', \omega) + \mathbf{A}^{(2)}(\mathbf{r}', \omega). \end{aligned} \tag{2.66}$$

The *first-order* term $\mathbf{A}^{(1)}$ in Eq.(2.66) corresponds to the electric dipole moment, while the *second-order* expansion term $\mathbf{A}^{(2)}$ accounts for both the magnetic dipole and the electric quadrupole contribution. It is important to keep in mind that both, the electric quadrupole as well as the magnetic dipole moment, represent second-order multipole contributions. To show the relationship of $\mathbf{A}^{(1)}$ with the electric dipole moment, the first term on the right hand side of Eq.(2.66) can be transformed with the continuity relation (2.49) and Gauss's law to

$$\mathbf{A}^{(1)}(\mathbf{r}, \omega) = \mathbf{A}_{\text{ED}}(\mathbf{r}, \omega) = -i\omega\frac{\mu_0}{4\pi}\frac{e^{ikr}}{r}\mathbf{p}. \tag{2.67}$$

The electric dipole moment $\mathbf{p}$ in Eq.(2.67) represents the *molecular dipole* moment Eq.(2.28)

$$\mathbf{p} = \int_{V_0} d^3r'\mathbf{r}'\rho(\mathbf{r}') = \sum_{b(m)=1}^{N_{\text{bound}}}\int_{V_0} d^3r'\mathbf{r}'q_{b(m)}\delta(\mathbf{r}' - \mathbf{r}_{b(m)}) = \mathbf{p}_m. \tag{2.68}$$

The second term in Eq.(2.66) splits into two contributions using the identity

$$\mathbf{j}(\mathbf{r}')(\mathbf{n} \cdot \mathbf{r}') = \frac{1}{2}[\mathbf{r}' \times \mathbf{j}(\mathbf{r}')] \times \mathbf{n} + \frac{1}{2}\left\{[\mathbf{r}' \times \mathbf{j}(\mathbf{r}')]\mathbf{j}(\mathbf{r}') + [\mathbf{n} \cdot \mathbf{j}(\mathbf{r}')]\mathbf{r}'\right\}, \tag{2.69}$$

for which the vector potential for the second order can be separated into the magnetic dipole and the electric quadrupole parts

$$\mathbf{A}^{(2)}(\mathbf{r}, \omega) = \mathbf{A}_{\text{MD}}(\mathbf{r}, \omega) + \mathbf{A}_{\text{EQ}}(\mathbf{r}, \omega), \tag{2.70}$$

$$\mathbf{A}_{\text{MD}}(\mathbf{r}, \omega) = \frac{\mu_0}{4\pi}\frac{e^{ikr}}{r}\left(\frac{1}{r} - ik\right)\left[\frac{1}{2}\int_{-\infty}^{\infty} d^3r'\mathbf{r}' \times \mathbf{j}(\mathbf{r}')\right] \times \mathbf{n}, \tag{2.71}$$

$$\mathbf{A}_{\text{EQ}}(\mathbf{r}, \omega) = \frac{\mu_0}{4\pi}\frac{e^{ikr}}{r}\left(\frac{1}{r} - ik\right)\int_{-\infty}^{\infty} d^3r'\frac{1}{2}\left\{[\mathbf{n} \cdot \mathbf{r}']\mathbf{j}(\mathbf{r}') + [\mathbf{n} \cdot \mathbf{j}(\mathbf{r}')]\mathbf{r}'\right\}. \tag{2.72}$$
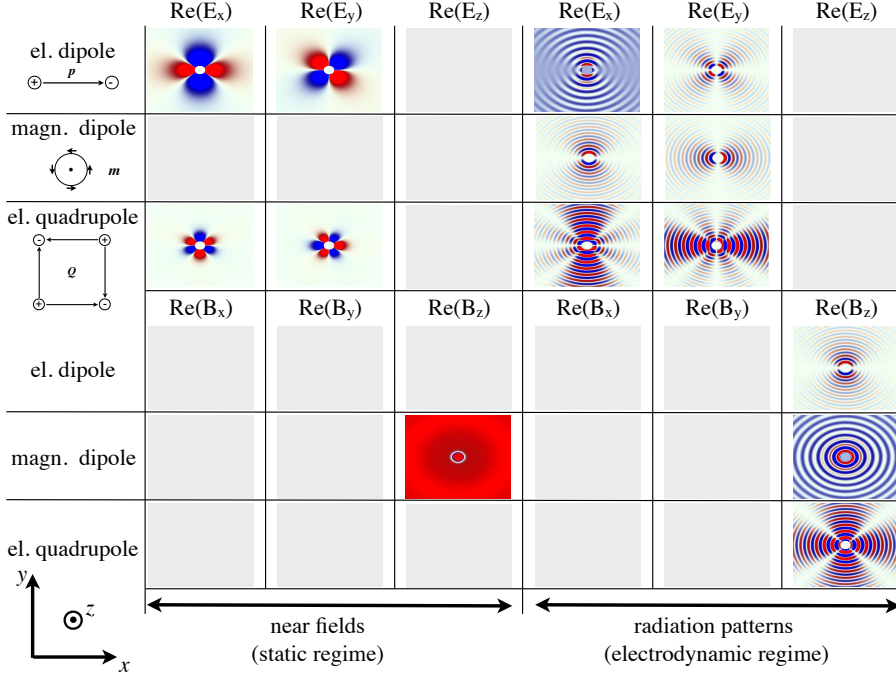
19

**Figure 2.3:** Illustration of the electric (upper 3 rows) and the magnetic (lower 3 rows) near-fields (left 3 columns) and their radiated fields (right 3 columns).

Considering bound carrier dynamics in terms of currents written by

$$\mathbf{j}(\mathbf{r}') = \sum_{b(m)=1}^{N_{\text{bound}}} q_{b(m)} \mathbf{v}_{b(m)} \delta(\mathbf{r}' - \mathbf{r}_{b(m)}), \tag{2.73}$$

together with the expression (2.45) the vector potential for the molecular magnetic dipole moments reads

$$\mathbf{A}_{\text{MD}}(\mathbf{r}) = \frac{\mu_0}{4\pi} \frac{e^{ikr}}{r} \left( \frac{1}{r} - ik \right) \mathbf{m}_m \times \mathbf{n}. \tag{2.74}$$

The remaining electric quadrupole vector potential (2.72) can be transformed with the identity

$$\int_{V_0} d^3r' \left\{ (\mathbf{n} \cdot \mathbf{r}') \mathbf{j}(\mathbf{r}') + [\mathbf{j}(\mathbf{r}') \cdot \mathbf{n}] \mathbf{r}' \right\} = -\int_{V_0} d^3r' \mathbf{r}'(\mathbf{n} \cdot \mathbf{r}')[\nabla' \cdot \mathbf{j}(\mathbf{r}')], \tag{2.75}$$

and the continuity equation (2.49) to

$$\mathbf{A}_{\text{EQ}}(\mathbf{r}, \omega) = i\omega \frac{\mu_0}{8\pi} \frac{e^{ikr}}{r} \left( \frac{1}{r} - ik \right) \int_{V_0} d^3r' \mathbf{r}'(\mathbf{n} \cdot \mathbf{r}') \rho(\mathbf{r}') \tag{2.76}$$

$$= i\omega \frac{\mu_0}{8\pi} \frac{e^{ikr}}{r} \left( \frac{1}{r} - ik \right) \sum_{\alpha} \sum_{\beta} \mathbf{e}_{\alpha} (Q)_{\alpha\beta}(\mathbf{n}), \qquad \text{with } \mathbf{e}_{\alpha} \equiv \frac{\mathbf{r}_{\alpha}}{r}. \tag{2.77}$$

The modified molecular quadrupole tensor $\hat{\mathbf{Q}}(\mathbf{n})$ of a carrier density according to Eq.(2.68) is

$$\hat{\mathbf{Q}}(\mathbf{n}) = \begin{pmatrix} Q_{xx}n_x & Q_{xy}n_x & Q_{xz}n_x \\ Q_{yx}n_y & Q_{yy}n_y & Q_{yz}n_y \\ Q_{zx}n_z & Q_{zy}n_z & Q_{zz}n_z \end{pmatrix}, \tag{2.78}$$

where $Q_{\alpha\beta}$ are the molecular quadrupole entries according to Eq.(2.29). After arriving at the vector potentials Eqs.(2.67,2.74,2.77) the near- and far-field distributions for first- and second-order multipoles can be determined by the relations Eqs.(2.57,2.58). It is mentioned that the electrodynamical derivation easily allows for the determination of the static fields with the transition $k \to 0$. For illustration the in-plane radiation patterns for primitive carrier and current configurations have been computed for the static as well as the time harmonic radiation in Fig.2.3.

## 2.1.3 Localized plasmon polaritons

In this section the electrostatic approximation, a particular and frequently applied simplification for the electrodynamical treatment, will be applied to calculate the effective parameters of an ensemble of particulary shaped nanoparticles. This approximation is limited to metamolecules with such small dimensions that the internal field of the metamolecule can be assumed to be constant. Strictly speaking, the wavelength, being a number for the length scale of the spatial variations of incident electromagnetic plane waves, has to be much larger than the metamolecule's dimensions. This limitation is termed the *sub-wavelength criterion.*

It will be seen that the natural electric permittivity of certain materials in ellipsoidal-shaped metamolecules will allow for a resonant phenomenon in the optical response, termed *localized plasmon-polariton* (LPP). The derivation starts with the scalar potential according to Eq.(2.60), but in the electrostatic regime making time derivations safely negligible

$$\Delta\phi(\mathbf{r}, t) = -\frac{1}{\epsilon_0}\mathfrak{r}(\mathbf{r}, t). \tag{2.79}$$

Averaging [Eq.(2.20)] yields for the corresponding macroscopic scalar potential

$$\Delta\Phi(\mathbf{r}, t) = 0. \tag{2.80}$$

Eq.(2.80) is now considered for the case of elliptical particles. It is mentioned that for other nanoparticle shapes, except spheres, cylinders and ellipsoids, analytical solutions of Eq.(2.80) are hardly amenable. Here the notation according to Ref. [BH83] is used. Transformation towards elliptical coordinates provides the scalar potential for an external $z$-polarized electric field

$$\Phi_0(\mathbf{r}, t) = -zE_0 = -E_0\sqrt{\frac{(a_z^2 + \xi)(a_z^2 + \eta)(a_z^2 + \zeta)}{(a_x^2 - a_z^2)(a_y^2 - a_z^2)}}. \tag{2.81}$$

Hereby $a_{x,y,z}$ represent the semi axes of the ellipsoid in the principle directions $x, y, z$, respectively, and $\xi, \eta, \zeta$ are the elliptical coordinates [BH83]. The potential outside the ellipsoid comprises beyond the external contribution $\Phi_0$ the influence of the ellipsoid $\Phi_p$, considered as a perturbation, while the potential inside the ellipsoid is $\Phi_i$. The potential at the interface of the ellipsoid has to be continuous, described in elliptical coordinates by $\xi = 0$ and expressed by the condition

$$\Phi_i(0, \eta, \zeta) = \Phi_p(0, \eta, \zeta) + \Phi_0(0, \eta, \zeta). \tag{2.82}$$

The transformation of Eq.(2.80) in elliptical coordinates yields

$$\begin{aligned} \Delta\Phi(\mathbf{r}, t) &= (\eta - \zeta)f(\xi)\frac{\partial}{\partial\xi}\left[f(\xi)\frac{\partial\Phi}{\partial\xi}\right] + (\zeta - \xi)f(\eta)\frac{\partial}{\partial\eta}\left[f(\eta)\frac{\partial\Phi}{\partial\eta}\right] \\ &\quad + (\xi - \eta)f(\zeta)\frac{\partial}{\partial\zeta}\left[f(\zeta)\frac{\partial\Phi}{\partial\zeta}\right], \end{aligned} \tag{2.83}$$

with $f(u) = \sqrt{(u + a_x^2)(u + a_y^2)(u + a_z^2)}$ and $u \in [\xi, \eta, \zeta]$. The solutions of Eq.(2.83) for the unknown $\Phi_{p,i}$ are considered in form of the ansatz

$$\Phi_{p,i}(\xi, \eta, \zeta) = F(\xi)\sqrt{(a_z^2 + \eta)(a_z^2 + \zeta)}, \tag{2.84}$$

which is substituted into Eq.(2.83) yielding two solutions

$$F_1(\xi) = \sqrt{a_z^2 + \xi}, \tag{2.85}$$

$$F_2(\xi) = F_1(\xi)\int_\xi^\infty \frac{du}{F_1^2(u)f(u)}. \tag{2.86}$$

The requirement for vanishing potential at infinite distance from the ellipsoid is expressed by $\xi \to \infty$ which is only satisfied by $F_2(\xi)$. Hence, the solutions for the ellipsoid's potential

$$\Phi_p(\xi, \eta, \zeta) = C_p F_2(\xi)\sqrt{(a_z^2 + \eta)(a_z^2 + \zeta)}, \tag{2.87}$$

and the internal potential which has to be finite at the origin, are found

$$\Phi_i(\xi, \eta, \zeta) = C_i F_1(\xi)\sqrt{(a_z^2 + \eta)(a_z^2 + \zeta)}. \tag{2.88}$$

In order to determine the two unknown constants $C_{p,i}$, the boundary conditions for the potential (2.82) as well as the requirement for a continuous normal component of the dielectric displacement $\mathbf{D}(\mathbf{r}, \omega)$

$$\begin{aligned} \epsilon_i(\omega)\frac{\partial}{\partial\xi}\Phi_i(\xi, \eta, \zeta, \omega)\bigg|_{\xi=0} &= \epsilon_a(\omega)\frac{\partial}{\partial\xi}\Phi_p(\xi, \eta, \zeta, \omega)\bigg|_{\xi=0} \\ &\quad + \epsilon_a(\omega)\frac{\partial}{\partial\xi}\Phi_0(\xi, \eta, \zeta, \omega)\bigg|_{\xi=0}, \end{aligned} \tag{2.89}$$

yield two equations for two unknown constants. The permittivity denoted as $\epsilon_a$ represents the embedding ambient material, whereas $\epsilon_i$ accounts for the the ellipsoid's permittivity. The final expressions for the potentials in the Fourier domain [transformation 2.51] can be obtained as

$$\Phi_i(\xi, \eta, \zeta, \omega) = \Phi_0(\xi, \eta, \zeta, \omega)\frac{1}{1 + \frac{L_z[\epsilon_i(\omega) - \epsilon_a(\omega)]}{\epsilon_a(\omega)}}, \tag{2.90}$$

$$\Phi_p(\xi, \eta, \zeta, \omega) = \Phi_0(\xi, \eta, \zeta, \omega)\frac{a_x a_y a_z}{2}\frac{[\epsilon_a(\omega) - \epsilon_i(\omega)]\int_\xi^\infty \frac{du}{(a_z^2+u)f(u)}}{\epsilon_a(\omega) + L_z[\epsilon_i(\omega) - \epsilon_a(\omega)]}. \tag{2.91}$$

In Eqs.(2.90,2.91) the geometrical factors $L_l$ have been introduced as

$$L_l = \frac{a_x a_y a_z}{2}\int_0^\infty \frac{du}{(a_l^2 + u)f(u)}, \qquad \text{with } l \in [x, y, z]. \tag{2.92}$$

The potential (2.91) is typically solved for distances far away from the ellipsoid $r \gg a_{x,y,z}$ which allows the expansion of the integral in the nominator of Eq.(2.91)

$$\int_\xi^\infty \frac{du}{(a_z^2 + u)f(u)} \approx \int_\xi^\infty u^{-5/2}du = \frac{2}{3}\xi^{-3/2}. \tag{2.93}$$

For $\xi^2 \approx r^2$ the *far-field* scattering potential[4] of the ellipsoid can be finally determined

$$\Phi_p(\xi, \eta, \zeta, \omega) \approx \frac{E_0 cos(\theta)}{r^2}\frac{a_x a_y a_z[\epsilon_i(\omega) - \epsilon_a(\omega)]}{3\epsilon_a(\omega) + 3L_z[\epsilon_i(\omega) - \epsilon_a(\omega)]}. \tag{2.94}$$

The introduced angle $\theta$ accounts for the polarization direction of the external electric field with respect to the axis $a_z$ according to Eq.(2.81). In order to relate the found potential (2.94) to the multipole moments, the fundamental electric dipole vector potential can be translated into the corresponding scalar potential applying the Lorenz gauging relation $[\nabla \cdot \mathbf{A} + -i\omega\epsilon_a(\omega)c^{-2}\Phi = 0]$. This yields for the vector potential (2.67) of the electric dipole

$$\Phi_{ED}(\mathbf{r}, \omega) = \nabla \cdot \mathbf{A}_{ED}\frac{c^2}{-i\omega\epsilon_a(\omega)} = \frac{1}{4\pi\epsilon_0\epsilon_a(\omega)}\frac{\mathbf{p} \cdot \mathbf{r}}{r^3}. \tag{2.95}$$

Comparing Eq.(2.94) with Eq.(2.95), the electric dipole moment associated with the ellipsoid in the principle directions $l \in [x, y, z]$ follows directly

$$p_l(\omega) = \frac{4\pi\epsilon_0\epsilon_a(\omega)a_x a_y a_z}{3}\frac{\epsilon_i(\omega) - \epsilon_a(\omega)}{\epsilon_a(\omega) + L_l[\epsilon_i(\omega) - \epsilon_a(\omega)]}E_{0l}(\omega). \tag{2.96}$$

Having arrived at this point some important conclusions can be drawn which are beneficial to understand the physics of localized plasmon polaritons in more complex geometries.

---

[4]Typically the series expansion of the integral [Eq.(2.93)] is only performed up to the first order, yielding solely the electric dipole potential. Now, one might erroneously anticipate that higher series expansion orders could help to include higher-order multipoles. To include higher multipole orders it is first of all essential to have more complicated ansatz for the scalar potentials (2.87,2.88), see Ref. [LL85].
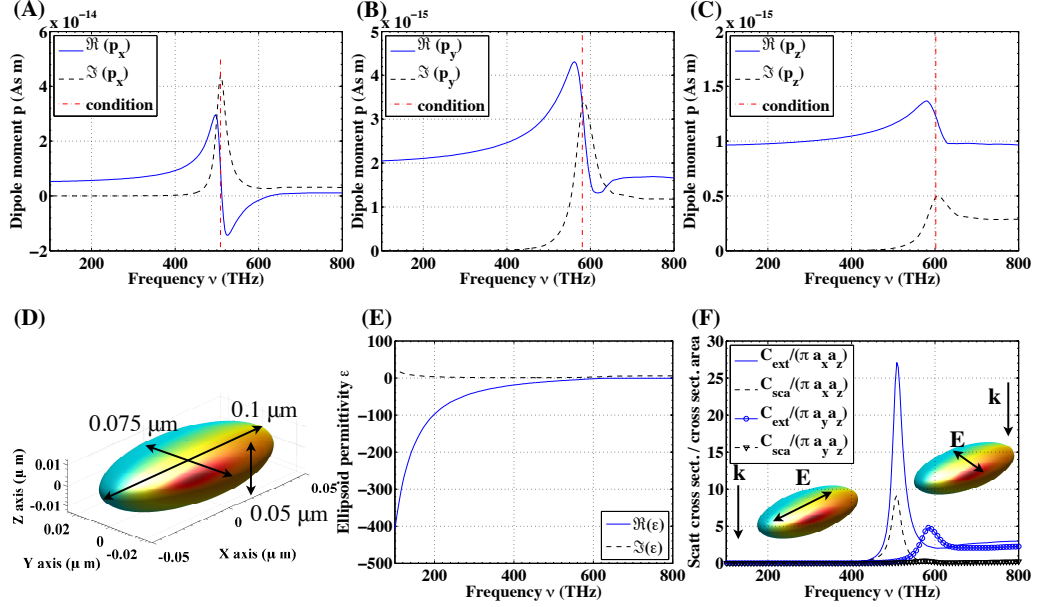
**Figure 2.4:** The dipole moment (2.96) for an electric field with the amplitude 1 for the three principle directions $x, y, z$ in (A,B,C), respectively. The red dotted line marks the frequency for which $[\epsilon_a(\omega)(1 - L_z) + L_z\epsilon_i(\omega) = 0]$ is fulfilled. (D) A sketch of an ellipsoid embedded in air together with the spatial dimensions. (E) The bulk permittivity of gold [JC72], used for all simulations. (F) The effective cross sections of the isolated ellipsoid for the two indicated polarization directions.

- The electric field induced by the ellipsoid $\mathbf{E}_p = -\nabla\Phi_p$

$$\mathbf{E}_p(\xi, \eta, \zeta, \omega) = -\frac{a_x a_y a_z}{2} \frac{[\epsilon_a(\omega) - \epsilon_i(\omega)]\nabla\left[\Phi_0 \int_\xi^\infty \frac{du}{(a_z^2 + u)f(u)}\right]}{\epsilon_a(\omega) + L_z[\epsilon_i(\omega) - \epsilon_a(\omega)]}, \qquad (2.97)$$

will be resonant, if the denominator becomes zero $[\epsilon_a(\omega)(1 - L_z) + L_z\epsilon_i(\omega) = 0]$. Since $L_l \leq 1$ for arbitrary ellipsoids, this condition can only be fulfilled if one of the two involved permittivities is negative. This property of having a negative permittivity can be naturally satisfied for metals at frequencies below the plasma frequency, see Fig.2.4(E). Hence, for metal ellipsoids, but also for their inverse geometry, i.e., elliptical dielectric voids in an ambient metallic material with negative permittivity, the local field can be enhanced at a certain resonance frequency[5]. This resonance corresponds to the *localized plasmon polariton mode.*

- Beyond having the ability of enhancing the local electric field one can also observe the LPP in the far-field. Averaging over an ensemble of identical ellipsoids (number density $\eta$) the macroscopic polarization via Eq.(2.35) and finally the corresponding effective permittivity (2.55) can be calculated

$$\epsilon_l(\omega) = 1 + \eta\epsilon_a(\omega)\frac{4\pi a_x a_y a_z}{3} \frac{\epsilon_i(\omega) - \epsilon_a(\omega)}{\epsilon_a(\omega) + L_l[\epsilon_i(\omega) - \epsilon_a(\omega)]}. \qquad (2.98)$$

It can be deduced that this effective permittivity represents a diagonal tensor, since a

---

[5]A detailed investigation of the local field enhancement of ellipsoids will be presented in section 3.1.1.
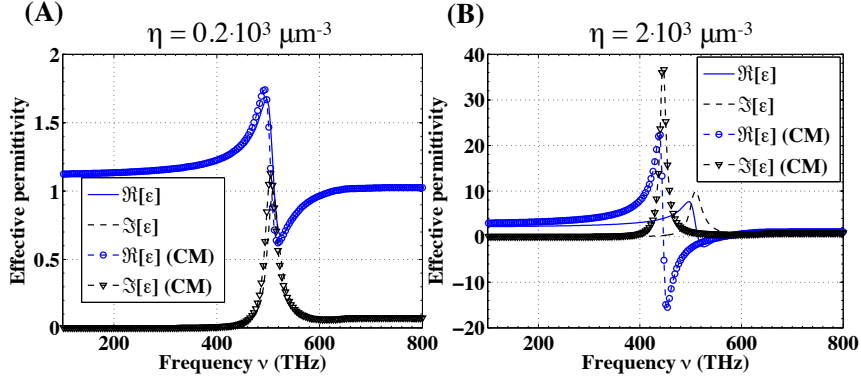
**Figure 2.5:** Comparison between effective permittivities predicted by Eq.(2.98) and the Clausius Mosotti (CM) formula [Eq.(2.99)] for two particle concentrations of ellipsoids according to Fig.2.4(D) for a polarization along the main axis: (A) 200 particles per $\mu m^3$ and (B) 2000 per $\mu m^3$.

polarized electric field induces a dipole moment only in the same direction. Since these entries are different for an ellipsoid with $a_x \neq a_y \neq a_z$ the general response has axial anisotropy in all three directions, see Fig.2.4(A-D). Hence, the general far-field response caused by a volume described by the effective permittivity (2.98) is expected to show a strong dispersion in the frequency domains where LPP resonances are excited.

- It is an important fact that the LPP resonance position is defined by both, the *material dispersion* $[\epsilon_i(\omega), \epsilon_a(\omega)]$, and the *geometrical dispersion*, induced solely by the geometry $(L_l)$ of the metamolecule, i.e., the ellipsoid.

- The influence of neighboring metamolecules is not considered by Eq.(2.98), since the averaged electric field of an ensemble of ellipsoids has been assumed to be the same as for the isolated ellipsoid. Hence, any electric field interaction of adjacent ellipsoids has been neglected. To consider this effect, which is important for large concentrations $\eta$, a local field correction can be done. Therefore the local field contributions of neighboring scatterers are considered by their polarization fields $\mathbf{E}_{\mathrm{pol}} = -\mathbf{P}/(3\epsilon_0)$ [Jac75]. This describes the electric field at the origin of a fictive sphere containing a volume of electric dipoles with the macroscopic polarization $\mathbf{P}$. In addition to the external field, the polarization field interacts with each dipole which yields an approximation for the averaged electric field. With this assumption the effective permittivity takes the following form

$$\epsilon_{\mathrm{eff},l}(\omega) = 1 + \frac{3\eta\alpha_l(\omega)}{3\epsilon_0 - \eta\alpha_l(\omega)}, \qquad \text{with} \qquad \alpha_l(\omega) = \frac{p_l(\omega)}{E_{0l}}. \qquad (2.99)$$

Equation (2.99) connects the microscopic polarizability $\alpha(\omega)$ and the associated macroscopic permittivity $\epsilon(\omega)$ and is known as the *Clausius Mosotti relation* [Jac75]. The two expressions for the effective permittivities (2.98) and (2.99) for different number densities are compared in Fig.2.5. In general, it can be concluded that an increasing number density $\eta$ causes a redshift due to increasing effective interaction of metamolecules.

- Considering an isolated ellipsoid rather than an ensemble, the far-field response may

be described best by effective cross sections $C(\omega)$. The scattering cross section $C_{\text{sca}}(\omega)$ is defined by the ratio of the scattered power and the intensity of the incident light (the *irradiance*) yielding values with the units of an area. Similarly, the absorption $[C_{\text{abs}}(\omega)]$ as well as the extinction $[C_{\text{sca}}(\omega) + C_{\text{abs}}(\omega)]$ cross sections are defined. The scattered power is calculated by the poynting vector ($\mathbf{S} = \mathbf{E} \times \mathbf{H}$) which is additionally integrated over the surface of a sphere including the scattering object. Evaluating these quantities with the help of Eqs.(2.58,2.64,2.67,2.95) the cross sections follow after some manipulations [BH83]

$$C_{\text{sca},l}(\omega) = \frac{k(\omega)^4}{6\pi}|\alpha_l(\omega)|^2, \qquad C_{\text{abs},l}(\omega) = k(\omega)\Im[\alpha_l(\omega)], \qquad (2.100)$$

$$C_{\text{ext},l}(\omega) = C_{\text{sca},l}(\omega) + C_{\text{abs},l}(\omega). \qquad (2.101)$$

The cross sections for the ellipsoid with the polarizabilities $\alpha_l(\omega)$, shown in Fig.2.4(A-C) can be evaluated with Eqs.(2.100,2.101). Dividing these cross sections by the geometrical cross sections of the ellipsoid for the respective polarization direction yields the dependencies presented in Fig.2.4(E). As it can be inferred this fraction is larger than unity within the LPP resonance region. In addition, it is depicted by Fig.2.4(A-C) that for a polarization parallel to the larger ellipsoid axis the resonance appears to be increased and redshifted. Furthermore, the ratio between scattered and absorbed light changes as well. For increasing ellipsoid dimensions the extinction cross section is mainly dominated by scattering, whereas for small ellipsoids absorption is the primary contribution to the total extinction.

Although these conclusions are drawn in the electrostatic limit, these physical properties of LPP resonances hold qualitatively also to understand more complex metamolecules that can only be described numerically. Hence, the above-mentioned properties will be essential in order to understand principle physical mechanisms and effects connected to LPP modes in the following chapters.

## 2.1.4 Propagating plasmon polaritons

In this section another family of plasmons, termed surface plasmon polaritons (SPP), will be discussed. Beyond the possibility to enhance and localize light in the vicinity of metal particles, localization can also occur on low-dimensional, i.e., one dimensional systems. Prototypical examples of such systems are metal films embedded in dielectrics (*insulator metal insulator*: IMI) or their inverse (*metal insulator metal*: MIM) configurations, see Fig.2.6(H). Considering a localized surface mode at a metal film parallel to the $xy$-plane the macroscopic magnetic field might be described by the ansatz [BSA86]

$$\mathbf{H}(\mathbf{r}, t) = \mathbf{C}f(z)e^{ik_x x - i\omega t}. \qquad (2.102)$$

In Eq.(2.102) the vector $\mathbf{C}$ is constant and accounts for the correct units, here [A/m]. Furthermore, $\mathbf{C}$ is zero in $x$ and in $z$ direction for propagation in this plane, making the considered solutions *transverse magnetic* modes. This can be verified by plugging this ansatz into the homogeneous Maxwell equation (2.8) and requiring general solutions [$k_x \neq 0$, and $\partial_z f(z) \neq 0$]. Due to the in-plane translational invariance the propagation direction can be fixed parallel to one axis, i.e., the $x$-axis. The associated electric fields in Fourier domain follow from the second curl Maxwell equation (2.7) and the constitutive relation (2.53)

$$\mathbf{E}(\mathbf{r}, \omega) = \frac{i}{\omega \epsilon_0 \epsilon(\omega)} \nabla \times \mathbf{H}(\mathbf{r}, \omega). \tag{2.103}$$

Now, the remaining task is to determine the functional dependence $f(z)$ describing the field decay inside and away from the guiding layer of the thickness[6] $h$

$$f(z) = \begin{cases} e^{k_{z1}z} & , \forall \quad z \leq 0, \\ \cosh(k_{z2}z) + \frac{k_{z1}\epsilon_2}{k_{z2}\epsilon_1} \sinh(k_{z2}z) & , \forall \quad 0 < z \leq h, \\ \left[ \cosh(k_{z2}h) + \frac{k_{z1}\epsilon_2}{k_{z2}\epsilon_1} \sinh(k_{z2}h) \right] e^{-k_{z3}(z-h)} & , \forall \quad z > h. \end{cases} \tag{2.104}$$

The function $f(z)$ in Eqs.(2.104) is chosen to fulfill the criteria for a steady transition of the tangential magnetic field ($H_y$) at the interfaces at $z = 0$ and $z = h$. The remaining boundary condition for a continuous behavior of the tangential electric field ($E_x$) will then provide the solutions for $k_x(\omega)$ for the selected field profile. The wave equation can be obtained for each homogeneous layer by combining macroscopic Maxwell's equations (2.6-2.9) and constitutive relations (2.55,2.56)

$$\nabla \times \nabla \times \mathbf{E}(\mathbf{r}, \omega) - \frac{\omega^2}{c^2} \epsilon_l(\omega) \mathbf{E}(\mathbf{r}, \omega) = 0, \qquad [\nabla \cdot \epsilon_0 \epsilon(\omega) \mathbf{E}) \overset{!}{=} 0], \tag{2.105}$$

$$\Delta \mathbf{E}(\mathbf{r}, \omega) + \frac{\omega^2}{c^2} \epsilon_l(\omega) \mathbf{E}(\mathbf{r}, \omega) = 0, \qquad l \in [1, 2, 3]. \tag{2.106}$$

Thereby, it has been assumed that no external currents or charges are present and that it is sufficient to consider materials in the electric dipole limit ($\mathbf{M} = 0$, $\hat{\mathbf{Q}} = 0$). According to Eq.(2.103) the electric field in the respective layer can be applied to get the dispersion relation, connecting $k_z(\omega)$, $\epsilon_l(\omega)$ and $k_x(\omega)$

$$k_{zl}^2(\omega) - k_x^2(\omega) = -\frac{\omega^2}{c^2} \epsilon_l(\omega), \qquad l \in [1, 2, 3]. \tag{2.107}$$

With Eqs.(2.107) the implicit defining equation for $k_x(\omega)$ can be obtained from evaluating the boundary condition for the tangential electric fields

$$\tanh(k_{z2}h) = -\frac{k_{z3}k_{z2}\epsilon_1\epsilon_2 + k_{z1}k_{z2}\epsilon_2\epsilon_3}{k_{z2}k_{z2}\epsilon_1\epsilon_3 + k_{z1}k_{z3}\epsilon_2\epsilon_2}. \tag{2.108}$$

Starting from Eq.(2.108) two important special cases are considered in the following: the *single*

---

[6]The frequency argument ($\omega$) has been dropped in Eq.(2.104) and Eq.(2.108) for the sake of clarity.

*interface surface plasmon polariton* and the case of *symmetric embedding* $[\epsilon_1(\omega) = \epsilon_3(\omega)]$.

- Starting with the *single interface plasmon* one can consider Eq.(2.108) in the limit of large film thicknesses $h$. For this limit the asymptotic behavior for the hyperbolic tangent function can be applied $\tanh(x)|_{x\to\infty} = 1$. Hence, the defining equation for $k_x(\omega)$ can be rewritten as

$$[k_{z3}(\omega)\epsilon_2(\omega) + k_{z2}(\omega)\epsilon_3(\omega)][k_{z1}(\omega)\epsilon_2(\omega) + k_{z2}(\omega)\epsilon_1(\omega)] = 0, \qquad (2.109)$$

which is mutually fulfilled if at least one expression of the two brackets becomes zero. Using the relations (2.107) to get $k_x(\omega)$ at the respective interface $(1,2)$ or $(3,2)$ yields the important single interface surface plasmon dispersion relation [BSA86]

$$k_x^{(l2)}(\omega) = \frac{\omega}{c}\sqrt{\frac{\epsilon_l(\omega)\epsilon_2(\omega)}{\epsilon_l(\omega) + \epsilon_2(\omega)}}, \qquad l \in [1,3]. \qquad (2.110)$$

Furthermore, one can draw the important conclusion that one of the layers must have a negative real part of the electric permittivity like in the case of the LPP modes before, see section 2.1.3. Combining Eq.(2.110) and Eq.(2.107) one can write

$$k_{z1}(\omega) = \frac{\omega}{c}\sqrt{\frac{-\epsilon_1^2(\omega)}{\epsilon_1(\omega) + \epsilon_2(\omega)}}. \qquad (2.111)$$

Now, if $\Re[\epsilon_1(\omega)] > 0$, which corresponds to an arbitrary dielectric for frequencies far away from any material resonance, $\epsilon_2(\omega)$ should be negative such that $\epsilon_1(\omega) + \epsilon_2(\omega) < 0$. In this case the solutions for $k_{z1}(\omega)$ have a positive real part and guarantee guided modes with evanescent field decay according to Eqs.(2.103,2.104). Though only shown for single interface surface plasmons, it can be generalized that for the second family of plasmons, i.e., surface plasmon polaritons, metals represent suitable materials for their existence in the same manner as for LPPs. It is worth noting that in contrast to LPPs, SPPs are existing typically in a much broader spectral range compared with LPPs.

- The second important implication is the case of a *symmetric embedding* of the guiding layer. Hence, the general relation (2.108) can be further simplified for $\epsilon_1(\omega) = \epsilon_3(\omega)$ and one obtains

$$\tanh[k_{z2}(\omega)h] = -\frac{2k_{z2}(\omega)k_{z1}(\omega)\epsilon_1(\omega)\epsilon_2(\omega)}{k_{z2}^2(\omega)\epsilon_1^2(\omega) + k_{z1}^2(\omega)\epsilon_2^2(\omega)}. \qquad (2.112)$$

Eq.(2.112) can be simplified using the identity for the *hyperbolic tangent*

$$\tanh(x) = \frac{e^x - e^{-x}}{e^x + e^{-x}} = \frac{e^{2x} - 1}{e^{2x} + 1}, \qquad (2.113)$$
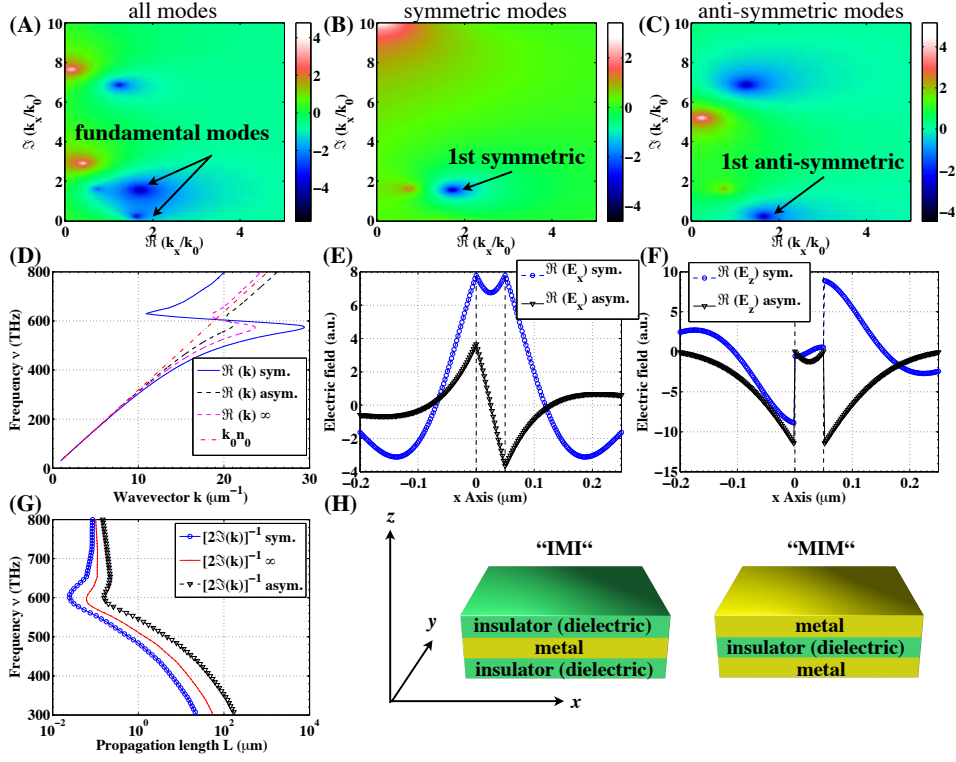
**Figure 2.6:** (A) Results of the evaluation of Eq.(2.108), (B) for the symmetric, and (C) for the anti-symmetric modes according to Eqs.(2.115, 2.116) for a 50 nm thick gold layer embedded in two equal halfspaces with $n = 1.5$. The blue spots represent solutions of the respective equation $\{\log[\|f(k_x)\|]\}$. (D) The real part of the propagation constant $k_x(\omega)$ for these modes as well as the free space dispersion relation and $k_x(\omega)$ for the single interface SPP. (E) The $x$-component of the electric field and (F) the $z$-component for the fundamental symmetric and anti-symmetric modes. (G) The propagation length (logarithmic $x$-scale) for the two modes compared to the single interface SPP. (H) Sketch of the two systems, metal insulator metal (MIM) and the inverse setup metal insulator metal (MIM).

giving

$$e^{k_{z2}(\omega)h} = \pm\frac{k_{z2}(\omega)\epsilon_1(\omega) - k_{z1}(\omega)\epsilon_2(\omega)}{k_{z2}(\omega)\epsilon_1(\omega) + k_{z1}(\omega)\epsilon_2(\omega)}. \tag{2.114}$$

It can be seen that the original set of solutions can be separated into two types of solutions ("+" and "-"). Substituting Eq.(2.114) into Eq.(2.113) by replacing $x$ by $k_{z2}(\omega)h/2$ yields for "+"

$$\tanh\left[\frac{k_{z2}(\omega)h}{2}\right] = -\frac{k_{z1}(\omega)\epsilon_2(\omega)}{k_{z2}(\omega)\epsilon_1(\omega)}, \tag{2.115}$$

and for "-"

$$\coth\left[\frac{k_{z2}(\omega)h}{2}\right] = -\frac{k_{z1}(\omega)\epsilon_2(\omega)}{k_{z2}(\omega)\epsilon_1(\omega)}. \tag{2.116}$$

To illustrate the advantage of such a separation, a 50 nm thick gold layer embedded in a dielectric medium with a non-dispersive refractive index of $n = 1.5$ has been assumed to

calculate the dispersion relation (2.108) as well as the two separated solutions according to Eqs.(2.115,2.116). Results are shown in Fig.2.6(A-C) for a constant frequency of 600 THz. It can be seen that the general equation contains all solutions, indicated by the blue spots compared with the split approach. Regarding the field distribution for the first two modes that are determined by different imaginary parts, it can be seen that symmetric and anti-symmetric modes with respect to the tangential electric fields emerge, see Fig.2.6(E). These modes can be either described by Eq.(2.115) if they are symmetric or Eq.(2.116) if the $z$-component of the electric field is anti-symmetric. Thus, for numerical calculations[7] it is beneficial to use the split formalism, since then all points representing solutions for the dispersion relation are better separated and reduce potential numerical errors. Furthermore, both modes comprise different dispersion in the propagation vector $k_x(\omega)$ as it can be seen from Fig.2.6(D). Considering the imaginary part of this propagation vector the propagation length of the respective mode

$$L \equiv \frac{1}{\Im[2k_x(\omega)]}, \tag{2.117}$$

can be estimated [Rae88]. Evaluating Eq.(2.117) for the fundamental modes and the case of the single interface plasmon one ends up with the propagation length plotted in Fig.2.6(G). The symmetric mode has a shorter propagation length for all frequencies when compared to the anti-symmetric mode and the single interface SPP. The increased propagation length of the anti-symmetric mode is frequently explained by the electric field distribution which has a zero and thus less confinement in the lossy metal in contrast to the electric field of the symmetric mode. Hence, typical propagation lengths range from several nanometers up to hundred microns, depending on the frequency.

Finally, there are two more important peculiarities of SPPs considering the local field enhancement and their excitation. First, the real part of the propagation constant below frequencies where $\epsilon_1(\omega) + \epsilon_2(\omega) < 0$ is always on the right side of the free space dispersion relation $\frac{\omega}{c}n_1(\omega)$. Hence, SPPs cannot be excited with plane waves. For frequencies above this threshold, SPPs become *leaky modes*, i.e., modes that radiate into free space and have an even larger imaginary part in $k_x(\omega)$. To overcome the excitation problem with plane waves various excitation regimes have been developed utilizing, e.g., grating couplers, attenuated total internal reflection, prisms, etc. [Rae88]. One important technique for this work is the so-called *end fire coupling* [BSA86]. Thereby the translational invariance of the infinite planes is broken on one side and the plane wave illuminates the end facets of the layer system. From this side the $k$-vector mismatch results only in a non-zero back reflection, but SPP modes can be excited depending on the symmetry of the illumination, i.e., the angle of incidence or the polarization state.

The second important point is the discontinuity of the component normal to the surface, e.g., see Fig.2.6(F). This discontinuity allows an electric field enhancement localized at the metal

---

[7]Here an adaptive simplex method has been applied which is able to calculate the shown dispersion relations with an appropriate numerical accuracy [$\Delta k_x(\omega)/k_x(\omega) \approx 10^{-4}$].

surface that is typically applied in various systems, e.g., Surface-Enhanced Raman Scattering, nonlinear optics, etc. [Rae88].

## 2.1.5 Rigorous numerical methods

In this section two very important numerical solution schemes that are widely applied throughout this work are introduced: The *Fourier Modal Method* (FMM) and the *Finite Difference Time Domain* (FDTD) method. Instead of presenting the exact derivation and implementation schemes here, the two approaches are described briefly supported by examples that correspond to problems whose solution has been found analytically in the previous sections. It is furthermore mentioned that in the field of nanoplasmonics and metamaterials the two presented methods correspond to standard tools that are frequently applied to solve various problems.

**Fourier Modal Method**

The most appealing aspect on the Fourier Modal Method, also known as *Rigorous Coupled Wave Analysis* (RCWA), especially when compared to the FDTD, is that it constitutes a frequency domain method. Hence, a solution for the wave propagation that is based on macroscopic Maxwell's equations computed in Fourier domain. Thereby the structures interacting with the electromagnetic fields are described by an electric permittivity distribution in reciprocal space and frequency according to

$$\epsilon(\mathbf{r}, \omega) = \frac{1}{\Lambda_x \Lambda_y} \sum_{K_x \in S_x} \sum_{K_y \in S_y} \epsilon(K_x, K_y, \omega) e^{iK_x x} e^{iK_y y}. \tag{2.118}$$

An example of such a 2D distribution is sketched in Fig.2.7(A). Similar to that expansion for the structure, the electromagnetic fields, denoted as $\mathbf{G}$, inside the structure are equivalently assumed to be decomposable in form of

$$\mathbf{G}(\mathbf{r}, \omega) = \frac{1}{\Lambda_x \Lambda_y} \sum_{K_x \in S_x} \sum_{K_y \in S_y} \mathbf{G}(K_x, K_y, \omega) e^{iK_x x} e^{iK_y y}. \tag{2.119}$$

Considering Eqs.(2.118,2.119) there are a few important aspects to be mentioned. First, the requirement for the Fourier decomposition is that the structure is arranged periodically. The periods for a planar structure oriented parallel to the $xy$-plane are denoted as $\Lambda_x$ and $\Lambda_y$. Second, the spatial frequencies, or spatial harmonics $K_{x,y}$, have to be elements of a certain parameter space $S_{x,y}$ which for the FMM is naturally provided by integer numbers multiplied by the respective inverse grating vector $\Gamma_{x,y} \equiv 2\pi/\Lambda_{x,y}$ known as the *Floquet theorem* [TW97]. Since for numerical simulations the corresponding infinite sums over all these values have to be approximated by calculating only finite sums, the FMM accuracy is limited by the number of Fourier orders. Hence, for a particular problem the number of considered orders determines the structural resolution as well as the resolution of the fields inside the modulated area. For simplicity the FMM is explained for 2D systems [Fig.2.7(B)] (translational invariance in $y$-
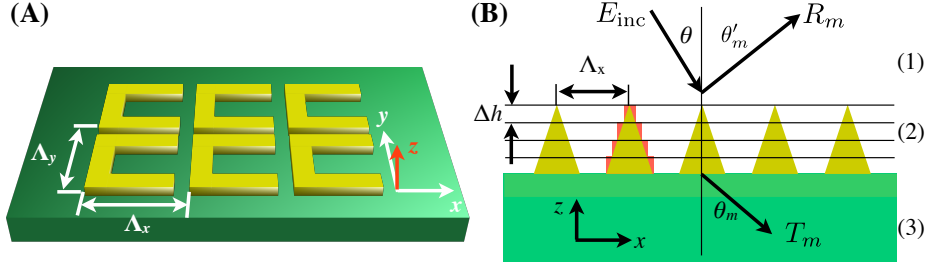
**Figure 2.7:** (A) 2D periodic unit cell of a typical structure for FMM simulations. (B) The definition of the illumination conditions as well as the approximation scheme required for varying structures in propagation direction.

direction) in the following as initially presented by the *Moharam* and *Gaylord* in 1981 [MG81]. Thus, the tangential electric fields in the homogeneous regions above (1) and below (3) the modulated layers may be written for transversal electric polarization (TE) as

$$E_y^{(1)}(x, z, \omega) = E_{\text{inc}} e^{ik_0 n_1 \sin(\theta)x + i\gamma_0 z} + \sum_{m=-\infty}^{\infty} R_m e^{i\alpha_m x - \rho_m z}, \tag{2.120}$$

$$E_y^{(3)}(x, z, \omega) = \sum_{m=-\infty}^{\infty} T_m e^{i\alpha_m x + \tau_m z}, \qquad k_0 \equiv \frac{2\pi}{\lambda}, \tag{2.121}$$

with

$$\alpha_m \equiv k_0 n_1 sin(\theta) + \frac{2\pi m}{\Lambda_x}, \tag{2.122}$$

$$\rho_m \equiv \sqrt{(k_0 n_1)^2 - \alpha_m^2} \qquad , \tau_m \equiv \sqrt{(k_0 n_3)^2 - \alpha_m^2}. \tag{2.123}$$

The angle of incidence is denoted by $\theta$, while the refractive index of the associated homogeneous layer (1) is $n_1$ and for layer (3) is $n_3$. In order to describe the fields inside the modulated region (2) the wave equation (2.106) is

$$\left[ \frac{\partial^2}{\partial x^2} + \frac{\partial^2}{\partial z^2} + \frac{\omega^2}{c^2} \epsilon_2(x, \omega) \right] E_y^{(2)}(x, z, \omega) = 0. \tag{2.124}$$

Performing the spatial Fourier transformation (2.52) provides the solution of Eq.(2.124)

$$E_y^{(2)}(x, z, \omega) = \sum_{m=-\infty}^{\infty} E_m e^{i\alpha_m x + \beta_m z} \tag{2.125}$$

which is conform to the general equation (2.119). The respective boundary conditions allow to formulate an eigenvalue problem from Eq.(2.125), whereas $\beta_m$ represents the eigenvalue and $E_m$ the eigenvector of the respective mode number $m$, which is solved numerically. As a result the electric fields[8] for each mode $m$ in each layer, i.e., the complex values for $R_m$ and $T_m$, as well as the propagation constants $\beta_m$ are obtained. A further direct result of

---

[8]For transversal magnetic polarization (TM) $E_y$ has to be replaced with $H_y$ and the respective boundary condition has to be taken.
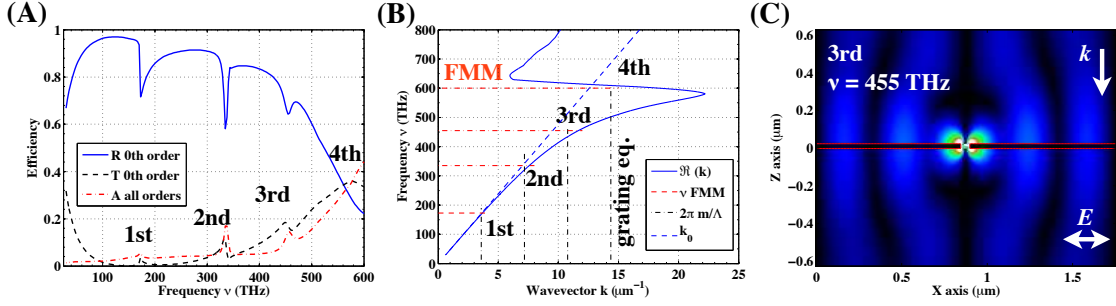
**Figure 2.8:** (A) FMM calculated zeroth order transmission (solid blue), reflection (dashed black) and total absorption (dashed dotted red) spectra including all orders of a metal film incorporating periodically arranged subwavelength slits. (B) The SPP dispersion relation (solid blue) together with the grating vectors $2\pi m/\Lambda$ (dashed dotted blue), the numerically obtained resonance frequencies (red dashed), and the free space dispersion relation for reference (dashed blue). (C) The $z$-component of the electric field modulus for mode $m = 3$ is shown (FMM simulation).

these considerations is an important relation, i.e., the *grating equation*. For their derivation it is sufficient to consider the conservation of momentum parallel to the $xy$-plane. Using this requirement for the electric fields (2.120-2.125) the condition for forward diffracted orders becomes

$$\underbrace{\alpha_m}_{(1)} = \underbrace{\alpha_m}_{(3)}, \tag{2.126}$$

$$k_0 n_1 \sin(\theta) + \frac{2\pi m}{\Lambda_x} = k_0 n_3 \sin(\theta_m). \tag{2.127}$$

The analogous consideration of the backward diffracted orders results in

$$k_0 n_1 \sin(\theta) + \frac{2\pi m}{\Lambda_x} = k_0 n_1 \sin(\theta'_m). \tag{2.128}$$

Though the grating equations (2.127, 2.128) easily allow to predict the diffraction angles, see Fig.2.7(B), the amplitudes $R_m$, $T_m$ require a numerical solution as described above.

As an example for the FMM a SPP propagation is described by calculating a 25 nm thin gold film embedded in vacuum incorporating a 50 nm wide slit. The period $\Lambda_x$ of the periodically repeated unit cell in $x$-direction is 1.75 $\mu$m. The resulting normalized zeroth-order reflectance and transmittance are shown for normal incidence and TM polarization in Fig.2.8(A). Several spectral features can be observed. Additionally the total absorption including all diffraction orders has been plotted showing an enhanced absorption for the resonance frequencies. Calculating the dispersion relation $k_x(\omega)$ [Eq.(2.112)] for the corresponding SPP at an unperturbed flat film yields the propagation constant shown in Fig.2.8(B). Now, if the grating equation is elaborated for the first modes and if additionally the numerically calculated resonance positions are inserted, one observes that the crossings match the SPP line[9]. Hence, one can

---

[9]For mode "4" in Fig.2.8(B) there are two intersections with the SPP line. The low frequency line causes no observable resonance in the spectra, since for this resonance the damping [$\Im(k_x)$] is much larger (not shown here).

anticipate that the grating vector, being the only $k$-vector in $x$-direction in the system, is able to launch SPP's due to the $k$-vector matching at the weakly perturbed metal film, explaining the observed enhanced absorption. This procedure, i.e., considering the grating in terms of the grating equation and utilizing the SPP dispersion relation of a plain metal film in order to describe the composite system is known as the *empty lattice approximation* [CFMW86]. To verify the SPP nature of the obtained resonances rigorously the FMM can be simultaneously utilized to calculate the $z$-component of the electric field for a particular mode ($m = 3$), see Fig.2.8(C). As expected, the evanescent decay away from the surface and away from the slit is observed, which can be attributed to the LPP excitation due to the presence of the grating. Moreover the field seems to be able to penetrate the subwavelength slit aperture and causes localized fields at the back side of the metal film. In passing it is mentioned that beyond the SPP additionally a *quasi-cylindrical mode* [LL08] is launched. In the literature this mode is important to describe the scattered of light after passing through nano-scaled holes and slits [LCXX10]. This mode yields radiation patterns similar to cylindrical waves which can be roughly anticipated from the near-fields in Fig.2.8(C).

Finally, the FMM has been briefly introduced and applied together with the previous considerations of SPP resonances to calculate experimentally accessible values, e.g., far-field intensities, as well as near-field distributions. In the end it is mentioned that state of the art implementation routines differing from the historical approach presented here typically use more stable implementations incorporating spatial adaptive resolution [EB10], coordinate transformations for faster convergence as well as adapted boundary conditions [Lie03, VH02, SLHC01] or even nonlinear optical effects [BT07].

### Finite Difference Time Domain Method

Probably the numerical technique with the lowest number of approximations or manipulations on the original set of Maxwell's equations is the Finite Difference Time Domain method (FDTD). With this method, Maxwell's equations are discretized in space and time applying the transition from analytical to numerical differential operators. Hence, the method is an appropriate tool to simulate an unknown system, since all physics are included. However, the method is approximate as all rigorous schemes due to limitations provided by computational resources like memory or CPU (central processing unit) power, which are finally defining the computational time. For convenience the FDTD will be shortly explained for 3D systems. The two curl Maxwell's equations (2.6,2.7) undergoing spatial and temporal discretization[10]

$$(x, y, z, t) = (\alpha \Delta x, \beta \Delta y, \gamma \Delta z, \delta \Delta t), \tag{2.129}$$

---

[10]For FDTD simulations only the curl equations have to be considered, since the divergence equations are automatically fulfilled by the applied Yee grid [Yee66].
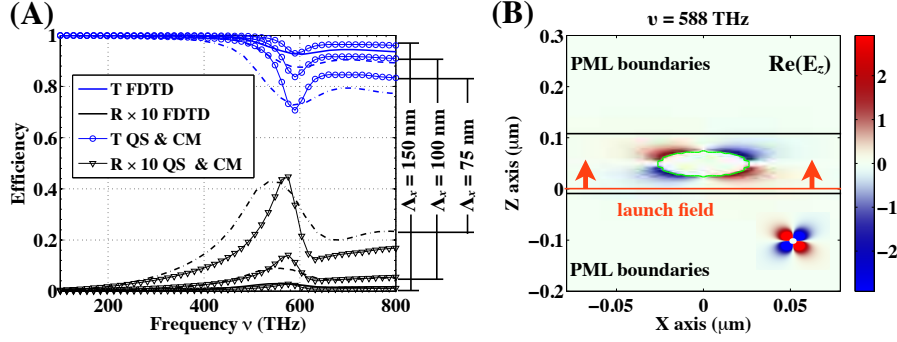
**Figure 2.9:** (A) The far-field observables $T$ and $R$ for a periodic arrangement for gold spheres with a diameter of 50 nm. The calculation has been performed by FDTD (lines) and the LPP model (lines with triangles or circles) utilizing an effective medium according to Eq.(2.99). Therefore three periods (200, 150 and 75 nm) have been investigated. (B) The near-field for the LPP resonance frequency of 588 THz has been computed by FDTD. The inset shows the respective near-field component for an electric dipole, see Fig.2.3.

become for $E_x$ and $H_x$ [Yee66]

$$
\begin{aligned}
E_x\big|_{\alpha,\beta+0.5,\gamma+0.5}^{\delta+0.5} &= E_x\big|_{\alpha,\beta+0.5,\gamma+0.5}^{\delta-0.5} \\
&+ \frac{\Delta t}{\epsilon_0 \epsilon_{\alpha,\beta+0.5,\gamma+0.5}} \left( \frac{H_z\big|_{\alpha,\beta+1,\gamma+0.5}^{\delta} - H_z\big|_{\alpha,\beta,\gamma+0.5}^{\delta}}{\Delta y} - \frac{H_y\big|_{\alpha,\beta+0.5,\gamma+1}^{\delta} - H_y\big|_{\alpha,\beta+0.5,\gamma}^{\delta}}{\Delta z} \right. \\
&\left. - j_x\big|_{\alpha,\beta+1,\gamma+0.5}^{\delta} \right),
\end{aligned}
\tag{2.130}
$$

$$
\begin{aligned}
H_x\big|_{\alpha-0.5,\beta+1,\gamma+1}^{\delta+1} &= H_x\big|_{\alpha-0.5,\beta+1,\gamma+1}^{\delta} \\
&+ \frac{\Delta t}{\mu_0} \left( \frac{H_y\big|_{\alpha-0.5,\beta+1,\gamma+1.5}^{\delta+0.5} - E_y\big|_{\alpha-0.5,\beta+1,\gamma+0.5}^{\delta+0.5}}{\Delta z} - \frac{E_z\big|_{\alpha-0.5,\beta+1.5,\gamma+1}^{\delta+0.5} - E_z\big|_{\alpha-0.5,\beta+0.5,\gamma+1}^{\delta+0.5}}{\Delta y} \right).
\end{aligned}
\tag{2.131}
$$

Analogous expressions are obtained for the remaining field components. However, there are some important points that can be directly inferred by considering Eqs.(2.130, 2.131). First, the structure enters the formalism typically by a spatial electric permittivity distribution, which has to be known in the time domain. Since typically the material permittivity is known in the frequency domain, special dispersion models have to be assumed for which the transformation in time domain can be performed. This is especially of interest if *pulsed*, e.g., Gaussian, *temporal excitation* profiles are considered. For time-harmonic fields, i.e., *continuous wave* propagation, only the permittivity for a particular frequency is needed. Second, the six electric and magnetic field components are not entirely available at the same time and on the same spatial grid. The reason for this is the underlying *leapfrog algorithm* [Taf95] that is applied to calculate the temporal and spatial derivatives. This calculation is performed on two shifted numerical grids which significantly decreases the computational time and improves the stability. Third, quite often the current in Eqs.(2.130) is used to include sources of the field, i.e., the excitation. However, electric field sources are also possible. State-of-the-art implementations include various improvements of the original formulation of the FDTD by [Yee66],

35

such as adaptive spatial resolution [Rem06], the possibility to account for nonlinear optical effects [GT92] and various others [Taf95] that can be found in open source implementations [ORI$^+$10] or commercial products [FDT10]. In order to illustrate the principle operation of the FDTD a periodical arrangement of metal spheres with a diameter of 50 nm and three different periods has been simulated for plane wave illumination. The typical FDTD simulation domain can be seen in Fig.2.9(B). An excitation plane for the launched field, the structure, and proper boundary conditions at the edges of the computational window are labeled. Frequently applied boundary conditions are *periodic boundary conditions* (PBC) or *perfectly matched layers* (PML). The latter provide an exponential decay with suppressed back-reflection from the boundaries which is applied when properties of isolated metamolecules are simulated. The entire computational window is then discretized, denoted by $\Delta x, \Delta y, \Delta z$ in Eq.(2.129). Hence, for each time step $\Delta t$ the entire computational domain has to be stored for all desired field components, as well as the field components that are required for their computation, see e.g., Eqs.(2.130,2.131). Thus, the machine specific available memory is limiting the spatial resolution for numerical computations. Second, the time step $\Delta t$ cannot be chosen arbitrarily, since the numerical speed for the fields propagating with $\Delta r/\Delta t$ can not exceed the maximal phase velocity in the system $\max(v_\text{phase})$ which has been termed the *Courant stability condition*

$$\Delta t \max(v_\text{phase}) < \sqrt{\Delta x^2 + \Delta y^2 + \Delta z^2}. \tag{2.132}$$

Although there are proposed methods to overcome this criterion [ZCZ99], this is still implemented in various codes [FDT10, ORI$^+$10].

As an example the normalized power spectra, monitored on the top and on the bottom of the computational window, for a gold sphere with a diameter of 50 nm has been evaluated for three selected periods ($\Lambda_x = \Lambda_y = 150, 100, 75$ nm). Results are presented in Fig.2.9(A). The spatial resolution for this computation has been set to 2.5 nm in all directions. In order to calculate spectral quantities such as $T$ and $R$ the temporal field evolution has to be Fourier-transformed. Hence, the size of the entire time window $\Delta T = [\max(\delta) - \min(\delta)]\Delta t$ yields the frequency sampling rate $\Delta\nu = 1/\Delta T$. The second limitation beyond the spatial discretization for accurate spectral investigations is the number of time steps $\Delta t$ for which the temporal evolution of the fields is calculated.

For reference, the numerically estimated values for $R$ and $T$ are compared with quasi-static calculations from section 2.1.3. Therefore the Clausius Mosotti relation (2.99) has been applied[11]. As expected, the resonances are shifted towards smaller frequencies for smaller periods, i.e., approaching spheres. The number density for the two-dimensional arrangement of spheres is $\eta = 1/(\Lambda_x\Lambda_y h)$. The line-shapes between the spectra predicted by FDTD and the quasi-static approach differ, which is an effect that occurs due to the size of the spherical metamolecule approaching limits of the validity for the quasi-static treatment. Besides these weak deviations, the near-fields [$\Re(E_z)$] are equivalent to the associated near-field component

---

[11]For the calculation of the reflection and transmission coefficients a standard transfer matrix formalism [BW99] has been used. Thereby, the film thickness has been set to the diameter of the spheres, while the refractive index of the film has been set to $n_\text{eff} = \sqrt{\epsilon_\text{eff}}$.

of the fundamental multipolar contribution, i.e., the electric dipole pattern[12] in Fig.2.3, shown in the inset of Fig.2.9(B).

With the two introduced numerical methods the most important computational techniques are presented that are widely applied in this work. Nevertheless, there are several other numerical solvers for Maxwell's equations that have been successfully applied in the recent research focussing on nanoplasmonics and metamaterials [GKM10, KBN10, Jin93, NH06]. The two methods presented here have been selected since typical experimental samples are characterized by an inherent periodicity (see chapter 2.2). Therefore, the FMM is the method of choice in order to calculate far-field transmission and reflection coefficients. However, for a complete understanding of spectral features of these quantities near-field simulations are indispensable. For this purpose, a second numerical method, i.e., the FDTD, has been presented as a tool to calculate the desired near-field distributions, as well.

Beyond these numerical methods, the analytical considerations introduced in this chapter present the physical basis which helps to understand, interpret and categorized plasmonic effects occurring upon electromagnetic excitation in metamolecules of interest.

## 2.2 Experimental

In this chapter an experimental method is presented, which has been applied to characterize fabricated planar metamaterials optically. In particular, the measured observables of interest in this work are the far-field intensities. Among other physical techniques that are widely applied to optically characterize metamaterials, the intensity measurement can be regarded a rather simple setup. Other frequently applied methods for the optical characterization are spectroscopic ellipsometry [LBB+09], scanning near-field microscopy [BDO+10, BVDZ10, DDLW10] or phase-resolved measurements of the reflection and transmission coefficients [PSSH+10] as well as single particle spectroscopy [HKF+08, BPQL10]. The advantages of the intensity measurement are that the number of potentially occurring errors is comparably low to the before-mentioned setups and that it allows to observe defining spectral features of ensembles of metamolecules.

Nevertheless, this measurement setup has some significant requirements, e.g., the need for samples with a large structured area. There are several reasons for that. At first, the spot size of the illuminating beam can only be focused or confined in the limits of the diffraction limit. For such beam widths the interaction with an isolated metamolecule can be hardly detected by standard schemes and will probably vanish in the noise. Thus, the signal has to be increased by large numbers of metamolecules covering the entire illumination spot size. A second restriction is induced by the requirement for normal incidence as it will be discussed in the forthcoming chapters. Therefore, any focussed illumination on the area covered with the metamaterial should be avoided. Hence, the covered area should be large to use pinholes and

---

[12]The corresponding field component for the electric dipole in Fig.2.3 is the ($E_y$) component due to a different coordinate system in Fig.2.9(B).

other optical elements with a low numerical aperture to allow measurements close to normal incidence.

This again results in a minimal area which should be covered with the metamaterial. Thus, sophisticated fabrication processes enabling for a large area covering of metamaterials are required [BMH+10, HBS+08], which finally allow a rather simple detection scheme for optical measurements.

It is mentioned that both, the details of the fabrication of metamaterials as well as the development of sophisticated measurement setups are beyond the scope of this thesis. The reader is referred to more experimentally oriented publications on these issues [HMR+09, PSSH+10, HBS+08].

In this work the experimental verification of certain spectral effects of particular metamaterials has been performed by means of optical and near-infrared far-field intensity measurements, e.g., for the nanoantenna samples of part 3. For this reason, the applied setup is described in the following section 2.2.1, for completeness.

### 2.2.1 Far-field spectroscopy

The basic setup for the spectrally resolved intensity measurements applied in this work is the *Lambda 950 professional* spectrometer from the *PerkinElmer* company [Perb]. The setup is based on a double-beam spectrometric method, illustrated in Fig.2.10. The double-beam approach allows for a reference measurement for each frequency without removing the sample. This is useful to account for any fluctuations during the measurements, e.g., instabilities of the lamps, etc. Thus, the recorded observable for each frequency is the ratio between the intensity measured in the sample and the reference beam. In order to align the ratio of the two beam paths and to remove the effect of residual ambient or background radiation an initial reference measurement without sample is performed. This initial adjustment can be similarly performed with a substrate without any structuring in order to remove the influence of the substrate. After this step the measurement for the relative and spectrally resolved transmission and reflection intensities can be realized and monitored online.

In the following the beam path of the spectrometer is briefly described in accordance with Fig.2.10. Two lamps represent the illumination. For ultra-violet and visible frequencies a deuterium lamp (a) is applied, while for the smaller frequencies in the visible and infra-red a halogen lamp (b) is used. After passing a rough initial spectral filter (c) the desired frequency is selected by two gratings (d). Thereby, each diffraction order propagates under a certain angle, see Eq.(2.127). Thus, the frequency is adjusted by selecting the respective rotation angle of the diffraction gratings. Afterwards, the beam passes an adjustable slit (e) that can be applied to narrow the frequency band which is propagating under a certain opening angle. At this point it becomes obvious that a precise alignment of a particular frequency coincides with very low illumination intensities. For a high spectral resolution very narrow slit widths have to be applied, which will result in a decrease of the energy passing through the slit. Consequently, for each measurement there is a trade-off between detector
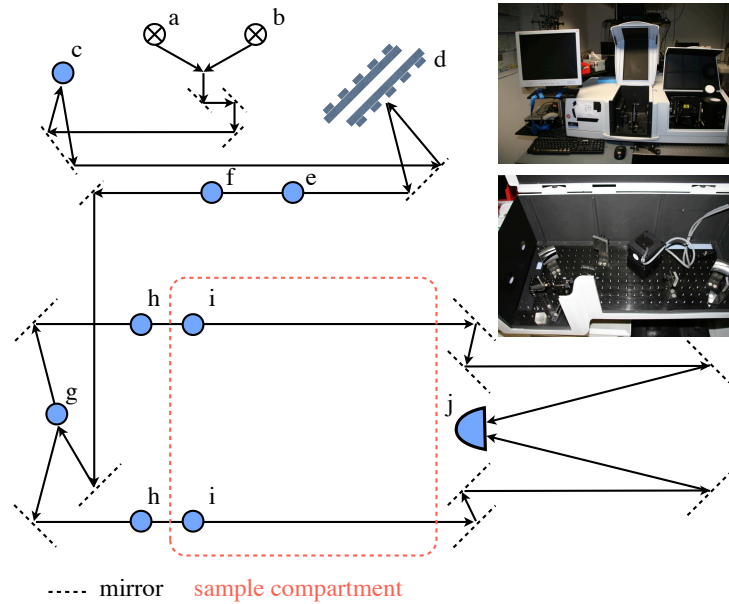
**Figure 2.10:** The principle beam path in the *Lambda 950* spectrometer. The insets show photographs of the spectrometer including the standard (top) and the advanced (bottom) sample compartment.

noise and spectral accuracy. The beam shape can be further modified by a second slit (f) to reduce the beam width in the second transversal direction. Next, the beam passes a depolarizer to remove the residual beam polarization introduced by, e.g., by the gratings, etc. The beam is selectively switched to the reference or the sample beam by a chopper (g). In order to perform measurements with polarized illumination, different types of polarizers can by optionally mounted in the automatic polarizer posts (h). Before the beams are finally detected by either a photo-multiplyer or an *InGaAs* (Indium-Galium-Arsenide) detector, the sample can be optionally mounted in the upper or in the lower path (i). Besides this setup that has been presented for transmission measurements, the beam path can be modified for reflection measurements at oblique incidence, scattering measurements, etc. by adding further items into the sample compartment.

The entire spectral interval provided by the lamps ranges from 175 to 3300 nm. The real measurement interval is reduced to $\approx 280 - 2500$ nm by the sensitivity of the detectors, the transmission window of the substrate, and the specifications of the applied polarizer. The overall accuracy of the entire setup is specified with a relative accuracy of $\leq 2\%$ [Pera].

# 3 Electric dipole excitations in metal nanostructures

## 3.1 Optical properties of dipole nanoantennas

After presenting the fundamental physical concepts, the applied fabrication as well as optical characterization methods in part 2, the following part is related to the first order multipolar response, i.e. *electric dipole excitations*, in detail. The associated metamolecules are termed *dipole nanoantennas* due to their similar radiation and absorption characteristics when compared with dipole antennas in the radiofrequency domain [KKH10, Bal08]. This idea, i.e., the application of the antenna concept in the field of nanooptics, started quite recent by the two seminal works of *Mühlschlegel et al.* [MEM+05] and *Schuck et al.* [SFS+05] in 2005. A profound knowledge about the optical response of nanoantennas operating in the fundamental multipole mode, i.e., the electric dipole, will be essential in order to design and understand the properties of more complex metamolecules [PWAB10, TSS09, PCT+09] entering higher multipole regimes. This will be the subject of the forthcoming part 4.

The content of chapter 3.1 is devoted to the presentation of general optical properties of electric dipole nanoantennas. In chapter 3.2 this knowledge will be applied to design and realize a new type of bio-sensing substrates. For this purpose, particularly arranged ensembles of dipole nanoantennas, providing LPP resonances, are tuned to exhibit SPP excitations, simultaneously. This combination yields multi-resonant plasmonic metamaterials that are successfully applied for *Surface-Enhanced Raman Scattering* (SERS).

### 3.1.1 Near-field enhancement

In order to start with the fundamental LPP resonance, i.e., the electric dipole, simple arrangements of nanoantennas are considered at first. The reason, why such nanoantennas are of special interest, is the possibility to exploit the local field enhancement in the spectral vicinity of LPP resonances as motivated in section 2.1.3. This enhancement provides the playground for a broad band of physical and interdisciplinary applications. Examples are bio-sensing applications [GHMG10], such as Surface-Enhanced Raman Scattering (SERS) [FSD08], non-linear frequency conversion processes [KYF+09], trapping [ZHSM10] or quantum effects, e.g., single photon emission [ETG10]. These typical research topics exploit the field enhancement occurring at optical nanoantennas. For this work, the enhancement will be applied to design improved SERS substrates for bio-sensing and chemical analysis later on. From the viewpoint of physics, there are three different principles that result in a local field enhancement utilizing optical nanoantennas.

- First, the presence of a plasmonic resonance, see section 2.1.3 for LPP resonances and section 2.1.4 for SPP resonances. In principle, both can be utilized to enhance the local

electric fields in a predefined spectral region, whereas LPP resonances are anticipated as the predominant plasmonic effect for an isolated nanoantenna.

- Second, a coupling between two or more closely spaced nanoantennas can enhance the the local field beyond the enhancement of an isolated nanoantenna [FNDM09, AKGQ09].

- Third, field enhancement can be achieved by particular shapes of the nanoantenna. This effect coined the term *lightning rod effect* [GN80, PC85, LW82]. In contrast to the first mechanism, it is a non-resonant effect that can be observed at various structures displaying sharp corners, tips, or rough surfaces.

In order to illustrate all three effects, triangular-shaped nanoantennas will be considered as an example. The triangular shape has been selected since it simultaneously allows for the excitation of LPP resonances and comprises sharp tips [NKS$^+$07]. Moreover, it is a prototypical example for a constituent that can be coupled to a second triangular nanoantenna yielding a system termed *bow-tie nanoantenna* [KYF$^+$09]. The system has been investigated numerically by means of the FMM for the spectral analysis, and the FDTD for the computation of the near-fields. For all simulations a two-dimensional periodic array with a grating period of 400 nm in $x$- and $y$-direction, $n = 1$ as the ambient refractive index, and $n = 1.5$ as the refractive index of the substrate have been assumed.

The nanoantennas are made of gold [JC72] and have a thickness of 25 nm. The propagation is assumed to be normal to the nanoantenna arrays, i.e., parallel to the $z$-direction. The polarization of the electric field has been set either along the $x$- or the $y$-direction. The orientation of the nanoantennas in the $xy$-plane is depicted in Fig.3.1(C). Considering the far-field spectra [Fig.3.1(A,B)], distinct resonances for both the triangular as well as the bow-tie nanoantennas for both polarization directions can be observed. These are associated to the fundamental LPP resonances, i.e., the electric dipole modes, of the nanoantenna for the respective polarization direction. To motivate that the resonances correspond to electric dipole excitations, the $y$-component of the electric field is shown in Fig.3.1(C) for the bow-tie nanoantenna at the resonance frequency for $x$-polarization. The inset in Fig.3.1(C) shows the corresponding radiation pattern of an isolated electric dipole in the near-field zone, as derived in section 2.1.2. It can be easily verified that the near-field patters of the bow-tie nanoantenna match nicely to the electric dipole pattern. It is mentioned that the $y$-component has been selected for this comparison, because it does not contain the impinging transverse electromagnetic fields. Hence, the localized mode can be observed almost undisturbed from the illumination field.

In Fig.3.1(D-F) the moduli of the $x$-polarized electric fields for the three scenarios of field enhancement are shown: (D) due to resonant coupling of the bow-tie nanoantennas with a gap width of 15 nm, (E) due to the LPP resonance of a single triangular nanoantenna, and (F) due to the presence of sharp curvatures at the nanoantenna's surface only, i.e., at the tips of the triangle. For the latter scenario an excitation frequency spectrally well-separated from the LPP resonance has been selected in order to ensure that the effects of the LPP resonance can be safely neglected. The fields have been recorded 5 nm above the nanoantennas. Additionally, the fields have been shown in a $y$-cut through the center of the respective nanoantenna,
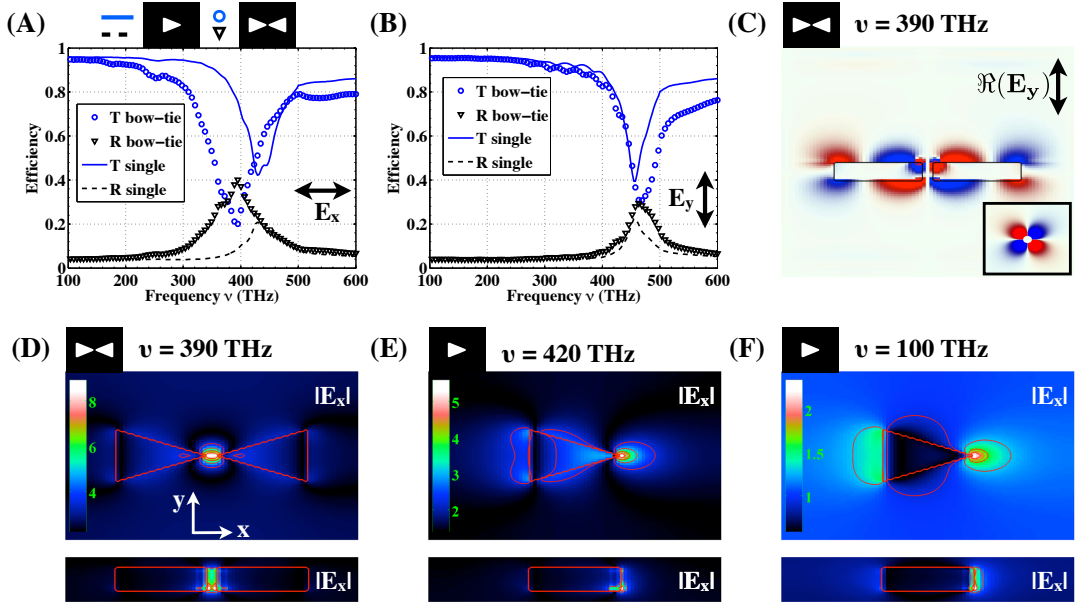
**Figure 3.1:** The spectral reflection (black) and transmission (blue) coefficients for an array of gold triangles and bow-tie nanoantennas computed with the FMM for (A) $x$-polarized electric fields, and (B) for $y$-polarized electric fields. (C) The real part of the $y$-component of the electric field for the bow-tie nanoantennas for the resonance frequency in $x$-polarization. The inset shows the corresponding radiation pattern of an electric dipole, oriented along the $x$-axis, in the near-field zone, see Fig.2.3. (D) The modulus of the $x$-component of the electric field 5 nm above the bow-tie nanoantenna in the resonance for $x$-polarized electric fields. The bottom image shows the modulus of the same field component in a $y$-cut through the center of the bow-tie nanoantenna. (E) The respective field distributions for the triangular nanoantenna at the resonance, and (F) in the off-resonant case.

see small insets at the bottom of Fig.3.1(D-F). For all three scenarios the electric fields are enhanced as $|E_x/E_{x0}|$ exceeds unity. Furthermore, the field enhancement factor directly at the tips of the triangles is $\approx 40$ for the resonant excitation, $\approx 8$ for the off-resonant excitation, and $\approx 50$ in the gap for the bow-tie setup at the resonance frequency.

For the coupled bow-tie nanoantannas there is one more peculiarity to be mentioned, which is a generic property of coupled electric dipole nanoantennas and which manifests in the far-field spectra in Fig.3.1(A,B). It can be seen that the resonance frequencies of the bow-tie nanoantenna system appears to be either *red-shifted*, i.e., shifted toward smaller frequencies, or *blue-shifted*, i.e., shifted toward larger frequencies, depending on the incident polarization when compared with the uncoupled triangular nanoantenna's resonance frequencies. In particular, the *in-line excitation* ("→→"), i.e., Fig.3.1(A), is energetically easier to excite and hence appears at lower frequencies due to the attraction of opposite charges of the two dipoles. In contrast, the *side-by-side excitation* ("↑↑"), i.e., Fig.3.1(B), appears at higher frequencies due to the rejection of the two facing and equally charged carriers of the dipoles[1].

To get a additional insights into the underlying physical principles of the field enhancement at nanoantennas, an ellipsoidal dipole nanoantenna will be analytically investigated with the LPP model introduced in section 2.1.3. The local field of a metal ellipsoid in the electrostatic

---

[1]A comprehensive investigation on the coupling of nanoantennas with different shapes and orientations that is sometimes referred to as *plasmon hybridization*, has been performed by *Davis et al.* [DGV10].

description according to Eq.(2.97) can be rewritten as

$$\mathbf{E}_{\mathrm{p}}(\xi, \eta, \zeta, \omega) = \frac{\epsilon_{\mathrm{i}}(\omega) - \epsilon_{\mathrm{a}}(\omega)}{\epsilon_{\mathrm{a}}(\omega) + L_z[\epsilon_{\mathrm{i}}(\omega) - \epsilon_{\mathrm{a}}(\omega)]} \frac{a_x a_y a_z}{2} \nabla \left[ \Phi_0 \int_{\xi}^{\infty} \frac{du}{(a_z^2 + u) f(u)} \right]. \tag{3.1}$$

The resonant behavior of the first term has already been discussed in section 2.1.3. It can be considered as the *dispersive enhancement* since it can be interpreted as the geometrically induced resonance control, mediated by the factor $L_z$. Hence, the shape of the ellipsoid controls the resonance position, at which the LPP emerges, and thus, at which frequency the local field is enhanced. The second term is a purely geometry-dependent factor that is sometimes referred to as the *lightning rod factor* [LW82]. In the following, it will be briefly shown that this factor provides a field localization and enhancement, as observed for the off-resonant excitation of the nanoantenna example above [Fig.3.1(F)]. For the last expression in Eq. 3.1 one can simplify to

$$\frac{a_x a_y a_z}{2} \nabla \left[ \Phi_0 \int_{\xi}^{\infty} \frac{du}{(a_z^2 + u) f(u)} \right]_{\xi=0} = E_0 \left[ -L_z \mathbf{e}_z + \frac{a_x a_y a_z}{2} z \nabla \int_{\xi}^{\infty} \frac{du}{(a_z^2 + u) f(u)} \bigg|_{\xi=0} \right]. \tag{3.2}$$

By using the relation $\partial_x \int_{f(x)}^{\infty} g(u)\ du = -g[f(x)] \partial_x f(x)$ for continuously differentiable functions $g(x)$, $f(x)$ and Eqs.(2.92) the second part in the sum of Eq.(3.2) becomes

$$\frac{a_x a_y a_z}{2} z \nabla \int_{\xi}^{\infty} \frac{du}{(a_z^2 + u) f(u)} \bigg|_{\xi=0} = -\frac{z}{2 a_z^2} \nabla \xi. \tag{3.3}$$

Now, the problem is to calculate the gradient of the elliptical coordinate $\xi$ which is given as a solution to

$$\frac{x^2}{a_x^2 + \xi} + \frac{y^2}{a_y^2 + \xi} + \frac{z^2}{a_z^2 + \xi} = 1. \tag{3.4}$$

Instead of solving Eq.(3.4), which is quite challenging, and applying the differential operator $\nabla$ it is very easy to compute the gradient of $\xi$ by a differentiation of Eq.(3.4) for each cartesian component, directly which gives[2]

$$[\nabla \xi]_\alpha = \frac{2 r_\alpha \mathbf{e}_\alpha}{a_\alpha^2 + \xi} \left[ \frac{x^2}{(a_x^2 + \xi)^2} + \frac{y^2}{(a_y^2 + \xi)^2} + \frac{z^2}{(a_z^2 + \xi)^2} \right], \text{ with } \alpha \in [x, y, z]. \tag{3.5}$$

---

[2]Since the explicit form of $\xi$ is not required, this step simplifies the derivation significantly.
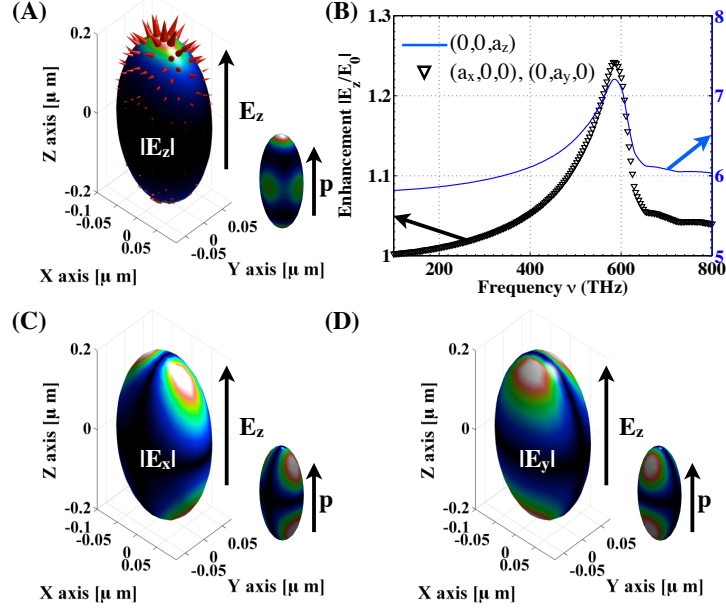
**Figure 3.2:** The electric field distributions of an ellipsoid oriented in $z$-direction at the surface: (A) The modulus of $E_z$, (C) the modulus of $E_x$, and (D) the modulus of $E_y$ at the resonance frequency of $\nu = 590$ THz. The arrows in (A) denote the vectorial electric field. (B) The electric field enhancement for $E_z$ at the tips of the ellipsoid according to Eq.(3.6). The insets in (A,C,D) represent the field distributions of an electric dipole calculated at an external spherical surface that is finally mapped at the surface of an ellipsoid by coordinate transformation.

With the above considerations it is possible to calculate the electric fields at the entire surface of an arbitrary ellipsoid, which is described by $\xi = 0$

$$
\begin{aligned}
\mathbf{E}_{\mathrm{p}}(0, \eta, \zeta, \omega) \;=\; & E_0 \frac{\epsilon_{\mathrm{a}}(\omega) - \epsilon_{\mathrm{i}}(\omega)}{\epsilon_{\mathrm{a}}(\omega) + L_z[\epsilon_{\mathrm{i}}(\omega) - \epsilon_{\mathrm{a}}(\omega)]} \left[ \frac{a_x^4 a_y^4 a_z^4}{x^2 a_y^4 a_z^4 + y^2 a_x^4 a_z^4 + z^2 a_x^4 a_y^4} \right. \\
& \times \left. \frac{z}{a_z^2} \begin{pmatrix} \frac{x}{a_x^2} \\ \frac{y}{a_y^2} \\ \frac{z}{a_z^2} \end{pmatrix} - L_z \mathbf{e}_z \right].
\end{aligned}
\tag{3.6}
$$

Typically this field is only computed at selected points of the ellipsoid, i.e., the tips or along the minor equator, which is defined as the ellipse spanned by the two minor axes of the ellipsoid. In order to illustrate the lightning rod effect and to discuss the field enhancement in terms of the electric dipole moment, all three field components have been calculated at the entire surface of a particular ellipsoid with $a_x = 100$ nm, $a_y = 75$ nm, and $a_z = 200$ nm. Since the dispersive enhancement does not depend on the spatial coordinates it has been set to unity. Results are shown in Fig 3.2. In Fig.3.2(A) the $z$-component of the electric field, being the incident polarization direction, is encoded by the surface color, while the red arrows correspond to the entire vectorial electric field and their length accounts for the magnitude. It can be clearly seen that the electric fields are enhanced and localized at the tips of the ellipsoids. Moreover, the effect of the lightning rod factor, which is corresponding to the fields at the surface, as introduced before, becomes obvious. Furthermore, the electric fields in $z$-direction are also enhanced at the minor equator of the ellipsoid, e.g., at $(a_x, 0, 0)$, $(0, a_y, 0)$.

To illustrate this and to include also the dispersive enhancement for realistic materials, gold has been used as the bulk permittivity $\epsilon_i(\omega)$ for the ellipsoid, while $\epsilon_a(\omega)$ has been set to unity, see Fig.3.2(B). At the frequency where the denominator of the dispersive enhancement, i.e., $\epsilon_a(\omega) + L_z[\epsilon_i(\omega) - \epsilon_a(\omega)]$, becomes zero, the electric fields are enhanced at the tip $(0, 0, a_z)$ as well as at the minor equator at $(a_x, 0, 0)$, $(0, a_y, 0)$ of the ellipsoid.

To clarify the electric field patterns of the ellipsoid, that have been obtained by the solution of the electrostatic Laplace equation (2.80), the corresponding electric field distributions for an electric dipole have been calculated at the surface of a sphere with Eqs.(2.64, 2.67). In a final step, these have been mapped on the surface of the same ellipsoid as computed before by simple coordinate transformation. For an electric dipole oriented in $z$-direction the results are shown in the insets of Fig.3.2(A,C,D). It can be seen that the radiation patterns of both fields match nicely, which is a further proof of the dipolar nature of the considered elliptical nanoantennas. In addition, Eq.(3.6) together with the electric dipole fields in Fig.3.2(C,D) yields a simple explanation for the occurrence of electric field components that are not included in the excitation, e.g., $E_x$, $E_y$. These two field components are not provided by the excitation, but are induced by the localized electric dipole mode.

In this section the near-field enhancement, being the dominant physical effect for the application of dipole nanoantennas, has been presented. Numerical simulations have been performed that provide exact results in terms of the spectral far-field and near-field response. In a second step, the LPP model has been utilized to explain the physics for the simplified case of elliptical dipole nanoantennas. Although this is an approximation, physical consequences could be derived that help to understand and interpret the numerical data for more complex nanoantennas, and finally are required for a specific design for nanoantennas with predefined optical properties.

### 3.1.2 Polarization dependence

In section 3.1.1 a comprehensive investigation of the near-field characteristics for dipole nanoantennas has been performed. The intention of the present section is to understand their *excitation* properties. For this purpose, the effect the incident polarization orientation on the excitation of the dipole nanoantennas will be considered. The associated results and conclusions of this analysis will be of interest in the following chapter.

This investigation, similar to the previous section, will be performed numerically for a particular nanoantenna, i.e., the bow-tie nanoantenna, before the analytical LPP model for ellipsoids will be applied to explain the observed behavior. For the numerical simulations, the bow-tie nanoantennas from the previous section are used. The FMM is applied to numerically calculate the spectrally resolved reflection and transmission coefficients at normal incidence, but with changing polarization angle $\theta_1$, see principle setup at the top of Fig.3.3(C). Results for the far-field spectra in steps of $\Delta\theta_1 = 15°$ are shown in Fig.3.3(A). The red and the black lines represent the spectral absorption coefficients $1 - T - R$, for $x$-polarization ($\theta_1 = 0°$) and $y$-polarization ($\theta_1 = 90°$), respectively. It can be clearly seen that by changing the polarization

between these angles the absorption coefficients for the bow-tie antenna changes continuously from the value at the resonance frequencies for 0° toward the value at the 90° resonance, see blue-dashed lines in Fig.3.3(A). Strictly speaking, the LPP resonance frequencies are fixed, but their excitation strengths are varying.

It is mentioned that plasmonic resonances comprise radiative losses due to enhanced scattering, as well as dissipative losses, i.e. non-radiative absorption of energy in the metal [SFW+02]. Consequently, by considering the transmission and reflection coefficients for a certain nanoantenna ensemble, an enhanced absorption is expected for frequencies close to the excitation of LPP resonances. Thus, the absorption can be regarded as an appropriate quantity to describe the excitation strength for the LPP resonances of the considered bow-tie nanoantennas for a particular excitation [Gri09].

Moreover, the LPP resonances of the bow-tie nanoantennas investigated here are *orthogonal*, since an isolated observation of each resonance is possible at polarization angles of 0° and 90°. Hence, the polarization eigenstates of the bow-tie nanoantennas are *linearly polarized* as long as the cross-polarized coefficients $T_{i,j}$, $R_{i,j}$, with $i, j \in [x, y] : i \neq j$ are zero. If the LPP modes are associated with electric dipole modes, their molecular dipole moment is expected to be proportional to the elongation of the internal metal carriers [Eq.(2.28)] which is proportional to the external electric field [Eq.(2.5)]. Hence, the projection of the electric field onto the electric dipole modes of the bow-tie nanoantennas in $x$- and $y$-direction is responsible for the excitation of the two LPP modes. In addition, the intensity is proportional to the square of the modulus of the electric field. Thus, the spectral response for a particular polarization angle $\theta_1$ and frequency $\omega_0$ may be expected to have the form

$$I(\omega_0, \theta_1) = I(\omega_0, 0°) \cos^2(\theta_1) + I(\omega_0, 90°) \sin^2(\theta_1). \qquad (3.7)$$

To verify this assumption, the absorption dependence on the polarization angle for the resonance frequency along the $x$-axis, see blue solid line, and for the off-resonant case, see red dotted line in Fig.3.3(B), have been calculated with Eq.(3.7). Therefore, the required values for $I(\omega_0, 0°)$ and $I(\omega_0, 90°)$ at the LPP resonance frequency, see Fig.3.3(A), have been taken and used to calculate those of all other polarization angles. In addition, the absorption has been calculated for the resonance frequency for $x$-polarization at discrete polarization angles with the FMM. As can be seen, the continuous line corresponding to Eq.(3.7) matches nicely to the numerical data represented by the black triangles. Furthermore, these calculations prove that the spectral quantities at a polarization of 0° and 90° form a complete set of eigenstates for normal incidence, since the optical response for arbitrary polarization angles can be determined[3] from Eq.(3.7).

Now, the LPP model for ellipsoids will be applied to complete the description of the excitation properties of dipole nanoantennas which is in line with all considerations performed above. Such a model is of importance, since it gives insights into the underlying physics of

---

[3]It is mentioned that there is one remaining dipolar LPP mode along the $z$-axis. For completeness this has to be taken into account as well. But this mode cannot be probed at normal incidence.
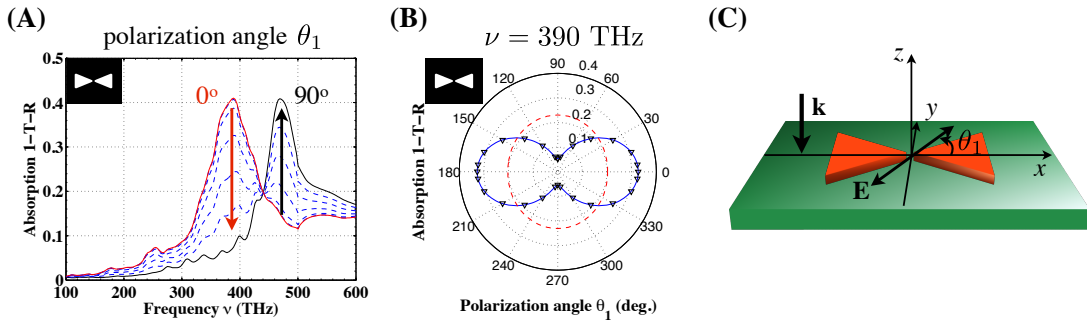
**Figure 3.3:** (A) The influence of the variation of the polarization angle $\theta_1$ on the spectrally resolved absorption coefficient. (B) The polar representation of the absorption for a changing polarization angle. The red-dashed line accounts for an off-resonant excitation frequency, while the black triangles represent the numerical values for the resonance frequency along the $x$-axis of the bow-tie nanoantennas. Blue solid lines are associated with predictions from Eq.(3.7). (C) Sketch of the bow-tie nanoantennas including the illumination and the definition of the polarization angle.

the investigation performed previously. The molecular electric dipole moment induced in a ellipsoid can be found according to Eq.(2.96) and Eq.(2.99) from section 2.1.3 [BH83]

$$
\mathbf{p}(\omega) = \begin{pmatrix} \alpha_x(\omega) & 0 & 0 \\ 0 & \alpha_y(\omega) & 0 \\ 0 & 0 & \alpha_z(\omega) \end{pmatrix} \mathfrak{E}(\omega) \equiv \hat{\alpha}(\omega)\mathfrak{E}(\omega), \tag{3.8}
$$

with the polarizability tensor[4] $\hat{\alpha}(\omega)$. Any rotation of the ellipsoid or the external field may be described by the application of a transformation matrix $\hat{U}$. For example a rotation of the polarization of the electric field in the $xy$-plane, as performed above, may be described by

$$
\hat{U}(\theta_1) = \begin{pmatrix} \cos(\theta_1) & -\sin(\theta_1) & 0 \\ \sin(\theta_1) & \cos(\theta_1) & 0 \\ 0 & 0 & 1 \end{pmatrix}. \tag{3.9}
$$

The molecular dipole moment for the rotation with respect to the $z$-axis as described by Eq.(3.9) becomes

$$
\tilde{\mathbf{p}}(\omega) = \hat{U}(\theta_1)\mathbf{p}(\omega). \tag{3.10}
$$

In analogy, the electric field yields

$$
\tilde{\mathfrak{E}}(\omega) = \hat{U}(\theta_1)\mathfrak{E}(\omega). \tag{3.11}
$$

---

[4]Although the polarizabilities have been introduced and discussed for the case of ellipsoids, this consideration holds for arbitrary dipole nanoantennas with linearly polarized eigenstates, i.e., nanoantennas with a diagonal polarizability tensor. The only difference is that for arbitrary nanoantennas, the polarizabilities can no longer be obtained analytically.

Hence, Eq.(3.8), upon performing the respective transformation for $\hat{\alpha}(\omega)$, yields

$$\tilde{\mathbf{p}}(\omega) = \hat{U}^T(\theta_1)\hat{\alpha}(\omega)\hat{U}(\theta_1)\tilde{\mathfrak{E}}(\omega) \equiv \tilde{\hat{\alpha}}(\omega)\tilde{\mathfrak{E}}(\omega). \tag{3.12}$$

In order to quantify the total amount of energy that is scattered or absorbed by an electric dipole with a known molecular dipole moment, described by Eq.(3.8), the effective cross sections as introduced in section 2.1.3 can be applied. With the definitions of the effective scattering and extinction cross sections according to Eq.(2.100) and Eq.(2.101) the effect of a changing polarization angle as described by $\hat{U}(\theta_1)$ in Eq.(3.9) can be computed

$$C_{\text{sca}}(\omega, \theta_1) = \frac{k^4(\omega)}{6\pi}\left|\frac{\tilde{\hat{\alpha}}(\omega)\tilde{\mathfrak{E}}(\omega)}{\tilde{\mathfrak{E}}_x(\omega)}\right|^2 = \frac{k^4(\omega)}{6\pi}\left[|\alpha_x(\omega)|^2\cos^2(\theta_1) + |\alpha_y(\omega)|^2\sin^2(\theta_1)\right], \tag{3.13}$$

$$C_{\text{abs}}(\omega, \theta_1) = k(\omega)\Im\left[\frac{\tilde{\hat{\alpha}}(\omega)\tilde{\mathfrak{E}}(\omega)}{\tilde{\mathfrak{E}}_x(\omega)}\right] = k(\omega)\Im[\alpha_x(\omega)\cos^2(\theta_1) + \alpha_y(\omega)\sin^2(\theta_1)]. \tag{3.14}$$

As a result, the extinction cross section $C_{\text{ext}}(\omega, \theta_1) = C_{\text{sca}}(\omega, \theta_1) + C_{\text{abs}}(\omega, \theta_1)$, which quantifies the amount of energy that is scattered and absorbed due to the excitation of dipolar LPP modes in the ellipsoid, has the same functional dependence as the observed absorption for the bow-tie nanoantenns in Fig.3.3(B) upon changing polarization angles. Furthermore, as long as the polarizabilities have different resonance frequencies according to the different dimensions of the three semi-axes of the ellipsoid, the extinction cross sections for a selected resonance frequency will show a strong polarization dependence. This situation changes only, if the polarizabilities are degenerated in their resonance frequencies or if the selected observation frequency is off-resonant. For the latter case the polarizabilities would be almost identical to that of the embedding dielectric material. The second scenario, i.e., a frequency degeneration of all three polarizabilities, is possible, e.g., for spherical nanoantennas for which the depolarization factors are equal $L_x = L_y = L_z = 1/3$. Consequently, the polarizabilities $\alpha_{x,y,z}(\omega)$ are equal. Similarly to the off-resonant case, the angular dependence with respect to the polarization angle will be described by a circular shape, as it is observed for the off-resonant excitation in Fig.3.3(B) (red-dashed line). Slight deviations from a perfectly circular line-shape are observed, since the observation frequency should be even smaller than applied here. Even though the above presented LPP model has been applied to describe the polarization dependence only, also the effect of angular incidence can be modelled with the respective transformation $\hat{U}$. These considerations and the resulting conclusions can be applied to understand the optical response of ensembles of nanoantennas as long as the ensemble properties are dominated by the single nanoantenna's properties.

As a summary of chapter 3.1, essential optical properties of dipole nanoantennas have been presented and explored. At first, the local electric field enhancement associated with the dipolar LPP resonance has been elaborated. Second, the excitation dependence for dipole nanoantennas, i.e., the electric dipole LPP mode, has been investigated, whereas special emphasis has been given to the polarization dependence. For the analytical modeling ellipsoidal nanoantennas have been selected, whereas for all numerical simulations a more complex

nanoantenna geometry, i.e., the bow-tie nanoantenna, has been considered. The reason for the investigation of the bow-tie nanoantennas is that it has been subject of interest in an internal collaboration with the Institute of Optics and Quantumelectronics at the Friedrich-Schiller-Universität. Finally, the bow-tie nanoantenna represents a timely and prototypical example, combining various physical concepts that can be conveyed to differing nanoantenna systems.

## 3.2 Combining localized dipole and propagating surface plasmon modes

In this chapter, particular optical dipole nanoantennas will be theoretically designed and experimentally investigated. These nanoantennas sustain local field enhancement and allow for a large area covering fabrication process. Furthermore, it will be presented how a particular arrangement of such nanoantennas can be beneficial in order to excite localized plasmon modes (LPP) as well as propagating plasmon modes (SPP). In the next part of this chapter, the physics of *Surface-Enhanced Raman Scattering* (SERS), as a potential application of the near-field enhancement, will be briefly presented. Finally, this chapter will be concluded by the application of these *doubly resonant* plasmonic samples for SERS. Thereby, the angular polarization dependence of the recorded SERS signals will be investigated, which together with the results from section 3.1.2, allows to characterize and illustrate the effect of the prepared nanoantennas.

### 3.2.1 Doubly resonant nanoantenna arrays

In this section it will be presented, how a particular type of dipole nanoantennas has been prepared for applications in the optical frequency domain. Therefore, the following requirements have to be fulfilled by a careful design of the nanoantennas:

- At first, the fabrication process should allow for a deterministic and large area covering with nanoantennas. For this purpose, high throughput electron beam lithography has been applied, utilizing illumination masks in form of one-dimensional line gratings. The entire process has been reported in detail in Refs. [HBS+08, PYM+10].

- Second, the resonance frequencies should match the optical or near-infrared domain. Moreover, nanoantennas operating in the electric dipole limit, as the fundamental LPP mode, are desired. This basically translates into size-limitations for the for nanoantennas.

- Third, the nanoantennas should possess the field enhancing mechanisms due to the lightning rod effect and the excitation of dipolar LPPs, reported in section 3.1.1, as well as due to SPP modes.

As a consequence of these conditions a *rhomb-shaped* nanoantenna geometry has been selected, which requires only a two step illumination process as indicated in Fig.3.4(A). By illuminating
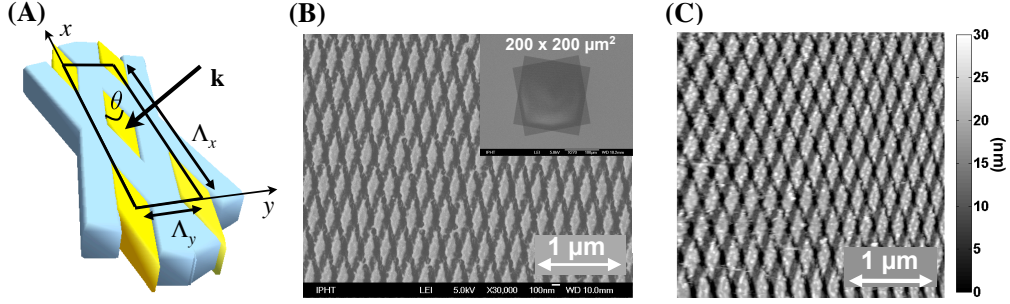
**Figure 3.4:** (A) Drawing of the principle fabrication scheme for rhomb-shaped nanoantennas, colored in yellow, utilizing two tilted line gratings (tilting angle $\theta$) which cause the removal of the blue-colored area. (B) SEM image of a particular nanoantenna array to visualize the reproducibility of the overall nanoantenna's shape and the homogeneous distribution obtained with the applied fabrication process. The inset shows a large area scan incorporating the two tilted structured areas. (C) AFM image of a nanoantenna array to visualize the homogeneity of the nanoantenna thickness, which has a value of 20 nm.

the photo-resist twice with a one-dimensional line grating it is possible to selectively remove the metal indicated by the two blue bars in Fig.3.4(A). The resulting geometry can be adjusted from rectangular ($\theta = 90°$) to rhomb-shaped nanoantennas ($0° < \theta < 90°$) by setting the angle between the two illuminating grating masks. The size of the nanoantennas is also dependent on the duty cycle of the applied illuminating line gratings. For triangular nanoantennas at least three fabrication steps utilizing these grating masks are required, while for the bow-tie nanoantennas an even more complicated scheme must be developed. The detailed fabrication process is described in [HBS+08]. Gold has been selected as the nanoantenna material, since it is more robust against surface oxidation than silver. Furthermore, Au has a higher compatibility with biological or chemical materials, which is essential since the nanoantenna arrays will be used as SERS substrates in the following section 3.2.3.

Thus, by this technique large arrays of gold nanoantennas can be realized. In Fig.3.4(B) images recorded by *scanning electron microscopy* (SEM) of a fabricated sample are shown. The realized tilting angle $\theta$ for the shown sample is 30°, yielding rhomb-shaped nanoantennas. In addition, a low magnification SEM image is shown in the inset of Fig.3.4(B), illustrating the two tilted illuminating masks. In Fig.3.4(C) a surface topography obtained with *atomic force microscopy* (AFM) is shown. The gray-scale color encodes the nanoantenna thickness. The average value for the thickness of the nanoantennas for this image is equal to the deposited metal film thickness of 20 nm and applies to all samples. The combination of the SEM and the AFM characterization is useful in order to check the samples for potential fabrication errors and to extract the exact geometrical values used for the theoretical calculations later on. With this step, the first requirement, i.e., a reliable, large area fabrication process, has been met.

To consider the second requirement, i.e., the presence of electric dipole LPP modes, optical far-field measurements, as described in section 2.2.1, as well as numerical simulations have been performed. Although a large number of samples has been prepared and optically characterized, only three selected samples covering all relevant properties will be discussed in the following. The dimensions of these nanoantenna arrays are listed in Tab.3.1. They have

| Parameter | Sample 1 | Sample 2 | Sample 3 |
|---|---|---|---|
| Period in $x$-direction $\Lambda_x$ (nm) | 437 | 800 | 1243 |
| Period in $z$-direction $\Lambda_y$ (nm) | 198 | 187 | 376 |
| Rhombus length $\Delta x$ (nm) | 279 | 514 | 810 |
| Rhombus width $\Delta y$ (nm) | 85 | 125 | 247 |
| Resonance frequency $x$-pol. $\nu$ (THz) | 256 | 164 | 171 |
| Resonance frequency $y$-pol. $\nu$ (THz) | 503 | 490; 417 | 464; 348 |

**Table 3.1:** Parameters of the three nanoantenna samples of interest obtained by structural (SEM) and optical characterization. Sample 1 corresponds to a regular array of rhombs, which can be realized by a 34° tilt of both illumination gratings. Sample 2 and 3 are characterized by roughly the same apex angle for the nanoantenna of (27° and 34°, respectively) but they are fabricated with an increased period of both crossed gratings. This translates into a larger period of the two-dimensional nanoantenna array as well as an expansion of the nanoantenna dimensions itself. The thickness of the Au layer is a final parameter that can be used to tailor the plasmonic properties of the samples. In all samples it was chosen to be 20 nm and verified by AFM measurements, see Fig.3.4(C).

been obtained by evaluating SEM images similar to Fig.3.4(B). After this structural characterization, spectrally resolved optical far-field measurements have been performed with the *Lambda 950* spectrometer, see section 2.2.1. Here, the polarization direction of the illuminating linearly polarized light has been set either along the short or the long axis of the rhombus. Results for the measured transmission spectra are shown in Fig.3.5(A-C). The arrows indicate the linear polarization direction with respect to the rhombus orientation. To verify the optical measurements, numerical simulations of the far-field spectra have been performed. Results for the corresponding FMM simulations, using the experimental parameters[5] of Tab.3.1, are presented in Fig.3.5(D-F). An overall agreement between the experimental and the numerical data can be observed for all three samples. In the following the nature of the observed resonances within the optical spectra will be considered in detail.

Starting with sample 1, having the smallest unit cell of the three selected ones, only two resonances can be observed [Fig.3.5(A,D)], denoted by (1) and (2). They are associated to the electric dipole-type LPP modes along the respective rhombus axis. They can be understood similar to the dipolar modes along the axes of an ellipsoid with three different semi-axes. The third mode, associated with the nanoantenna axis in propagation direction, i.e., $z$-direction, cannot be probed at normal incidence. This can be explained by regarding an ellipsoid with the LPP model, i.e., Eq.(3.13) and Eq.(3.14). For a propagation in $z$-direction and a polarization in the $xy$-plane only the dipole modes of the $x$- and the $y$-axis can be excited, if the ellipsoid is oriented with its major axis along the three coordinate axes. The dipole mode along the short axis occurs at higher frequencies, while the long-axis mode is located at lower frequencies, as expected from section 2.1.3.

For sample 2, an increasing size of the unit cell and of the rhombus dimensions [Tab.3.1] results in a red-shift of the two resonances (1) and (2), as expected. However, the shift for resonance (1) is comparably larger than the shift of resonance (2). This is due to the relative

---

[5]For the $SiO_2$ substrate a constant bulk permittivity of $\epsilon = (1.46)^2$ has been applied. The permittivity of gold has been taken from literature [JC72].
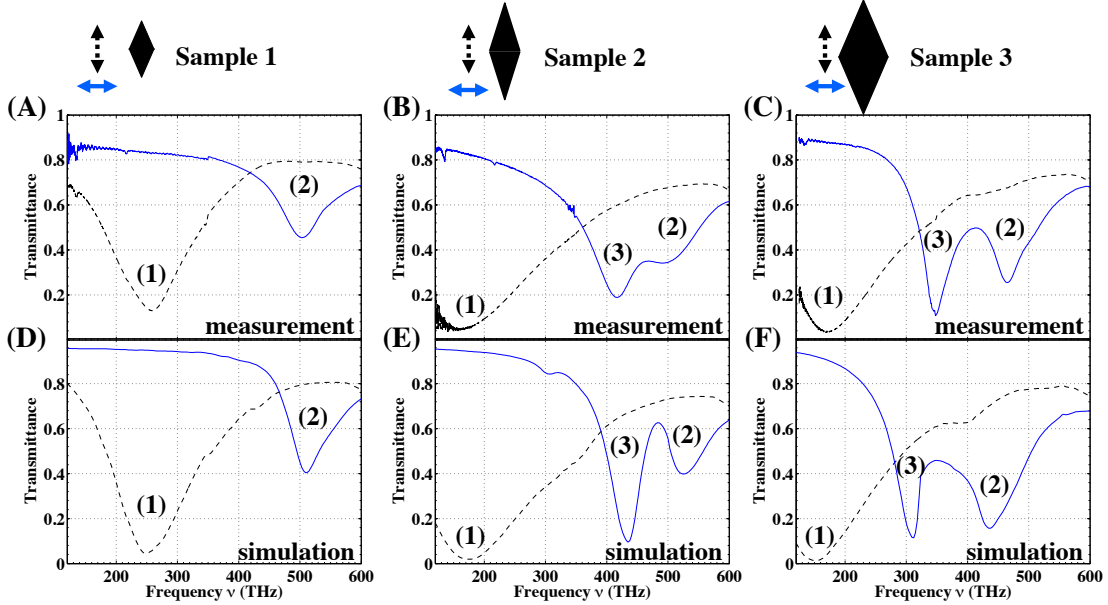
**Figure 3.5:** Results of the experimental measurements of the transmission spectra for (A) sample 1, (B) sample 2, and (C) sample 3. Resonances (1) and (2) are associated with the electric dipole LPP mode along the respective rhombus axis, while mode (3), approaching only for larger lattice periods corresponds to a SPP mode. (D),(E),(F) the respective numerical results obtained by FMM simulations including the experimental parameters of Tab.3.1.

change in size of the semi-axes being much larger for the long than for the short rhombus axis. In addition, to the two resonances (1) and (2) a third resonance (3) occurs, which corresponds to a SPP mode induced by the grating period, as will be shown later.

Finally, sample 3 with an even further increased period and rhombus size adds no new resonances, only the SPP resonance (3) and the LPP resonance (2) are now clearly separated.

In the following, the LPP and SPP origin of the resonances will be investigated by probing for essential properties of the respective plasmonic mode of sample 2. These will finally allow to verify the LPP or the SPP character of the respective resonances.

At first, a simplified LPP model is derived, taking both electric dipole modes into account with respect to the $x$- and $y$-direction. The molecular dipole moment of a single rhomb-shaped nanoantenna can be calculated with [Eq.(2.28)]

$$p_j = q_j r_j, \qquad j \in [x, y]. \tag{3.15}$$

To account for the carrier dynamics $\mathbf{r}$ induced by the microscopic electric field $\mathfrak{E}$, a simple oscillator model may be applied

$$\frac{\partial^2}{\partial t^2} r_j - \gamma_j \frac{\partial}{\partial t} r_j + \omega_{0j} r_j = \frac{q_j}{m_j} \mathfrak{E}_j. \tag{3.16}$$

The damping, due to non-radiative, i.e., dissipative, and radiative losses is described by the damping constant $\gamma_j$. A resonant excitation of the carriers is assumed at frequencies $\omega_{0j}$. The solution of Eq.(3.16) can be easily obtained by temporal Fourier transformation (2.51).

52
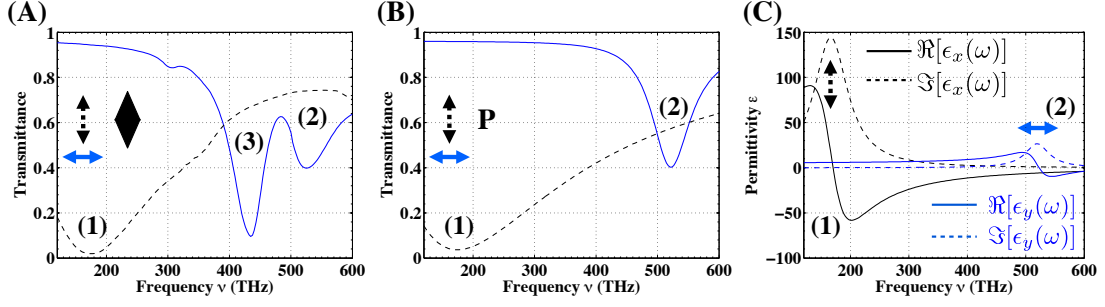
**Figure 3.6:** Transmission spectra for sample 2 obtained by (A) numerical FMM simulations, and (B) by the fitted LPP model according to Eq.(3.15) for the two polarization directions of interest, denoted by the arrows. As can be seen, the two resonances (1) and (2) can be reproduced nicely. (C) The effective permittivities for both polarization directions that are applied to calculate the spectra of the effective medium slab shown in (B).

Averaging of an ensemble of nanoantennas, described by Eq.(3.15) and Eq.(3.16) yields the macroscopic polarization

$$P_j(\omega) = \eta p_j(\omega) = \frac{q_j}{m_j \epsilon_0} \frac{1}{\omega_{0j}^2 - \omega^2 - i\omega\gamma_j} E_j(\omega), \qquad (3.17)$$

which finally can be used to calculate the associated effective permittivity, see Eq.(2.53,2.55),

$$\epsilon_j(\omega) = 1 + \frac{\Omega_j^2}{\omega_{0j}^2 - \omega^2 - i\omega\gamma_j}, \qquad \Omega_j^2 \equiv \frac{\eta q_j}{m_j \epsilon_0}. \qquad (3.18)$$

The effective permittivity possesses Lorenz-type resonances exactly at the resonance positions of the LPP excitations. This functional shape is consistent with the previous results of LPP resonances of the ellipsoids in section 2.1.3. The LPP model for ellipsoids cannot be applied for the present rhomb-shaped nanoantennas, because the quasi-static description fails due to retardation effects. Retardation and increased radiation damping become important due to the increased nanoantennas dimensions, which exceed the limitations for a static description [BCM83].

However, with the introduced dipole model it is possible to describe an ensemble of electric dipoles by the associated effective permittivity. With Eq.(3.18) it is possible to calculate the associated spectra for the two resonances for the respective polarization direction. An analytical transfer matrix formalism for a slab with the thickness of 20 nm can be applied [BW99] to calculate the far-field spectra. By adjusting the parameters $\omega_{0j}$, $\Omega_j$, and $\gamma_j$ it is possible to reproduce the numerical spectra[6] of sample 2. Both spectra, i.e., the numerical as well as the spectra fitted with this simple model, are shown in Fig.3.6(A,B). The final effective permittivities for both polarization directions are shown in Fig.3.6(C). Consequently, resonance (3) is absent in all spectral quantities, shown in Fig.3.6, as it is not yet included in the model.

---

[6]The found parameters are $\omega_{0x} = 170$ THz, $\omega_{0y} = 520$ THz, $\gamma_x = 70$ THz, $\gamma_x = 50$ THz, $\Omega_x = 1.7 \cdot 10^6$ (THz)$^2$, $\Omega_y = 1.6 \cdot 10^5$ (THz)$^2$.

Now, the transverse wavevector provided by the lattice of the nanoantennas will be considered. This will provide the required tangential momentum to launch SPP excitations at the interface between the dielectric ambient and the effective medium surface described by Eq.(3.18). The applied method is known as the *empty lattice approximation* [TPdA$^{+}$06]. Therefore, the lattice is considered as a perturbation that just provides additional transverse grating vectors, while the structured medium is described by its effective permittivity. The transverse wavevector induced by the grating can be calculated by the grating equations (2.127) and (2.128). The wavevector of a single interface SPP can be calculated by Eq.(2.110). Combining these two contributions together with the projection of the incident wavevector for oblique incidence yields the simple condition[7]

$$\frac{\omega^2}{c^2}\sqrt{\epsilon_{\mathrm{a}}(\omega)}\sin(\theta_{\mathrm{inc},j}) + \frac{2\pi m_j}{\Lambda_j} = \frac{\omega^2}{c^2}\sqrt{\frac{\epsilon_j(\omega)\epsilon_{\mathrm{a}}(\omega)}{\epsilon_j(\omega)+\epsilon_{\mathrm{a}}(\omega)}}, \qquad (3.19)$$

which is the *conservation of momentum*. Obviously Eq.(3.19) is dependent on the angle of incidence $\theta_{\mathrm{inc},j}$ and the grating period $\Lambda_j$ for the respective direction $j \in [x, y]$. Hence, there are two possibilities to prove the SPP nature of resonance (3). First, by changing the lattice period for normal incidence Eq.(3.19) simplifies, since $\sin(\theta_{\mathrm{inc},j}) = 0$. For that particular case the resonance positions, i.e., the frequencies for which Eq.(3.19) is fulfilled, are only dependent on the grating periods $\Lambda_j$. As it has been discussed in section 2.1.4, guided solutions for SPP modes can only be obtained if at least one permittivity of the two adjacent materials $\epsilon_{\mathrm{a}}(\omega)$ and $\epsilon_j(\omega)$ is negative. Hence, SPP mode propagation is expected to occur only in $x$-direction, because only the real part of $\epsilon_x(\omega)$ is negative for resonance position (3), see Fig.3.6(C). To check this dependence, the grating vector $2\pi/\Lambda_x$ has been varied in numerical FMM simulations with all other parameters fixed for sample 2. The frequency of resonance (3) has been evaluated in dependence of the grating vector in $x$-direction together with the expected dependence from Eq.(3.19). Results are shown in Fig.3.7(A). The numerically obtained resonance positions agree well with the analytically predicted ones for $m_x = 2$. Deviations appear for frequencies above $\approx 450$ THz. This is due to the fact that the simple oscillator model [Eqs.(3.15-3.18)] describes the transmission only up to this frequency. For higher frequencies the numerically calculated transmission [Fig.3.6(A)] is higher than the modelled one [Fig.3.6(B)].

Second, an additional transverse wavevector induced by oblique incidence influences resonance frequency (3), see Eq.(3.19). In turn, resonance frequencies (1) and (2) should appear unaffected, except for a change in the resonance strengths, as previously discussed for LPP modes. As for the grating vector manipulation before, the impinging electric fields are polarized along the $y$-axis. The angle of incidence has been changed in both transverse directions, i.e., in the $yz$-plane [Fig.3.7(D)], and the $xz$-plane [Fig.3.7(E)]. While the resonance positions

---

[7]For completeness, the right hand side of Eq.(3.19) should contain the transverse wavevector contributions associated with the diffracted orders, see Eq.(2.127) and Eq.(2.128). For the considered samples it has been proven numerically that the intensities in higher diffraction orders are vanishing. Hence, their transverse momentum can be safely neglected in Eq.(3.19).
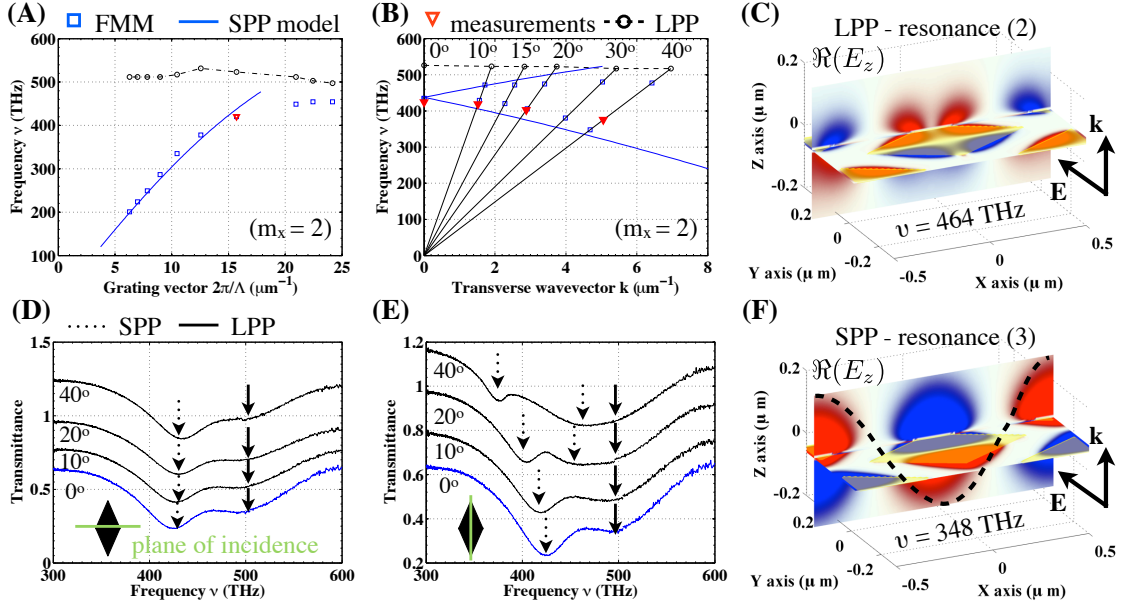
**Figure 3.7:** (A) Results for the grating vector variation according to Eq.(3.19). The resonance frequencies are described by the SPP model assuming $m_x = 2$. (B) The corresponding resonance frequency splitting which is observed for an additional transverse wavevector, provided by oblique incidence. For both variations, i.e., (A) and (B) sample 2 has been selected. The measured spectra for oblique incidence with a tilt in the (D) $yz$- and (E) $xz$-plane for sample 2. The simulated near-field distributions for $E_z$ for $y$-polarization of sample 3 at (C) the LPP resonance frequency (2), and (F) the SPP frequency (3).

for a tilt in the $yz$-plane should be unaffected, a splitting of resonance (3) is expected for a tilt in the $zx$-plane. The reason for this is the additional transverse wavevector which can be either parallel or anti-parallel to the grating vector $\pm 2m_x\pi/\Lambda_x$ yielding two solutions for Eq.(3.19). Hence, for oblique incidence a splitting of resonance (3) into two resonances is expected to occur. Since, the manipulation of the angle of incidence does not require the fabrication of new samples, as for instance the grating vector manipulation would do, the dependence has been investigated experimentally as well. For this purpose sample 2 has been selected. Results for the measured transmission spectra for tilted incidence are shown in Fig.3.7(D,E). As discussed above, a splitting of resonance (3) can be observed for a tilt in the $xz$-plane. To compare these results with the numerical and the analytical simulations according to Eq.(3.19), the resonance positions have been plotted dependent on the transverse wavevector in Fig.3.7(B). Again the grating vector order has been set to $m_x = 2$ as has been found in the grating vector variation before[8]. Comparing the experimental values with the numerical values obtained from FMM simulations as well as predictions from Eq.(3.19), it can be seen that the resonance splitting can be explained well with the SPP model. Deviations of the predicted resonance frequencies by the SPP model can be observed for frequencies above $\approx 450$ THz. Again, these deviations can be explained with the effective permittivity $\epsilon_x(\omega)$, which is only valid for lower frequencies.

To conclude this section, the field distributions for each resonance (2) and (3) will be shown. This also provides the necessary condition for the SPP excitation, while Eq.(3.19) can be

---

[8]For the first order, i.e., $m_x = 1$, the associated grating vector is still to small to match the required $k$ of the SPP.

considered as a required condition for the existence. In order to observe SPP excitations in the spectra the field overlap between the SPP mode and the fields at the effective medium interface must be non-zero, additionally. Therefore, sample (3) has been selected, since for this sample both resonances are clearly separated, which allows an almost undisturbed observation of both different field distributions. For simplicity, normal incidence has been assumed. Considering the field distributions for $E_z$ for resonance (2), the field distribution of an electric dipole, directed in $y$-direction can be observed in the $z$-cut of Fig.3.7(C). In addition to the electric dipole response, a standing wave pattern can be observed for resonance (3) in the $y$-cut, see Fig.3.7(F). It is important to note that the shown $y$-cuts have been recorded not in the center at $y = 0$, but at the position $y = \Lambda_y/4$. In the center the electric field component of an electric dipole is vanishing, see Fig.2.3 in section 2.1.2. Hence, the field component normal to the surface which is required to excite SPP's is only available off the center. Furthermore, this can be used to explain the splitting of the SPP resonance for oblique incidence. For normal incidence two SPP modes are launched in opposite directions which are degenerated with respect to their resonance frequencies. One SPP mode in the half-space $y > 0$ and the other SPP mode in the half-space $y < 0$. Their degeneracy will be lifted for oblique incidence as shown in Fig.3.7(B). Finally, it can be seen that the launched mode corresponds to the fundamental SPP mode, since one plasmon wavelength fits in the entire unit cell in $x$-direction, indicated by the black-dashed line in Fig.3.7(F).

Thus, the numerical near-field calculations together with the variations of the grating vector and the illumination clearly reveal the SPP character of resonance (3). Hence, with all performed investigations from this section the observed resonance (3) will be considered as a surface plasmon polariton that is excited at a effective medium interface. Such an SPP mode, propagating on periodically corrugated surfaces, has been investigated at first on flat interfaces with periodically arranged holes and coined the term *spoof plasmon mode* [PMMGV04, HES05, GVMMP05, WAM+08]. Recently, such SPP modes have been observed in various other geometries, e.g., periodically corrugated channels [FDMMMGV09, NMCFD+10] or wedges [FDMMM09], and tapered tips [MAMMGV06]. Later on, these samples are of special interest for application to SERS. Before this will be performed, a brief recapitulation of some basic properties of the SERS effect will be given in the following section 3.2.2.

## 3.2.2 Surface-Enhanced Raman Scattering

In this section the principles of the SERS effect will be repeated. Due to the huge number of different theories [KMK06] it is almost impossible to give a detailed explanation within a few pages. A comprehensive review about SERS theories has been presented by *M. Moskovits* in 1985 [Mos85]. The following explanation will be as compact as possible in order to understand how near-field enhancing nanoantennas improve the efficiency of the Raman scattering.

In general, SERS describes increase of magnitude of the Raman signals emitted by molecules in the vicinity of metal electrodes, rough surfaces or metal nanostructures. Among other contributions to this effect, there are two substantial mechanisms that a are considered as
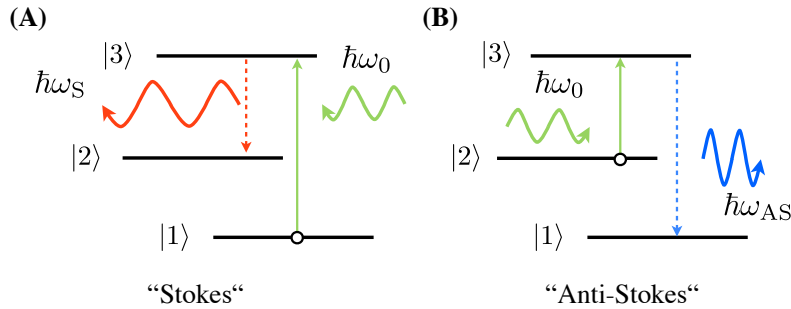
**Figure 3.8:** Simplified presentation of the frequency shift that is characteristic for Raman scattering. The re-emitted photon can have (A) a lower (Stokes-shift), or (B) a higher energy (Anti-Stokes-shift) compared with the incident photon energy.

the dominant ones, i.e., the *chemical* and the *electromagnetic enhancement*. The first can be considered as a chemical modification on the Raman tensor of the molecule when adsorbed to a metal surface [LBLX86, CK98]. This effect can improve the Raman signals by approximately a factor of 10 [Mos85]. The second contribution, i.e., the electromagnetic enhancement, has been shown to provide enhancement factors that can exceed the chemical enhancement by orders of magnitude [KMK06]. Hence, the electromagnetic enhancement will be solely discussed in this work.

A simplified scheme of the Raman scattering process is illustrated in Fig.3.8. Incident radiation induces the transition between the molecular vibrational states of a particular molecule. If the photon energy $\hbar\omega_0$ matches the energy for such a transition the respective vibrational state will be excited. This state can relax into one with a higher or lower energy level as compared with the initial state. The radiated photon associated with this transition will then have a lower (*Stokes shift*) or a higher energy (*Anti-Stokes shift*) compared to the incident photon energy, see Fig.3.8(A,B), respectively. The transitions between the molecular vibrational states in an external electromagnetic field with the frequency $\omega_0$ can be considered as dipole transitions with a classically introduced molecular electric dipole moment[9]

$$p_{\mathrm{m},l}(\mathbf{r}, \omega_{\mathrm{R}}) = \alpha_{\mathrm{m}}(\omega_0, \omega_{\mathrm{R}}) E_l(\mathbf{r}, \omega_0). \tag{3.20}$$

Equation (3.20) states that an electric field with the frequency $\omega_0$ will induce an electric dipole moment at the Raman-shifted (Stokes or Anti-Stokes) frequency $\omega_{\mathrm{R}}$. Moreover, Eq.(3.20) represents a classical approximation neglecting the tensorial character of the molecular polarizability, while the exact process requires a full-vectorial, quantum-mechanical treatment, including perturbation theory. Nevertheless, this simplified approach has been established and is frequently applied to phenomenologically explain the SERS effect by classical means [KMK06, LBC+81]. If the molecule is adsorbed on the surface of a metal nanoantenna, e.g., an ellipsoidal particle, the incident field $\mathbf{E}(\mathbf{r}, \omega_0)$ has to be replaced by the enhanced near-field of the nanoantenna. The induced molecular dipole moment of the adsorbed molecule may

---

[9] A physically thorough and classical examination of the SERS effect including ellipsoidal-shaped metal nanoantennas has been performed by *Gersten* and *Nitzian* [GN80, GN81].

then be written as [LBC⁺81]

$$p_{\mathrm{m},l}(\mathbf{r},\omega_R) = \frac{2}{\epsilon_{\mathrm{a}}(\omega)r^3}\alpha_{\mathrm{m}}(\omega_0,\omega_{\mathrm{R}})\alpha_l(\omega_0)E_l(\mathbf{r},\omega_0). \tag{3.21}$$

In Eq.(3.21) $\alpha_l(\omega_0)$ is the component of the ellipsoid's polarizability, while $r$ is the distance from the center of the ellipsoid to the molecule. This molecular dipole moment $\mathbf{p}_{\mathrm{m}}(\mathbf{r},\omega_{\mathrm{R}})$ oscillating at the Raman-shifted frequency $\omega_{\mathrm{R}}$ induces a dipole moment in the ellipsoid $\mathbf{p}_{\mathrm{e}}(\mathbf{r},\omega_{\mathrm{R}})$ at the Raman-shifted frequency as well

$$\begin{aligned} p_{\mathrm{e},l}(\mathbf{r},\omega_R) &= \frac{2}{\epsilon_{\mathrm{a}}(\omega)r^3}\alpha_l(\omega_{\mathrm{R}})p_{\mathrm{m},l}(\mathbf{r},\omega_{\mathrm{R}}) \\ &= \frac{4}{\epsilon_{\mathrm{a}}^2(\omega)r^6}\alpha_l(\omega_{\mathrm{R}})\alpha_l(\omega_0)\alpha_{\mathrm{m}}(\omega_0,\omega_{\mathrm{R}})E_l(\mathbf{r},\omega_0). \end{aligned} \tag{3.22}$$

The ratio between the dipole moments with [Eq.(3.22)] and without the presence of the nanoantenna [Eq.(3.20)] is defined as the enhancement factor $g$

$$g \equiv \frac{p_{\mathrm{e},l}(\mathbf{r},\omega_R)}{p_{\mathrm{m},l}(\mathbf{r},\omega_R)} \propto \frac{1}{r^6}\alpha_l(\omega_0)\alpha_l(\omega_{\mathrm{R}}). \tag{3.23}$$

Since in SERS measurements the intensity is recorded, its enhancement factor is defined as

$$\Gamma \equiv |g|^2 \propto \left|\frac{1}{r^6}\alpha_l(\omega_0)\alpha_l(\omega_R)\right|^2. \tag{3.24}$$

Having arrived at the final equation (3.24), some important aspects of the SERS mechanism can be explained. As intuitively expected, the enhancement is largest, if the molecule is located directly at the surface of the nanoantenna due to the $1/r^6$ dependence of $\Gamma$. Since the polarizability is directly proportional to the local electric field for a fixed position, see, e.g., Eq.(3.6,2.98,2.99), the enhancement factor $g$ is proportional to $E(\omega_0)E(\omega_{\mathrm{R}})$. Furthermore, if the Raman-shifted frequency $\omega_{\mathrm{R}}$ is close to the incident frequency $\omega_0$, the intensity enhancement can be approximated as $\Gamma \propto |E(\omega_0)E(\omega_{\mathrm{r}})|^2 \approx |E(\omega_0)|^4$. This fourth power dependence is a frequently applied argument to explain the dramatical SERS enhancement factors $\Gamma > 10^6$ that have been reported for single molecules at resonant metal nanoantennas [FSD08][10]. In the previous section 3.1.1 it has been shown that the polarizabilities of nanoantennas $\alpha(\omega)$ show a resonant behavior that coincides with a strong near-field enhancement. This local field enhancement is induced by the excitation of LPP resonances of the nanoantennas. Hence, nanoantennas supporting a local field enhancement are preferable to observe improved SERS signals. Moreover, Eq.(3.24) highlights that efficient SERS signals can be achieved if the electric near-fields at both frequencies, the excitation $\omega_0$ as well as the emission frequency $\omega_{\mathrm{R}}$ are enhanced. Thus, the frequency range for typical SERS samples is limited by the linewidth of the excited LPP resonance. By increasing this linewidth of the LPP resonance the near-

---

[10]It has been shown by *Stockman* and others that for particular aggregates the intensity is dependent on the third power rather than on the fourth [Sto97, GAB⁺99].

field enhancement decreases yielding weaker SERS signals. In the forthcoming section a new type of samples will be introduced, circumventing this limitation by exploiting two tunable plasmonic resonances as presented in section 3.2.1.

From the beginning of the SERS effect, which has been discovered by *Fleischmann et al.* in 1974 [FHM74] on rough silver electrodes, more and more sophisticated nanoantenna approaches have been developed to continuously improve the enhancement factors. Present nanoantennas have been shown to enable even single molecule detection [NE97]. It is also worth noting that the Raman spectra contains unique features that are characteristic for the particular analyte. A recorded SERS spectra can be used to unambiguously prove the presence of particular substances in a very small volume. Exactly this property makes SERS attractive as a highly sensitive bio-chemical sensing approach.

### 3.2.3 Application of doubly resonant nanoantenna arrays to Surface-Enhanced Raman Scattering

In this section the samples, which simultaneously exhibit LPP and SPP resonances, will be used for SERS measurements[11]. Due to the fabrication process yielding reproducible nanoantenna arrays with a high surface density of near-field enhancing elements the samples will be applied for surface-averaged SERS measurements. For this purpose, sample 2 has been selected as a substrate, while *crystal-violet* as a standard adsorbate for SERS detection has been applied. To illustrate the improvements that can be achieved with a doubly resonant substrate, sample 1 will be applied as a reference. In contrast to sample 2, sample 1 shows only a LPP mode at the same frequency as sample 2. On the basis of the optical properties of sample 2, an enhanced SERS efficiency is expected, due to the presence of two near-field enhancing plasmonic modes. These are associated with the LPP mode of the rhombus and the SPP mode induced by the lattice. It is important to point out that the SPP mode rather than the LPP mode, is typically non-radiating in the same manner as it cannot be excited by normally incident plane waves. As has been shown in section 2.1.4, SPPs are confined at a metal-dielectric interface. But since the interface comprises an additional grating vector, this mode can be excited and thus becomes radiative. This is important for the SERS process since this guarantees that if the emission frequency approaches the SPP resonance, the SERS molecules require a radiative mode to couple. Otherwise, the enhanced SERS signals would be confined to the surface until their energy will be dissipated into heat.

Since with the fabrication process, described in section 3.2.1, large areas can be covered with nanoantennas, the resulting substrates are suitable for *averaged* SERS measurements. Compared to the measurement at isolated nanoantennas, the recorded surface-averaged SERS enhancements are typically several orders of magnitude lower. This is caused by areas of the substrates that possess no near-field enhancement or that the are not homogeneously covered with the adsorbed analyte. Hence, they are not contributing to the detected SERS intensity.

---

[11]Measurements have been performed by *Dana Cialla* in collaboration with the Institute of Photonic Technology Jena as well as the Institute of Physical Chemistry at the Friedrich-Schiller-Universität Jena.
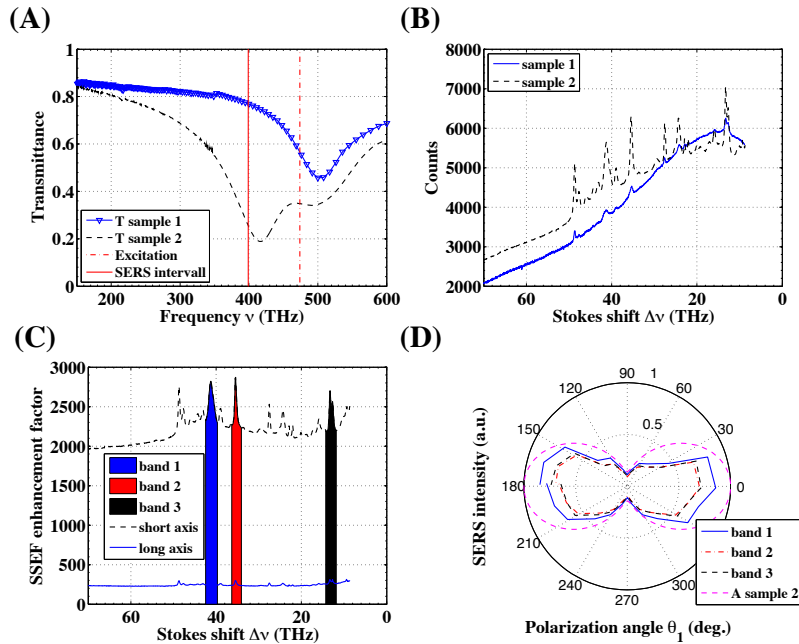
**Figure 3.9:** The transmission spectra indicating the LPP (1) and the SPP resonances (3) for sample 1 and 2. Additionally, the SERS interval is sketched starting with excitation frequency marked by the dashed-dotted line until the solid line. Hence, both resonances are included in the investigated frequency interval. (B) Comparision between the measured SERS spectra of sample 1 (blue solid line) and 2 (black dotted line). (C) The calculated SERS surface enhancement factor (SSEF) for sample 2 for a polarization along the short rhombus axis (black dotted line) exhibiting for LPP and SPP modes. As a reference, the SSEF for the long axis for which no plasmonic resonance is within the measured SERS interval is shown (blue solid line). (D) Angular dependence of the SERS signal for three selected bands, as indicated in (C) together with the calculated absorption of sample 2 (normalized units).

In turn, the averaged measurements have the important advantage that the required setup is comparably simple and fast in contrast to the measurements at isolated nanoantennas.

Results for the recorded SERS intensities for sample 1 and sample 2 are shown in Fig.3.9. In Fig.3.9(A) the measured transmission spectra for sample 1 and 2 are presented again to show that both samples have their LPP resonance (2) at around 500 THz. In addition, the excitation frequency has been indicated by the dashed-dotted line. This line corresponds to the emission wavelength of a He-Ne laser ($\lambda = 633$ nm). Starting from the associated frequency the scattered SERS signals are recorded at decreasing, i.e., Stokes-shifted, frequencies overlapping with the SPP resonance (3) at $\nu = 417$ THz. Results are shown in Fig.3.9(B)[12]. As can be clearly seen, the peaks, i.e., the scattered SERS features[13], are much more pronounced and sharp for sample 2 when compared to sample 1. Especially for larger Stokes-shifts the quality of the SERS signal for sample 2 remains quite sharp and clearly exceeds the signal of sample 1. This can be attributed to the presence of the SPP resonance (3) which appears at a Stokes-shift of $\Delta\nu > 20$ THz. In order to quantitatively investigate the SERS effect, the

---

[12]Typically, the Raman signals for the Stokes-shift are presented by inverting the frequency axis, while for the Anti-stokes case the frequency axis is not inverted.

[13]The peaks in the SERS spectra of Fig.3.9(B) are typically accompanied by a characteristic background continuum whose physical origin is still discussed [MCS+10].

*SERS surface enhancement factor* (SSEF) has been calculated [RBME07]

$$\Gamma_{\text{SSEF}}(\omega) = \frac{I_{\text{SERS}}(\omega) C_{\text{RS}} H_{\text{eff}}}{I_{\text{RS}}(\omega) \mu_{\text{M}} \mu_{\text{S}} A_{\text{M}}}. \tag{3.25}$$

In Eq.(3.25) $I_{\text{SERS}}(\omega)$ is the recorded SERS intensity, $I_{\text{RS}}(\omega)$ is the recorded Raman intensity measured without the nanoantennas. The remaining parameters characterize the crystal violet solution and the nanoantenna array. $C_{\text{RS}} = 6.02 \cdot 10^{24}$ m$^{-3}$ is the concentration of crystal-violet for the measurement of the Raman scattering without the nanoantenna sample, $\mu_{\text{S}} = 1.7 \cdot 10^{18}$ m$^{-2}$ and $\mu_{\text{M}} = 2/(\Lambda_x \Lambda_z) = 1.34 \cdot 10^{13}$ m$^{-2}$ are the average densities of the molecules on the nanoantenna array and of the nanostructures per unit area, respectively.

Considering the calculated SSEF in Fig.3.9(C) for sample 2, a value for the averaged enhancement of $\geq 2000$ can be obtained. As a reference the polarization has been changed along the major axis of the rhombus ($x$-direction), where the averaged enhancement decreases to $\approx 200$. This control experiment is a very reliable proof that the produced sample 2 enhances the SERS signal significantly for the polarization direction parallel to the minor axis ($y$-axis). The reason for this is that only the polarization direction of the illumination has been turned, while all other parameters remained fixed. Typically, the number of adsorbed molecules, the structure quality, etc., are differing from sample to sample. With the possibility to tilt the polarization direction the plasmonic resonances of the prepared samples can be easily switched on and off. Moreover, one observes that the SSEF is larger than unity even for a polarization direction along the major axis of the nanoantennas. In the SERS measurement interval, shown in Fig.3.9(A), no resonance will be excited. The only mechanism that still provides a near-field enhancement in this off-resonant case is the lightning-rod effect attributed to the sharp-edged geometry, see section 3.1.1. This effect is of course weaker in amplitude when compared with the field enhancement associated with LPP excitation, but still able to induce an enhanced SERS signal.

Finally, the polarization dependence of the SERS signals of sample 2 has been measured for three characteristic SERS bands, as indicated by the bars in Fig.3.9(C). The observed dependence shows a maximum for a polarization along the minor axis ($\theta = 0°$), while the SERS intensity is lowest for a polarization direction along the minor axis of the nanoantennas ($\theta = 90°$). The overall shape of this dependence is very similar the the characteristic behavior for the extinction cross sections for dipole nanoantennas, shown in Fig.3.1(B). Thus, the measured SERS intensity follows the excitation strength of the nanoantenna sample, as represented by the calculated absorption for sample 2 upon changing the incident polarization angle, see the magenta-colored line in Fig.3.9(D). Hence, the polarization resolved SERS signals can be used to indirectly visualize the plasmonic nature of the underlying dipole nanoantenna samples.

In summary of part 3, the main physical concepts of optical nanoantennas operating in the electric dipole regime have been presented. As one of the most important properties, the local field enhancement has been discussed. In a next step, specially designed nanoantenna arrangements have been shown to support SPP mode propagation, additionally. Thereby, the

planar arrangement of the nanoantennas has been described by an effective permittivity, while its lattice has been considered by an additional transverse grating vector. As an application, SERS measurements on such samples have been performed, which led to an improved SERS signal when compared to samples supporting LPP modes only. These samples have been investigated in a collaboration with the Institute of Photonic Technology as well as the Institute of Physical Chemistry of the Friedrich-Schiller-Universität. Besides the results shown here [PYM+10], the presented nanoantennas have been applied in for various SERS experiments [CSH+09, CPH+10].

In the next part, metamolecules operating in higher multipole regimes will be investigated. Thereby, similar to the description of the nanoantenna arrangements in this part, ensembles of structures will be considered and described by their effective material parameters.

# 4 Higher-order multipole properties of optical metamaterials

## 4.1 Linear optical properties

In part 4 particular metamolecules possessing a higher-order multipolar response will be presented. Additionally to the electric dipole modes, as they have been subject of part 3, now both multipolar excitations of second order, i.e., the electric quadrupole and the magnetic dipole moments, will be considered. For ordinary matter the appearance of higher-order multipoles is caused by a more complex atomic assembly of molecular carriers, e.g., as for the carbon dioxide molecule [BD63]. Consequently, the geometry of the required metamolecules possessing higher multipolar contributions is expected be more complex, as well. Thus, particularly coupled and more complex-shaped geometries are investigated in the following as compared to the electric dipole nanoantennas of the previous part 3.

The most interesting application of metamaterials obeying higher-order multipolar responses is the possibility to alter the wave propagation in the metamaterial by structural modifications on the individual metamolecules. A major difference between metamaterials and natural materials is the possibility to include magnetic effects at optical frequencies. As it has been derived in section 2.1.1, this can be achieved by the excitation of magnetic dipole moments, induced by particularly designed mesoscopic currents. This results in a dispersion in the magnetization which is typically absent for optical frequencies in any natural material [LL85].

Hence, this part will focus on how dispersive properties of metamaterials can be influenced by taking into account second order multipole moments. In chapter 4.1 emphasis is put on the linear optical properties, while in chapter 4.2 nonlinear optical properties, induced by second-order multipolar contributions, will be discussed. Since both of these effects will be investigated on the basis of averaged metamaterials, the final chapter 4.3 will conclude by revealing the multipole moments of isolated and thus microscopic metamolecules. It will be presented how this can be performed by a rigorous decomposition of the scattered field into multipolar contributions.

### 4.1.1 Cut-Wire metamolecule

In the first section 4.1.1 a particular metamolecule, i.e., the cut-wire pairs (CW) [SZO01, SCC⁺05, DEW⁺05, CME⁺08], will be considered. It is selected since it is one of the simplest metamolecules, possessing a second-order multipolar response. The CW metamolecule conceptually consists of two sub-wavelength metal wires that are closely spaced. Each of the wires is acting like an electric dipole-type nanoantenna. Upon external illumination the narrow spacing provides a coupling due to the overlap of the near-fields of both nanoantennas [CME⁺08]. Hence, a splitting of the two isolated dipole modes into two energetically separated modes can
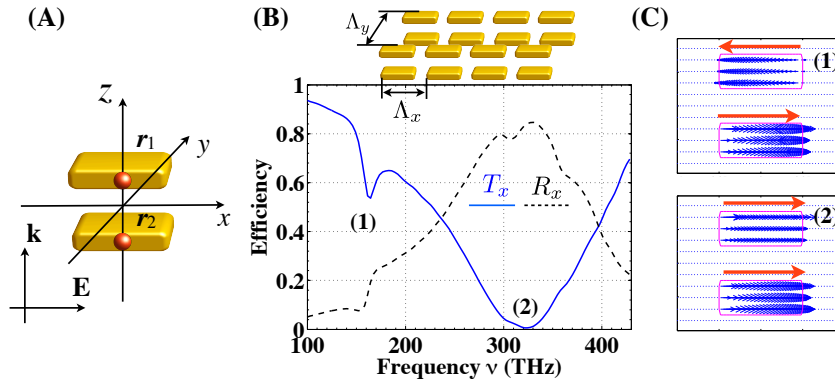
**Figure 4.1:** (A) Sketch of the CW metamolecule with the charge carriers representing the dynamics denoted by red dots. Each of the dots accounts for two carriers. A positively and a negatively charged one being at the same position when there is no an external electric field. (B) The numerically obtained far-field reflectance (dashed) and transmittance (solid) for a periodic arrangement of CW pairs. The spectra have been calculated for plane wave propagation in $z$-direction presuming $x$-polarized electric fields. The numbers denote the two fundamental resonances: (1) anti-symmetric and (2) symmetric resonance. (C) Top: Electric field ($E_x$) inside the CW pairs for resonance (1). Bottom: Electric field for resonance (2).

be observed. Thereby, the two electric dipole moments are oriented either in-line (*symmetric mode*) or opposite (*anti-symmetric mode*) to each other. The anti-symmetric mode is responsible for the second-order multipole response, whereas the symmetric mode contributes solely to the electric dipole response.

This can be easily illustrated by the multipole series. Considering an isolated electric dipole nanoantenna, the total charge, being the sum over all positively and negatively charged carriers, vanishes for neutrally charged nanoantennas. Thus, the next order in the expansion series has to be considered, i.e., the electric dipole moment. For the isolated dipole nanoantenna[1] the electric dipole response suffices to understand the optical interaction, see part 3. Now, considering a metamolecule that is created by two near-field coupled electric dipole-type nanoantennas, the total charge is vanishing as well. If the symmetric mode is excited, the response of the metamolecule is dictated by the lowest-order multipole moment. For this particular mode it is just the constructive superposition of two electric dipoles. For the anti-symmetric mode the two oppositely directed dipoles annihilate and the next order of the multipole expansion becomes important, i.e., the magnetic dipole and the electric quadrupole moments[2].

Similar to section 3.2.2, where the electromagnetic response of an isolated nanoantenna has been transformed into multipolar contributions, the same procedure will be performed for the CW metamolecule. The remaining missing part for this task is the access to the bound carrier dynamics in the CW metamolecule $\mathbf{r}_{b(m)}$, see section 2.1.1. With an underlying understanding of these carrier motions all multipole contributions of interest [Eqs.(2.28,2.29,2.45)] as well

---

[1]Note that this holds for nanoantennas with sub-wavelength dimensions, only. In particular, for extended nanoantenna wires exceeding this limitation, the nanoantenna will expose standing surface modes that can no longer be described by electric dipole excitations [Nov06, DVK+10].

[2]In section 2.1.2 it has been derived that both modes, the electric quadrupole and the magnetic dipole moment, are of equivalent order and thus have to be simultaneously considered for consistency.

as the dispersion relation and the material responses according to Eqs.(2.55,2.56) will be obtained.

In Fig.4.1(A) the CW metamolecule is sketched. The red dots in Fig.4.1(A) account for the positions of the carriers which will be used to model the microscopic currents. In order to illustrate the resonance splitting the reflection and transmission spectra for a periodic array of CW metamolecules have been computed with the FMM and are shown in Fig.4.1(B). Two distinct resonances emerge that can be associated with the before-mentioned anti-symmetric (1) and symmetric (2) modes. To visualize the symmetry of the modes, numerically calculated near-fields for the two resonance frequencies (1) and (2) are shown in Fig.4.1(C).

In order to account for the numerically observed dynamics, a suitable carrier configuration of two negatively charged (superscript "-") and two positively charged (superscript "+") carriers is assumed with their positions as sketched in Fig.4.1(A)

$$\mathbf{r}_1^+ = [0, 0, z_0]^T, \ \mathbf{r}_1^- = [\xi_1(t), 0, z_0]^T,$$
$$\mathbf{r}_2^+ = [0, 0, -z_0]^T, \ \mathbf{r}_2^- = [\xi_2(t), 0, -z_0]^T. \tag{4.1}$$

Thereby, only negatively charged carriers are considered to perform oscillations[3] $\xi_{1,2}(t)$ which are induced by the microscopic electric field as[4]

$$\frac{\partial^2}{\partial t^2}\xi_1(t) + \gamma_1\frac{\partial}{\partial t}\xi_1(t) + \omega_{01}^2\xi_1(t) + \sigma\xi_2(t) = -\frac{q_1}{m_1}\mathfrak{E}_x(z + z_0, t), \tag{4.2}$$

$$\frac{\partial^2}{\partial t^2}\xi_2(t) + \gamma_2\frac{\partial}{\partial t}\xi_2(t) + \omega_{02}^2\xi_2(t) + \sigma\xi_1(t) = -\frac{q_2}{m_2}\mathfrak{E}_x(z - z_0, t). \tag{4.3}$$

In addition to the well-known terms in the oscillator equations (4.2, 4.3) such as the damping constants $\gamma_j$ and the eigenfrequencies $\omega_{0j}$, the two equations are coupled denoted by the coupling constant $\sigma$. This coupling accounts for the near-field interaction that takes place between the two metal wires forming the CW metamolecule. Without this coupling the symmetric and the anti-symmetric modes would be degenerated in their resonance frequencies. A decoupling could be achieved by separating both wires far beyond the typical near-field coupling distances, which are in the order of $\approx 20$ nm for optical frequencies. This case would clearly violate the sub-wavelength restriction in propagation direction [ZDU+08]. With the oscillator equations it is possible to calculate the bound carrier dynamics for an isolated CW metamolecule and to find the desired molecular quantities: electric dipole moment (2.28), electric quadrupole

---

[3]This assumption corresponds to the approximation of the quasi-free-electron motion above a positively charged background.

[4]Note that the interaction of the magnetic field with charged carriers is neglected since a non-relativistic dynamic is assumed ($\partial_t|\mathbf{r}|/c << 1$).

moment (2.29), and the magnetic dipole moment (2.45)

$$\mathbf{p}_{\text{CW}} = \sum_{l=1}^{N} q_l \mathbf{r}_l = \begin{pmatrix} -q[\xi_1(t) + \xi_2(t)] \\ 0 \\ 0 \end{pmatrix}, \tag{4.4}$$

$$\hat{\mathbf{Q}}_{\text{CW}} = 3\sum_{l=1}^{N} q_l [\mathbf{r}_l]_\alpha [\mathbf{r}_l]_\beta = -3q \begin{pmatrix} [\xi_1^2(t) - \xi_2^2(t)] & 0 & z_0[\xi_1(t) - \xi_2(t)] \\ 0 & 0 & 0 \\ z_0[\xi_1(t) - \xi_2(t)] & 0 & 0 \end{pmatrix}, \tag{4.5}$$

$$\mathbf{m}_{\text{CW}} = \frac{1}{2}\sum_{l=1}^{N} q_l \mathbf{r}_l \times \frac{\partial}{\partial t}\mathbf{r}_l = -\frac{q z_0}{2} \begin{pmatrix} 0 \\ \frac{\partial}{\partial t}[\xi_1(t) - \xi_2(t)] \\ 0 \end{pmatrix}. \tag{4.6}$$

For the sake of simplicity, a symmetric CW metamolecule is assumed with $\gamma_1 = \gamma_2 \equiv \gamma$, $\omega_{01} = \omega_{02} \equiv \omega_0$, and $q_1 = q_2 \equiv q$. It is obvious from Eqs.(4.4-4.6) that all moments depend either on the sum or the difference of the oscillator elongations $\xi_j$. Explicitly, the electric dipole resonance depends on the sum, while both second order multipole moments are proportional to the difference. Hence, for the symmetric mode ($\xi_1 = \xi_2$) the electric dipole moment is maximized and both second order moments vanish. In turn, for a completely anti-symmetric elongation ($\xi_1 = -\xi_2$) second order moments are maximal and the electric dipole moment is zero. The respective wave equation which describes the propagation of electromagnetic fields inside a macroscopic material comprising up to second order multipoles upon temporal Fourier transformation [Eqs.(2.51)] reads as

$$\Delta\mathbf{E}(\mathbf{r}, \omega) + \frac{\omega^2}{c^2}\mathbf{E}(\mathbf{r}, \omega) + \frac{\omega^2}{c^2\epsilon_0}\left[\mathbf{P}(\mathbf{r}, \omega) - \nabla \cdot \hat{\mathbf{Q}}(\mathbf{r}, \omega) + \frac{i}{\omega}\nabla \times \mathbf{M}(\mathbf{r}, \omega)\right] = 0. \tag{4.7}$$

For $x$-polarized transverse electric fields propagating in $z$-direction and by Fourier transformation and substitution of the multipole moments (4.4-4.6), Eq.(4.7) simplifies to the scalar equation

$$\frac{\partial^2}{\partial z^2}E_x(z, \omega) + \frac{\omega^2}{c^2}E_x(z, \omega) + \frac{\omega^2}{c^2\epsilon_0}\left[P_x(z, \omega) - \frac{\partial}{\partial z}Q_{xz}(z, \omega) - \frac{i}{\omega}\frac{\partial}{\partial z}M_y(z, \omega)\right] = 0. \tag{4.8}$$

Prior to solving this equation for particular field distributions, there is one important point to be mentioned. The macroscopic quantities $\mathbf{P}$, $\mathbf{Q}$, $\mathbf{M}$ according to Eqs.(2.34,2.35,2.44) have been obtained by basically summing up over all molecular quantities. It is assumed that the corrections due to interactions of metamolecules can be neglected, since the metamolecules are well separated. This decoupling is hard to achieve for realistic metamaterials since even a weak coupling between adjacent metamolecules causes a shift of resonance frequencies when compared to the isolated metamolecule [FKH+10, SFVK09, DLW09]. To include this effect, either a more sophisticated averaging procedure[5] or adapted oscillator parameters can be used.

---

[5]In principle the Clausius Mosotti formalism can be applied where the Lorenz field interaction between

Because properties of isolated metamolecules are hardly accessible since typically ensembles of metamaterials are considered this interaction will be incorporated in form of adapted oscillator parameters, being the numerically and experimentally accessible ensemble values.

Determining the averaged quantities [Eqs.(2.34,2.35,2.44)] from the molecular moments (4.4-4.6) in the Fourier domain [Eq.(2.51)]

$$
\begin{aligned}
\mathbf{P}(\mathbf{r}, \omega) &= \eta \mathbf{p}_{\mathrm{CW}}(\mathbf{r}, \omega), & (4.9) \\
\hat{\mathbf{Q}}(\mathbf{r}, \omega) &= \frac{\eta}{6} \hat{\mathbf{Q}}_{\mathrm{CW}}(\mathbf{r}, \omega), & (4.10) \\
\mathbf{M}(\mathbf{r}, \omega) &= \eta \mathbf{m}_{\mathrm{CW}}(\mathbf{r}, \omega), & (4.11)
\end{aligned}
$$

with the number density $\eta$ and substituting them into Eq.(4.8) yields

$$
\frac{\partial^2}{\partial z^2} E_x(z, \omega) + \frac{\omega^2}{c^2} E_x(z, \omega) - \frac{\omega^2 \eta q}{c^2 \epsilon_0} \left\{ [\xi_1(\omega) + \xi_2(\omega)] - z_0 \frac{\partial}{\partial z} [\xi_1(\omega) - \xi_2(\omega)] \right\} = 0.
$$
$$(4.12)$$

The first term $\xi_1(\omega) + \xi_2(\omega)$ in the brackets represents the electric dipole interactions whereas the second term $\propto \partial_z[\xi_1(\omega) - \xi_2(\omega)]$ arises from both the electric quadrupole and the magnetic dipole interactions. Now, the remaining task is to evaluate these two contributions as functions of the averaged electric field $E_x(z, \omega)$. Thus, from Eqs.(4.2, 4.3) and by replacing the microscopic with the macroscopic field according to Eq.(2.16) one ends up with

$$
\begin{aligned}
\xi_1(\omega) + \xi_2(\omega) &= -\frac{q}{m} \frac{E_x(z + z_0, \omega) + E_x(z - z_0, \omega)}{A(\omega) + \sigma}, & (4.13) \\
\xi_1(\omega) - \xi_2(\omega) &= -\frac{q}{m} \frac{E_x(z + z_0, \omega) - E_x(z - z_0, \omega)}{A(\omega) - \sigma}, & (4.14) \\
\text{with } A(\omega) &\equiv \omega_0^2 - \omega^2 - i\omega\gamma. & (4.15)
\end{aligned}
$$

Now, if an ansatz for the propagating modes inside the metamaterial like

$$
E_x(z, \omega) = E_0 e^{ik_z(\omega)z}, \tag{4.16}
$$

is substituted into the wave equation (4.12), the dispersion relation can be obtained as

$$
k_z^2(\omega) = \frac{\omega^2}{c^2} \left\{ 1 + \frac{\eta q^2 2}{\epsilon_0 m} \frac{\cos[k_z(\omega)z_0]}{A(\omega) + \sigma} + \frac{\eta q^2 2}{\epsilon_0 m} \frac{z_0 k_z(\omega) \sin[k_z(\omega)z_0]}{A(\omega) - \sigma} \right\}. \tag{4.17}
$$

Analyzing the functional form of the implicit equation (4.17), it can be easily verified that this equation has various solutions $k_z(\omega)$ for a fixed frequency. These solutions represent different branches of the dispersion relation, i.e., different propagating modes. For CW metamolecules having larger dimensions $z_0$ in propagation direction, higher-order propagationg modes have to be considered. For CW metamolecules with a small extend in the propagation direction only the fundamental mode occurs. Hence, for such metamaterials operating in the fundamental

---

metamolecules can be considered in dependence on the metamaterial's volume density, see section 2.1.3.

mode regime the trigonometric functions in Eq.(4.17) may be expanded in a Taylor series up to the first non-constant contribution

$$\cos[k_z(\omega)z_0] \approx 1 - \frac{k_z^2(\omega)z_0^2}{2}, \qquad \sin[k_z(\omega)z_0] \approx k_z(\omega)z_0, \qquad (4.18)$$

which provides an explicit form of the dispersion relation $k_z(\omega)$ for the fundamental mode

$$k_z^2(\omega) = \frac{\omega^2}{c^2} \frac{1 + \frac{C}{A(\omega)+\sigma}}{1 - \frac{\omega^2}{c^2}\frac{Cz_0^2}{2}\frac{A(\omega)+3\sigma}{A(\omega)^2-\sigma^2}}, \qquad \text{with } C \equiv \frac{2\eta q^2}{m\epsilon_0}. \qquad (4.19)$$

In addition to the dispersion relation Eq.(4.19), also the effective material properties according to Eqs.(2.55, 2.56) may be assigned. For the effective electric permittivity one ends up with

$$\epsilon_x(k_z, \omega) = 1 + \frac{C}{A(\omega)+\sigma} + k_z^2(\omega)z_0^2 \frac{C\sigma}{A^2(\omega)-\sigma^2}. \qquad (4.20)$$

Considering Eq.(4.20) it can be inferred that spatial dispersion occurs, as indicated by the intrinsic $k_z(\omega)$-dependence of the permittivity for the fundamental mode approximation.

The magnetic permeability can be similarly obtained according to Eq.(2.56)

$$\mu_y(z, \omega) = B_y(z, \omega)[B_y(z, \omega) - \mu_0 M_y(z, \omega)]^{-1}, \qquad (4.21)$$

where the magnetic induction $B_y(z, \omega) = [k_z(\omega)/\omega]E_x(z, \omega)$ has to be replaced by the electric field. Finally, this results again in a spatially dispersive expression

$$\mu_y(k_z, \omega) = \left\{1 - \frac{\omega^2}{c^2}\frac{\eta q^2}{m\epsilon_0}\frac{z_0 \sin[k_z(\omega)z_0]}{k_z(\omega)[A(\omega)-\sigma]}\right\}^{-1}. \qquad (4.22)$$

Upon substitution of the approximations (4.18), one ends up with

$$\mu_y(\omega) = \left\{1 - \frac{\omega^2}{c^2}\frac{Cz_0^2}{2[A(\omega)-\sigma]}\right\}^{-1}, \qquad (4.23)$$

which, in contrast to the effective permittivity, is not spatially dispersive, i.e., $\mu_y(k_z, \omega) = \mu_y(\omega)$ for the applied fundamental mode approximation of $k_z(\omega)z_0 << 1$.

In order to apply the developed formalism to a realistic CW metamaterial [PMC+08], numerical FMM simulations of a slab of periodically arranged CW metamolecules have been performed. The lateral periods of $\Lambda_x = 600$ nm and $\Lambda_y = 500$ nm have been used. The CW metamolecule has a single wire extension in $x$- and $y$-direction of 400 nm and 150 nm, respectively, and a thickness of 40 nm in $z$-direction. Both wires are 25 nm separated, yielding a total slab thickness of 105 nm. The far-field reflection and transmission spectra for such a slab have been already shown in Fig.4.1(B). On the basis of these spectral results the effective parameters for normal incidence can be estimated [SVKS05]. These are approximative since they are associated to a homogeneous slab for which the spatial dispersion is neglected. Considering the spatial dispersion in Eqs.(4.20,4.23) one can anticipate that this is solely con-
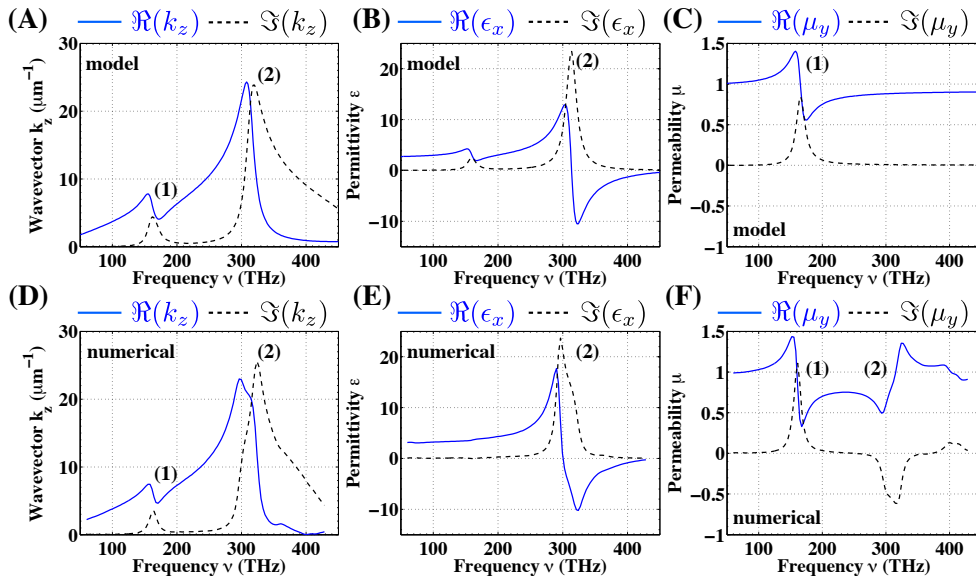
**Figure 4.2:** In the first row the (A) dispersion relation, (B) permittivity, and (C) permeability values for the multipole model are shown, whereas on the second row the respective numerically obtained observables are shown for a slab of periodically arranged CW metamolecules. Solid lines represent the real part, while dashed lines label the imaginary part.

nected to the parameter $z_0$. This is due to several reasons. At first, $2z_0$ is the dimension of metamolecules in propagation direction, enabling the observation of second order multipoles. It can be easily proven that for vanishing $z_0$, second order multipoles become zero. Second, $z_0$ is related to the phase accumulation of the electric field evolution upon propagating through the metamaterial according to Eqs.(4.13, 4.14). This field difference is essential in order to excite any anti-symmetric currents that are required for second order excitations, i.e., magnetic dipoles. Due to the dependence of multipole moments on the fields, the non-local response translates into the dispersion relation as well as into the effective material parameters.

In order to evaluate the dispersion relation (4.19), the permittivity (4.20) and the permeability (4.23) the unknown values $\omega_0$, $\gamma$, $\sigma$ and $C$ have to be determined. This can be achieved by fitting one of the quantities $k_z(\omega)$, $\epsilon_x(\omega)$, or $\mu_y(\omega)$ to the respective numerical result. The remaining two quantities are then fixed and can be computed without further adaption. For the results shown in Fig.4.2(A-F) the numerical dispersion relation has been used to fix the parameters of the model, whereas the permittivity and the permeability follow directly. When comparing analytical and numerical results major discrepancies can be only observed in the magnetic permeability [Fig.4.2(C,F)]. There an anti-resonance feature of the numerical data is not present in the multipole model. To conclude this comparison for the CW metamaterial, it is stated that all relevant numerically observed effects can be simultaneously observed in the multipole model.

After the comprehensive presentation of the approach at the example of the CW metamolecule, which allowed to calculate experimentally accessible and relevant quantities, the model can be applied to describe various other metamolecules [PMC+08, PCT+09]. A major advantage of the presented modeling is that numerically obtained results can be unambiguously linked to a physical meaning beyond the phenomenological interpretation of observed

69

effects in terms of multipolar excitations. It has been even shown that also quantitative results can be achieved. But since the model is based on parameters that have to be determined the prediction of new metamolecule properties is only possible to a certain extent, as will be shown in the following section 4.1.2.

Before this is done, a brief explanation why the presented model for a certain metamaterial has to be fitted to either experimental or numerical data is given. For ordinary materials operating in the electric dipole limit a similar oscillator ansatz is typically chosen, where usually one uncoupled oscillator is sufficient. In order to fix the material parameters, i.e., the permittivity, this model has to be compared to experimental measurements, preferably by means of reflection and transmission measurements at thin films [JC72]. However, depending on the microscopic carrier dynamics these parameters are different for each material. Strictly speaking, the presented model requires that for each metamaterial these parameters have to be determined again. By changing the mesoscopic geometry, the entire metamaterial is modified, and thus requires a new fitting of the parameters. To illustrate that the presented model is just a consequent continuation of the description of natural materials, we set $z_0 = 0$, which is equivalent to consider only one oscillator in the origin which makes $\sigma$ meaningless. With this step all second order multipole moments (2.52, 2.53) vanish. The magnetic permeability (4.23) becomes unity and the electric permittivity (4.20) takes the form of

$$\epsilon(\omega) = 1 + \frac{C}{A(\omega)} = 1 + \frac{C}{\omega_0^2 - \omega^2 - i\omega\gamma}, \tag{4.24}$$

which, depending on the presence of $\omega_0$ in $A(\omega)$, provides the well-known Drude metal or a polar material featuring a Lorenzian resonance. Although the CW metamolecule described in this section is rather simple, several important physical features have been already observed, such as optical magnetism, the occurrence of spatial dispersion and higher-order dispersion branches, which help to facilitate the understanding of metamaterials by means of fundamental electrodynamic principles.

## 4.1.2 Split-Ring Resonator metamolecule and planar modifications enabling asymmetric transmission

In this section, metamaterials composed of planar metamolecules are investigated [PCT+10]. The major part of this section is devoted to the question, to what extend the introduced multipole model of section 4.1.1 allows to predict the properties of new metamaterials. Hence, an original metamolecule is considered at first, which will be modified later on. As will be shown, the parameters of the modified metamolecule will be correctly predicted by the multipole model.

These modifications are extended to cover effects associated with asymmetric transmission for circularly polarized light [ZNG09, FSZ+07, SPM+09, ZDW+09]. The planar SRR [LEW+04], Fig.4.3(A), serves as the original metamolecule. The SRR, similar to the CW metamolecule before, is a pioneering metamolecule being subject of many investigations [DLW09,
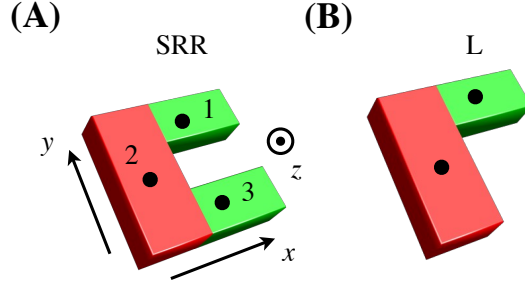
**Figure 4.3:** Illustration of (A) the SRR, and (B) the L metamolecule [CKK$^+$05]. Both metamolecules are arranged in the $xy$-plane, hence the propagation vector is assumed to be normal to the surface, i.e., parallel to the $z$-direction. The dots denote the carrier configuration assumed for the analytical model.

KKK$^+$05, RLE$^+$06, HKF$^+$08, LGF$^+$08, LLZG09, PWAB10]. The structure has been initially proposed for microwave frequencies [PHRS99, Tre05]. Thereby, the SRR can be conceptually replaced by a miniaturized LC-circuit[6]. Here, the SRR will be discussed in the optical frequency domain, but already from the simple LC-model it may be anticipated that the SRR exhibits both a magnetic and an electric response.

In the following the polarization eigenstates of metamaterials consisting of SRR metamolecules are shown to be linearly polarized. Moreover, the optical response in terms of effective parameters and the reflection and transmission coefficients will be calculated. Next, it will be revealed that for particular geometrical modifications [Fig.4.3(B)] on the SRR metamolecule the polarization eigenstates change toward elliptical polarization. Even though this is a drastic change in the optical functionality, it is shown that the multipole model will correctly predict the changed optical response for these modifications.

In order to describe the internal carrier dynamics for the SRR, conceptually consisting of three connected straight wire pieces, the following microscopic carrier configuration is assumed

$$
\begin{aligned}
\mathbf{r}_1^+ &= [0, y_0, 0]^T, \ \mathbf{r}_1^- = [\xi_1(t), y_0, 0]^T, \\
\mathbf{r}_2^+ &= [-x_0, 0, 0]^T, \ \mathbf{r}_2^- = [-x_0, \xi_2(t), 0]^T, \\
\mathbf{r}_3^+ &= [0, -y_0, 0]^T, \ \mathbf{r}_3^- = [\xi_3(t), -y_0, 0]^T.
\end{aligned}
\tag{4.25}
$$

A set of three coupled microscopic oscillators is proposed to account for the coupling between the conductively connected wires

$$
\begin{aligned}
\frac{\partial^2}{\partial t^2}\xi_1(t) + \gamma_1\frac{\partial}{\partial t}\xi_1(t) + \omega_{01}^2\xi_1(t) + \sigma_{21}\xi_2(t) &= -\frac{q_1}{m}\mathfrak{E}_x(z,t), \\
\frac{\partial^2}{\partial t^2}\xi_2(t) + \gamma_2\frac{\partial}{\partial t}\xi_2(t) + \omega_{02}^2\xi_2(t) + \sigma_{21}\xi_1(t) - \sigma_{23}\xi_3(t) &= -\frac{q_2}{m}\mathfrak{E}_y(z,t), \\
\frac{\partial^2}{\partial t^2}\xi_3(t) + \gamma_3\frac{\partial}{\partial t}\xi_3(t) + \omega_{03}^2\xi_3(t) - \sigma_{23}\xi_2(t) &= -\frac{q_3}{m}\mathfrak{E}_x(z,t).
\end{aligned}
\tag{4.26}
$$

It is assumed that wire 1 and wire 3 are equal, but different to the SRR base wire 2. Hence, Eqs.(4.26) can be simplified with: $\omega_{01} = \omega_{03} \equiv \omega_x$, $\omega_{02} \equiv \omega_y$, $\gamma_1 = \gamma_3 \equiv \gamma_x$, $\gamma_2 \equiv$

---

[6]"L" is an abbreviation for an inductor, while "C" accounts for a capacitor in circuit theory.

$\gamma_y$, $\sigma_{12} = \sigma_{23} \equiv \sigma$, and $q_1 = q_3 \equiv q_x$, $q_2 \equiv q_y$. Next, the mesoscopic multipole contributions Eqs.(2.28,2.29,2.45) have been evaluated for the carrier distribution (4.25). The resulting molecular SRR multipole moments are

$$\mathbf{p}_{\mathrm{SRR}} = \begin{pmatrix} q_x[\xi_1(t) + \xi_3(t)] \\ q_y\xi_2(t) \\ 0 \end{pmatrix}, \tag{4.27}$$

$$\hat{\mathbf{Q}}_{\mathrm{SRR}} = 3 \begin{pmatrix} -q_x[\xi_1^2(t) + \xi_3^2(t)] & -q_xy_0[\xi_1(t) - \xi_3(t)] + q_yx_0\xi_2(t) & 0 \\ -q_x[\xi_1(t) - \xi_3(t)] + q_yx_0\xi_2(t) & -q_y\xi_2^2(t) & 0 \\ 0 & 0 & 0 \end{pmatrix}, \tag{4.28}$$

$$\mathbf{m}_{\mathrm{SRR}} = \frac{1}{2} \begin{pmatrix} 0 \\ 0 \\ q_xy_0\frac{\partial}{\partial t}[\xi_1(t) - \xi_3(t)] + q_yx_0\frac{\partial}{\partial t}\xi_2(t) \end{pmatrix}. \tag{4.29}$$

For arbitrary carrier dynamics $\xi_j(t)$, $j \in [1, 2, 3]$, molecular electric dipole moments in $x$- and $y$-direction, a magnetic moment in $z$-direction and electric quadrupole moments $Q_{ij}$, $[i, j] \in [x, y]$ are induced. Hence, even after the transition to averaged quantities (4.9-4.11) the wave equation (4.8), describing $x$-polarized electric fields propagating in $z$-direction, has no contributions stemming from second order multipole moments. As can be easily verified, these conclusions hold for $y$-polarized electric fields propagating in $z$-direction as well. Thus, the entire optical response is described by the macroscopic polarization

$$\mathbf{P}(z, \omega) = \eta\mathbf{p}_{\mathrm{SRR}}(z, \omega) = -\eta \begin{pmatrix} q_x[\xi_1(\omega) + \xi_3(\omega)] \\ q_y\xi_2(\omega) \\ 0 \end{pmatrix}. \tag{4.30}$$

Similar to the CW metamolecule the oscillator elongations according to the set of equations (4.26) are simply obtained in Fourier domain (2.51). For $x$-polarization one obtains

$$\xi_1(\omega) = \xi_3(\omega) = -\frac{q_x}{m}\frac{1}{A_x(\omega)}E_x(z, \omega), \tag{4.31}$$

$$\xi_2(\omega) = 0, \tag{4.32}$$

whereas for $y$-polarized electric fields we have

$$\xi_1(\omega) = -\xi_3(\omega) = -\frac{q_y}{m}\frac{\sigma}{A_x(\omega)A_y(\omega) - 2\sigma^2}E_y(z, \omega), \tag{4.33}$$

$$\xi_2(\omega) = -\frac{q_y}{m}\frac{A_x(\omega)}{A_x(\omega)A_y(\omega) - 2\sigma^2}E_y(z, \omega), \tag{4.34}$$

$$\text{with } A_{x,y}(\omega) \equiv \omega_{x,y}^2 - \omega^2 - i\omega\gamma_{x,y}. \tag{4.35}$$

Considering Eqs.(4.31-4.35) it becomes obvious that $x$-polarized electric fields induce only a polarization in $x$-direction, because $\xi_2(\omega) = 0$. In turn, $y$-polarized light induces a polarization
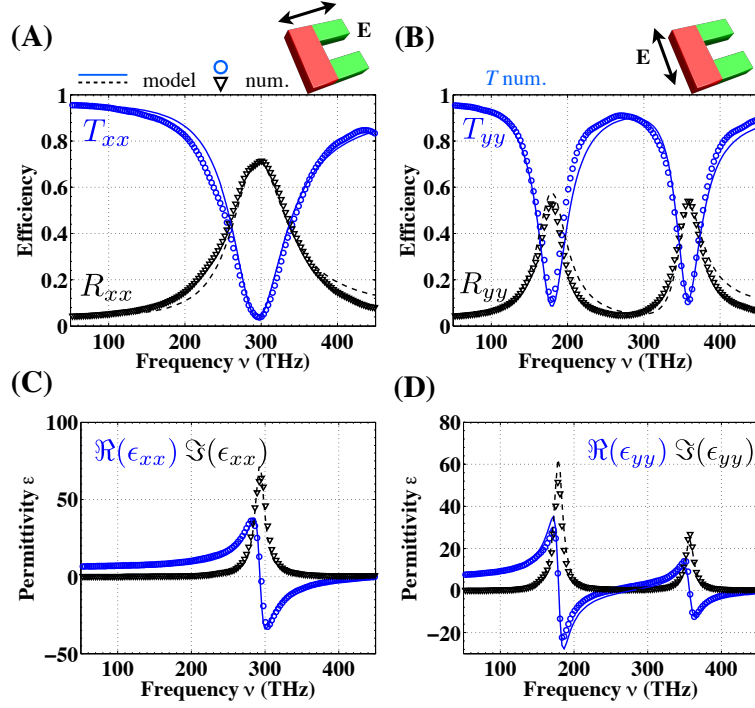
**Figure 4.4:** The SRR far-field spectra obtained by numerical simulation (T circles, R triangles) and for the developed model (T solid, R dashed) for (A) $x$-polarization and (B) for $y$-polarization. (C,D) The corresponding complex permittivities obtained by the parameter retrieval of the numerical spectra in comparison to predictions from Eq.(4.36) for the respective polarization direction.

solely in $y$-direction due to the annihilation of the carrier dynamics in wire 1 and 3 $[\xi_1(\omega) = -\xi_3(\omega)]$. In other words, the electric permittivity (2.55) is a *diagonal tensor* and consequently the polarization eigenstates are *linearly polarized*

$$\hat{\epsilon}(\omega) = \begin{pmatrix} \epsilon_{xx}(\omega) & 0 & 0 \\ 0 & \epsilon_{yy}(\omega) & 0 \\ 0 & 0 & 1 \end{pmatrix}, \tag{4.36}$$

$$\epsilon_{xx}(\omega) = 1 + \frac{2\eta q_x^2}{m\epsilon_0} \frac{1}{A_x(\omega)}, \tag{4.37}$$

$$\epsilon_{yy}(\omega) = 1 + \frac{\eta q_y^2}{m\epsilon_0} \frac{A_x(\omega)}{A_x(\omega)A_y(\omega) - 2\sigma^2}. \tag{4.38}$$

In turn, the magnetic permeability is unity for both polarization directions as expected for media comprising electric dipole interaction only. With Eqs.(4.37,4.38) it is now possible to calculate the reflection and transmission coefficients by applying a standard transfer matrix formalism for films [BW99]. For reference, the SRR spectrum has been computed at first numerically with the FMM and secondly by calculating and fitting the spectra of a metamaterial slab incorporating the permittivity derived above.

Spectra for polarization in $x$- and $y$-directions are shown in Fig.4.4(A,B), respectively. The SRR metamaterial has been selected similarly to the one investigated in the literature [LEW+04, PCT+10]. The SRR wires are 200 nm long and 50 nm wide, the SRR base has a length of 100 nm and a width of 80 nm. The entire SRR thickness is 25 nm and it is made of

gold [JC72]. A periodical arrangement with a period of 400 nm in both $x$- and $y$-direction has been assumed. The thickness of the metamaterial corresponds to the thickness of the SRR. In addition, the permittivity has been obtained from the numerical spectra by the parameter retrieval that has been used for the CW pairs before. Comparing this retrieved permittivity to the one that has been found in the spectral fit for the reflection and transmission spectra almost perfect coincidence is observed [Fig.4.4(C,D)]. Hence, the developed formalism can be applied as a kind of parameter retrieval procedure. In addition to the permittivity, the formalism may be useful in order to quantify the coupling between the SRR wire pieces.

Next, the SRR metamolecule is modified yielding the L metamolecule [CKK$^+$05], see Fig.4.3 (B), where one of the SRR arms (3) has been removed. This modification prevents the mutual cancellation of the carrier dynamics in wire 1 and 3 when compared to the original SRR metamolecule. The solutions for the oscillator elongations are

$$\xi_1^x(\omega) = -\frac{q_x}{m}\frac{A_y(\omega)}{A_x(\omega)A_y(\omega) - \sigma^2}E_x(z,\omega), \tag{4.39}$$

$$\xi_2^x(\omega) = -\frac{q_x}{m}\frac{\sigma}{A_x(\omega)A_y(\omega) - \sigma^2}E_x(z,\omega), \tag{4.40}$$

for polarization in $x$-direction and

$$\xi_1^y(\omega) = -\frac{q_y}{m}\frac{\sigma}{A_x(\omega)A_y(\omega) - \sigma^2}E_y(z,\omega), \tag{4.41}$$

$$\xi_2^y(\omega) = -\frac{q_y}{m}\frac{A_x(\omega)}{A_x(\omega)A_y(\omega) - \sigma^2}E_y(z,\omega), \tag{4.42}$$

in $y$-direction. Since one of the SRR arms has been removed, one oscillator elongation can be set to zero. Hence, an electric field polarized in $x$-direction induces a cross-polarization in $y$-direction and *vice versa*. For the permittivity that is calculated from the polarization (4.30) upon setting $\xi_3(\omega) = 0$ these cross-polarizabilities result in non-zero off-diagonal elements

$$\hat{\epsilon}(\omega) = \begin{pmatrix} \epsilon_{xx}(\omega) & \epsilon_{xy}(\omega) & 0 \\ \epsilon_{yx}(\omega) & \epsilon_{yy}(\omega) & 0 \\ 0 & 0 & 1 \end{pmatrix}, \tag{4.43}$$

$$\epsilon_{xx}(\omega) = 1 + \frac{q_x^2\eta}{m\epsilon_0}\frac{A_y(\omega)}{A_x(\omega)A_y(\omega) - \sigma^2}, \tag{4.44}$$

$$\epsilon_{yy}(\omega) = 1 + \frac{q_y^2\eta}{m\epsilon_0}\frac{A_x(\omega)}{A_x(\omega)A_y(\omega) - \sigma^2}, \tag{4.45}$$

$$\epsilon_{yx}(\omega) = \epsilon_{xy}(\omega) = \frac{q_xq_y\eta}{m\epsilon_0}\frac{\sigma}{A_x(\omega)A_y(\omega) - \sigma^2}. \tag{4.46}$$

If $A_x(\omega) \neq A_y(\omega)$, which is fulfilled for different geometries of wires (1) and (2), the permittivity tensor cannot be diagonalized. Thus, the polarization eigenstates are in general *elliptically polarized* [ZNG09]. In order to verify these analytical considerations the spectral response of the L metamolecule has been numerically modeled using FMM. For media which are described by a permittivity according to Eq.(4.43) the reflectivity and transmissivity have
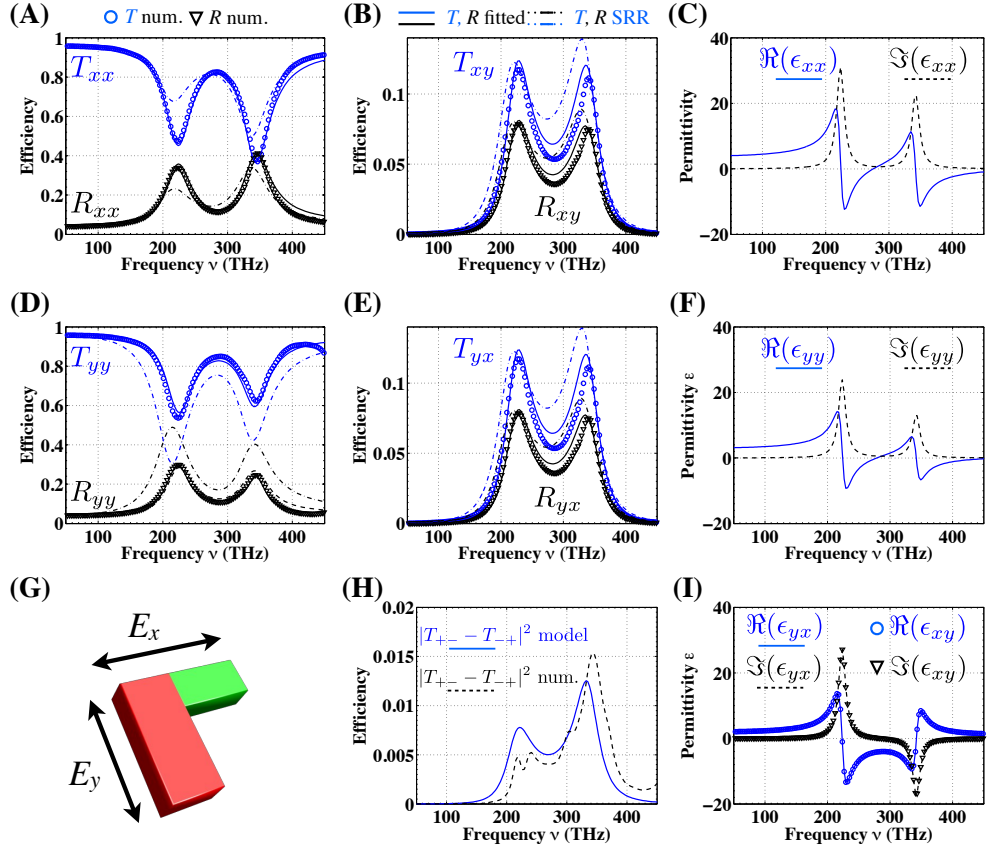
**Figure 4.5:** The (A) far-field spectra, (B) the cross-polarized spectral quantities $T_{xy}$, $R_{xy}$, and (C) the permittivity for $x$-polarization. (D,E,F) The respective results for $y$-polarization. The spectra predicted by the SRR values in (A,B,D,E) are labeled by dashed dotted lines, whereas the directly fitted values correspond to the solid lines. The permittivities (C,F,I) have been calculated with Eq.(4.43) using the directly fitted values. (G) The L structure made of two wires with different widths together with the two polarization directions of interest are shown. (H) The asymmetric transmission in terms of a difference between $T_{+-}$ and $T_{-+}$ is shown for the numerical and the adapted transmissivities.

to be calculated requiring more sophisticated methods. Here a homogeneous slab with the permittivity (4.43) and a thickness corresponding to the thickness of the metamolecules has been simultaneously modeled [Lie03]. In a first step, the parameters of the SRR that have been found before are applied while considering the removal of one wire. The results for both polarization directions are shown in Fig.4.5(A,B,D,E). As can be seen, the resonance positions as well as the resonance widths are predicted with only minor differences in the resonance strength, see Fig.4.5(A,C). Second, the permittivity (4.44) for the L metamolecule has been used directly to fit the numerical spectra. This improves the coincidence between the spectra predicted by the model and the numerical spectra toward almost perfect agreement. Considering the cross-polarized quantities $T_{ij}$, $R_{ij}$, $i \neq j$, agreement with sufficient accuracy is observed even for the SRR parameters [Fig.4.5(B,E)]. As a further outcome of the spectral adaption, the entire permittivity tensor can be directly obtained [Fig.4.5(C,F,I)] which is, for media that do not posses linearly polarized eigenstates, a non-trivial task. Additionally, it is mentioned that the anti-resonance observed in Fig.4.5(I) can be fully explained by the mutual interplay of the coupled carriers[PCT+10].

75

Finally, it will be proven that asymmetric transmission [ZNG09, FSZ$^+$07, SPM$^+$09, ZDW$^+$09] for circularly polarized light occurs, as expected from the shape of the permittivity tensor (4.43). The connection between left- ("-") and right-("+") handed circularly and linearly polarized light may be written as [ZDW$^+$09]

$$\begin{pmatrix} T_{++} & T_{+-} \\ T_{-+} & T_{--} \end{pmatrix} = \frac{1}{2} \begin{pmatrix} (T_{xx} + T_{yy}) + i(T_{xy} - T_{yx}) & (T_{xx} - T_{yy}) - i(T_{xy} + T_{yx}) \\ (T_{xx} - T_{yy}) + i(T_{xy} + T_{yx}) & (T_{xx} + T_{yy}) - i(T_{xy} - T_{yx}) \end{pmatrix}.$$
(4.47)

Considering Eq.(4.47) it becomes obvious that for non-zero, cross-polarized transmission coefficients $T_{xy}$, $T_{yx}$ the difference $T_{+-} - T_{-+}$ is non-zero, too, requiring that $T_{xy} + T_{yx} \neq 0$. For the investigated L metamolecule the results for the modulus of the difference between $T_{+-}$ and $T_{-+}$ are shown in Fig.4.5(H). The two lines correspond to the results for the numerical transmission and the ones predicted by the model. Again all main features are correctly described by the developed formalism, see Fig.4.5(H). In passing, it is mentioned that typically the effects of asymmetric transmission in planar metamolecules [PZ09, PFZ11] are rather small compared to metamolecules that additionally exhibit chiral properties due to an extension and particular shape in the propagation direction [PFMZ09, PZD$^+$09, PLF$^+$09, ZDW$^+$09].

To conclude this section, it has been shown that the planar SRR metamolecule upon normal incidence possesses electric dipole response only, which simplifies the model significantly. These findings are consistent with experimental observations, where magnetic effects, i.e., a magnetic resonance, could be only observed for angular incidence [LEW$^+$04]. Furthermore, the transition from linear toward elliptically polarized eigenstates has been performed by geometrical variations of the SRR yielding the L metamolecule. In doing so the optical response of a metamaterial composed of these L metamolecules could be estimated solely from knowing the parameters of the original SRR metamaterial [PCT$^+$10]. The formalism has been utilized to determine the permittivity tensor which can be accessed by comparing with experimental or theoretical far-field intensities without requiring the spectral phase. The developed description supports and simplifies the physical understanding of asymmetric transmission effects by the simple mutual interaction of electric dipoles. Beyond this qualitative understanding it has been shown that also quantitative agreement can be achieved.

It is furthermore mentioned that the same procedure has been also examined for an S-shaped metamolecule where similar results have been obtained [PCT$^+$10]. As an important physical property, all derived permittivities are consistent with the *Casimir-Onsager relations* [Ons31, Cas45, TSJ02] which require the symmetry in the permittivity tensor $\epsilon_{xy}(\omega) = \epsilon_{yx}(\omega)$. This relation can be proven by considering Eq.(4.46) or Fig.4.5(I).

## 4.2 Nonlinear optical properties

In the first section of chapter 4.2, the intrinsic nonlinear optical response of particular metamaterials will be discussed at the example of the SRR metamolecule. As will be shown a

quadratic nonlinearity can be obtained, which is solely attributed to the appearance of the electric quadrupole and the magnetic dipole moments. Thus, among other nonlinear contributions of second order, e.g., due to symmetry-breaking at the substrate interfaces or the presence of an adjacent nonlinear material, this *multipole nonlinearity* can be observed solely due to the intrinsic carrier dynamics of the isolated metamolecule. As an example the *second harmonic generation* (SHG) will be investigated as one of the most prominent nonlinear optical frequency conversion processes.

In the second section 4.2.2 the obtained results are discussed and compared with other approaches that are used in order to account for the intrinsic nonlinear interactions in metamolecules.

## 4.2.1 Multipole nonlinearity - Second-harmonic generation

In this section, nonlinear optical effects induced by multipole moments will be discussed. At first, the origin of this second-order nonlinearity will be motivated. Second, the SRR metamolecule will be re-examined as an example geometry. The SRR has been already discussed in section 4.1.2. In this section it will be oriented differently as compared to the planar alignment that has been considered before. As will be shown, this adapted orientation causes second-order multipoles, i.e., the magnetic dipole and the electric quadrupole moments, to become radiating in addition to the first-order electric dipole moments.

With the presented approach it will be shown that the considered nonlinear optical response of a metamaterial can be predicted solely from knowing the linear optical properties, such as the dispersion relation, or any other effective material property.

In order to motivate the source term of the nonlinearity, the definitions of the electric quadrupole (2.29) and the magnetic dipole moments (2.45) can be considered

$$(Q_m)_{\alpha\beta} = 3 \sum_{b(m)=1}^{N_{\text{bound}}} q_{b(m)} (r_{b(m)})_\alpha (r_{b(m)})_\beta, \qquad \mathbf{m}_m = \frac{1}{2} \sum_{b(m)=1}^{N_{\text{bound}}} q_{b(m)} [\mathbf{r}_{b(m)} \times \mathbf{v}_{b(m)}].$$

It becomes obvious that both are depending on terms $\propto (r_{b(m)})_\alpha \cdot (r_{b(m)})_\beta$. Assuming that the spatial coordinate $\mathbf{r}_{b(m)}$ of a bound carrier is proportional to the microscopic electric field[7] $\mathfrak{E}$, both second-order multipoles produce the quadratic expressions $\mathfrak{E} : \mathfrak{E}$. Hence, it can be expected that quadratic, i.e., second-order, nonlinear effects emerge.

Conveying this knowledge to the SRR metamolecule, this multipole nonlinearity may be anticipated at all 90°-bends of the SRR. There, the carrier motion exhibits a two-dimensional oscillation, i.e., in $x$- and $y$-direction, simultaneously. The SRR metamolecule is shown in Fig.4.6(A), where the currents for the first two fundamental LPP modes are sketched [RLE+06]. The metamolecule is excited by plane waves with a polarization direction of the impinging electric field along the $x$-direction with a propagation along the $y$-axis. In order to illustrate the two modes, FDTD simulations have been performed of a particular gold

---

[7]This has been inherently used by the oscillator equations for the CW and the SRR metamolecule, e.g., in Eq.(4.26,4.2).
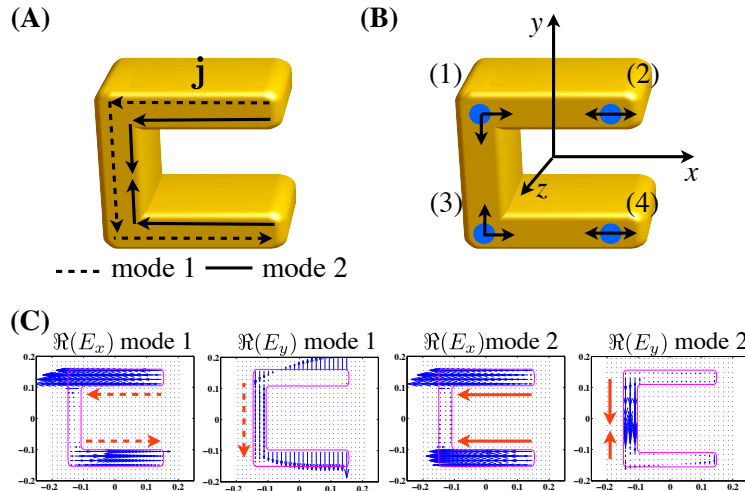
**Figure 4.6:** (A) The SRR metamolecule together with the two fundamental currents associated with the magnetic LPP resonance (mode 1) and electric LPP resonance (mode 2). (B) The corresponding carrier distribution proposed to resolve the currents shown in (A) and to particularly account for the two-dimensional oscillations at the SRR bends [carriers (1) and (3)]. (C) FDTD results for the electric field distributions inside the SRR for the two fundamental modes.

SRR metamolecule [PCT$^+$09], showing the electric field distributions[8] for both modes, see Fig.4.6(C)[9]. For such illumination conditions, also higher-order modes of the SRR can be excited. As it will be shown, they can be observed at higher frequencies, when compared to the resonance frequencies of the two lowest-order modes. For simplicity, emphasis will be put on these two lowest-order modes only. However, this simplification is not a restriction since higher-order LPP modes can be considered in complete analogy to the following approach. A comprehensive numerical investigation of the LPP modes of the SRR at optical frequencies has been performed by *Rockstuhl et al.* [RLE$^+$06].

In order to precisely account for the two-dimensional carrier oscillations in the SRR bends, a deviating carrier configuration as compared to the one of section 4.1.2 has to be applied, see Fig.4.6(B). It can be depicted that the charge configuration consists of four carriers, whereas carriers (1) and (3) are located in the center of the bends. The additionally sketched arrows in Fig.4.6(B) indicate the degree of freedom for the carrier motion. Moreover, this carrier configuration represents the simplest alignment, with only one additional carrier, compared with the three-carrier-setup in the previous section. The carrier configuration applied for the SRR here can be regarded as a balance between the following requirements. It is chosen to be able to account for the two lowest-order LPP modes, the two-dimensional carrier motion at the bends and finally it should be as simple as possible for the calculation of the nonlinear response in the following.

---

[8]The respective currents can be easily obtained by multiplying the microscopic electric fields with the conductivity $\sigma_{\text{cond.}}$ of the respective SRR composite metal, i.e., $j = \sigma_{\text{cond.}}\mathfrak{E}$. Hence, it can be assumed that $j \propto \mathfrak{E}$.

[9]The dimensions of the SRR are shown in Fig.4.7(D)

78

Thus, a suitable carrier configuration for this task could be

$$
\begin{aligned}
\mathbf{r}_1^+ &= [-x_0, y_0, 0]^T, \ \ \mathbf{r}_1^- = [-x_0 - \xi_1, y_0 - \xi_1, 0]^T, \\
\mathbf{r}_2^+ &= [x_0, y_0, 0]^T, \ \ \mathbf{r}_2^- = [x_0 - \xi_1, y_0, 0]^T, \\
\mathbf{r}_3^+ &= [-x_0, -y_0, 0]^T, \ \ \mathbf{r}_3^- = [-x_0 - \xi_2, -y_0 + \xi_2, 0]^T, \\
\mathbf{r}_4^+ &= [x_0, -y_0, 0]^T, \ \ \mathbf{r}_4^- = [x_0 - \xi_2, -y_0, 0]^T.
\end{aligned}
\tag{4.48}
$$

Again, the dynamic variables $\xi_{1,2}(t)$ account for the elongation of the negatively charged carrier oscillations driven by the external electric field $\mathfrak{E}$. The parameters $x_0$ and $y_0$ are defined by the size of the SRR and correspond to the locations shown in Fig.4.6(B). Thus, the carrier motion reduces to a set of two oscillator equations according to

$$
\frac{\partial^2}{\partial t^2}\xi_1(t) + \gamma \frac{\partial}{\partial t}\xi_1(t) + \omega_0^2 \xi_1(t) + \sigma \xi_2(t) = -\frac{q}{m}\mathfrak{E}_x(y + y_0, t),
\tag{4.49}
$$

$$
\frac{\partial^2}{\partial t^2}\xi_2(t) + \gamma \frac{\partial}{\partial t}\xi_2(t) + \omega_0^2 \xi_2(t) + \sigma \xi_1(t) = -\frac{q}{m}\mathfrak{E}_x(y - y_0, t).
\tag{4.50}
$$

The set of equations (4.49,4.50) is exactly the same as applied for the CW metamolecule, see Eqs.(4.2,4.3) in section 4.1.1, but the carrier configuration and their degrees of freedom are substantially different, see Eqs.(4.48). In Eqs.(4.49,4.50) it has been assumed that all positively charged carriers $q_j^+ = q$, while for all negatively charged carriers $q_j^- = -q$, $\forall\, j \in [1, 2, 3, 4]$. Again, the constant $\sigma$ accounts for the coupling of the carrier dynamics $\xi_1(t)$ in the top SRR arm [carriers (1) and (3)] and the oscillations described by $\xi_2(t)$ in the bottom SRR arm [carriers (2) and (4)]. The physical origin of this coupling is, as for the metamolecules discussed before, the Coulomb interaction of carriers in the horizontal SRR arms excited by an electric field parallel to the arms and the carriers in the vertical arm that are excited by the local fields of the horizontally oscillating charges. This produces a current inside the entire SRR. With the carrier distribution (4.48) together with the oscillator equations (4.49,4.50) the macroscopic quantities [Eqs.(2.34,2.35,2.44)] can be obtained

$$
\mathbf{P}(\mathbf{r}, t) = \mathbf{e}_x \left\langle 2\eta q [\xi_1(t) + \xi_2(t)] \right\rangle + \mathbf{e}_y \left\langle \eta q [\xi_1(t) - \xi_2(t)] \right\rangle,
\tag{4.51}
$$

$$
\mathbf{M}(\mathbf{r}, t) = -\mathbf{e}_z \left\langle \frac{q\eta}{2}(x_0 + 2y_0)\frac{\partial}{\partial t}[\xi_1(t) - \xi_2(t)] \right\rangle,
\tag{4.52}
$$

$$
Q_{xy}(\mathbf{r}, t) = \left\langle \frac{q\eta}{2}[\xi_1(t) - \xi_2(t)]\left\{(2y_0 - x_0) - [\xi_1(t) + \xi_2(t)]\right\} \right\rangle.
\tag{4.53}
$$

Regarding Eqs.(4.51,4.52,4.53) the first- and second-order moments are depending on the sum $\xi_1(t) + \xi_2(t)$ and the difference $\xi_1(t) - \xi_2(t)$. The first-order electric dipole moment causes a polarization in $x$- and in $y$-direction. For a symmetric carrier oscillation, i.e., $\xi_1(t) = \xi_2(t)$, only an electric dipole moment in $x$-direction will be induced, whereas the dipole moment in $y$-direction vanishes. In turn, a perfectly anti-symmetric oscillation mode, i.e., $\xi_2(t) = -\xi_1(t)$ causes the vanishing of the electric dipole moment in $x$-direction, while the electric dipole moment in $y$-direction is maximized. In addition to the first-order multipole response all

second-order multipole moments are non-zero for a non-symmetric oscillation, i.e., $\xi_1(t) \neq \xi_2(t)$, only. With these properties, the numerically observed dynamics for mode 1 and mode 2 in Fig.4.7(C) can be modeled by the proposed microscopic carrier arrangement.

As it has been initially motivated, the electric quadrupole tensor (4.53) comprises contributions that are proportional to the product of two carrier elongations, here $\propto [\xi_1(t) - \xi_2(t)][\xi_1(t) + \xi_2(t)]$. In the next step, it will be shown that exactly this moment causes a quadratic nonlinear source term, since both $\xi_1(t) + \xi_2(t)$ and $\xi_1(t) - \xi_2(t)$ are proportional to the electric field[10]. Hence, the macroscopic electric field ansatz

$$E_x(\mathbf{r}, t) = \langle \mathfrak{E}_x(\mathbf{r}, t) \rangle = E_\omega e^{i(k(\omega)y - \omega t)} + E_{2\omega} e^{i(k(2\omega)y - 2\omega t)} + \text{c.c.}, \tag{4.54}$$

has been selected. In Eq.(4.54) $E_\omega$ and $E_{2\omega}$ correspond to the macroscopic electric field amplitudes for the fundamental (FF) and the second harmonic (SH) frequency, respectively. This field decomposition will be used to describe the second harmonic generation (SHG) [Boy92], which will be investigated later on. Solving Eqs.(4.48,4.49) upon temporal Fourier transformation (2.51) yields for the before-mentioned electric field ansatz

$$\left\langle \xi_1(t) \pm \xi_2(t) \right\rangle = \xi_\omega^\pm E_\omega e^{i[k(\omega)y - \omega t]} + \xi_{2\omega}^\pm E_{2\omega} e^{i[k(2\omega)y - 2\omega t]} + \text{c.c.}, \tag{4.55}$$

where the amplitudes are given by

$$\xi_\omega^+ = 2\chi_\omega^+ \cos[k(\omega)y_0], \tag{4.56}$$

$$\xi_\omega^- = 2i\chi_\omega^- \sin[k(\omega)y_0], \qquad \text{with } \chi_\omega^\pm = -\frac{q}{m} \frac{1}{\omega_0^2 - \omega^2 - i\gamma\omega \pm \sigma}. \tag{4.57}$$

With the knowledge about the carrier dynamics (4.55) together with Eqs.(4.51,4.52,4.53) the wave equation (4.7) incorporating multipolar contributions up to second order can be evaluated. A separation of the wave equation into two parts yields for the FF

$$\left\{ \frac{\partial^2}{\partial y^2} + \frac{\omega^2}{c^2} + \omega^2 \mu_0 p_\omega - \mu_0 \left[ \omega^2 q_\omega - i\omega m_\omega \right] \frac{\partial}{\partial y} \right\} E_\omega e^{ik(\omega)y} =$$
$$-\omega^2 \mu_0 q_{\omega;2\omega,-\omega} \frac{\partial}{\partial y} \left\{ E_\omega^* E_{2\omega} e^{i[k(2\omega) - k(\omega)^*]y} \right\}, \tag{4.58}$$

and the SH [11]

$$\left\{ \frac{\partial^2}{\partial y^2} + \frac{4\omega^2}{c^2} + 4\omega^2 \mu_0 p_{2\omega} - \mu_0 \left[ 4\omega^2 q_{2\omega} - 2i\omega m_{2\omega} \right] \frac{\partial}{\partial y} \right\} E_{2\omega} e^{ik(2\omega)y} =$$
$$-4\omega^2 \mu_0 q_{2\omega;\omega,\omega} \frac{\partial}{\partial y} \left[ E_\omega^2 e^{i2k(\omega)y} \right]. \tag{4.59}$$

In Eqs.(4.58,4.59) the following abbreviations for the linear terms[12], i.e., the linear parts of

---

[10]Such terms have been already observed for the planar SRR, see Eq.(4.28) in section 4.1.2, and for the CW, see Eq.(4.5) in section 4.1.1, but there these contributions are not radiating in propagation direction.

[11]The operator $*$ in Eq.(4.58) accounts for the complex conjugation.

[12]For the SH, the respective expressions are obtained by substituting $\omega$ by $2\omega$.

the multipole moments

$$p_\omega = 2\eta q \xi_\omega^+, \quad m_\omega = i\omega \frac{\eta q (2y_0 + x_0)}{2} \xi_\omega^-, \quad q_\omega = \frac{q\eta(2y_0 - x_0)}{2} \xi_\omega^-, \tag{4.60}$$

as well as for the nonlinear source terms

$$q_{\omega;2\omega,-\omega} = \frac{q\eta}{2} \left( \xi_\omega^- \xi_{2\omega}^{+*} - \xi_{2\omega}^- \xi_\omega^{+*} \right), \qquad q_{2\omega;\omega,\omega} = \frac{q\eta}{2} \xi_\omega^- \xi_\omega^+, \tag{4.61}$$

have been defined. The nonlinear set of equations (4.58,4.59), connecting the FF and the SH, is coupled by the nonlinear source terms (4.61). Considering the wave equation for the SH, one can derive that all appearing quantities are simultaneously present in the wave equation for the FF. These circumstances will allow to predict the nonlinear response solely on the basis of the linear optical material response.

In order to estimate the linear properties of a realistic SRR metamaterial with the developed formalism, the nonlinear source terms are firstly dropped. This is a standard procedure in nonlinear optics [Boy92] which is valid for weak interaction between FF and SH. This causes a decoupling of the SH and the FF wave equations and allows to evaluate the dispersion relation and the effective material properties. Secondly, the source terms will be included and the SHG will be described with the determined parameters from the linear regime.

At first, the linear properties are investigated in terms of the dispersion relation. Therefore the nonlinear source term on the right-hand side of Eq.(4.58) is set to zero. Equivalently, the same can be performed for the SH wave equation. As required, the result is the same equation as for the FF, but with $2\omega$ instead of $\omega$. The dispersion relation[13] for a linear propagation in $y$-direction becomes [PCT+09]

$$k^2(\omega) = \frac{\omega^2}{c^2} n_{\text{eff}}^2(\omega) = \frac{\omega^2}{c^2} \frac{1 + \frac{4\eta q}{\epsilon_0} \chi_\omega^+}{1 + \frac{\omega^2}{c^2} \frac{2\eta q}{\epsilon_0} y_0^2 \left[ \chi_\omega^+ - 2\chi_\omega^- \right]}. \tag{4.62}$$

In Eq.(4.62) the approximations for the trigonometric functions, see Eqs.(4.18) have been applied. In addition, the effective material parameters, i.e., the electric permittivity according to Eqs.(2.53,2.55)

$$\epsilon_{\text{eff}}(k, \omega) \equiv 1 + \frac{p_\omega}{\epsilon_0} - ik(\omega) \frac{q_\omega}{\epsilon_0}, \tag{4.63}$$

as well as the magnetic permeability [Eqs.(2.54,2.56)]

$$\mu_{\text{eff}}(k, \omega) \equiv \frac{1}{1 + m_\omega \frac{\mu_0 \omega}{k(\omega)}}, \tag{4.64}$$

can be derived. In analogy to the CW metamaterial in section 4.1.1, these parameters have been introduced for the fundamental mode approximation and are valid for a fixed propagation

---

[13]Frequently the refractive index $n_{\text{eff}}$ is applied to describe the propagation properties of metamaterials. But since this quantity is a derived quantity of the dispersion relation, see Eq.(4.62), here the propagation constant is considered as the fundamental parameter, describing the light propagation characteristics.
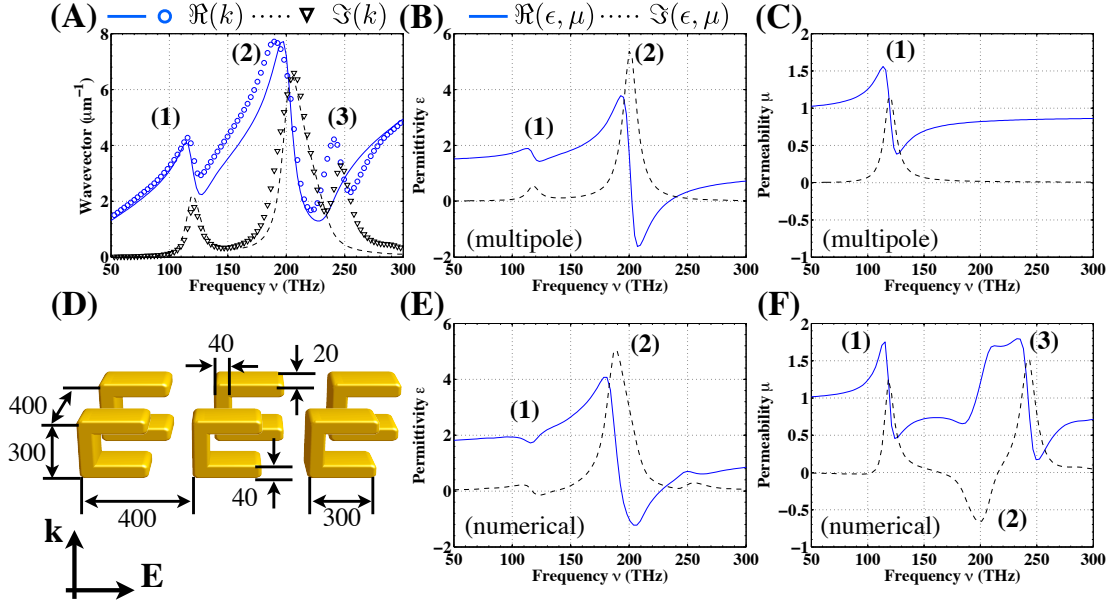
**Figure 4.7:** (A) The real and the imaginary part of the dispersion relation obtained numerically (circles, triangles) and analytically (solid and dashed lines). As it can be inferred, the analytical solution only reproduces the first two modes (1) and (2), while mode (3) is absent. The effective material properties (B) electric permittivity and (C) magnetic permeability obtained with the multipole description. The respective numerical values are shown in (E) and (F), respectively. (D) The dimensions and arrangement of the investigated SRR metamolecules. All dimensions are given in units of nm.

direction (along the $y$-axis), solely.

In order to evaluate the developed formalism, the dispersion relation as well as the effective material properties have been computed by FMM for a realistic SRR metamaterial. Results are presented in Fig.4.7. The geometry of the SRR metamolecules as well as the parameters of the lattice arrangement are shown in Fig.4.7(D). At first, the unknown oscillator parameters $\omega_0$, $\gamma$, $\sigma$, and $q^2\eta$ are determined by fitting the dispersion relation (4.62) to the numerical one[14]. Results are shown in Fig.4.7(A). The first two modes, denoted as (1) and (2), can be nicely reproduced by the multipole model, while the next higher-order mode (3) is not considered within the applied carrier ansatz. As it may be concluded from the numerical effective permeability this mode (3) corresponds to an effective magnetic mode as well. This mode comprises a similar anti-symmetric current distributions as mode (1), but with an oppositely directed current in the SRR base, not shown here.

With the parameters found by fitting the numerical with the analytical dispersion relation, the effective permittivity (4.63) and the magnetic permeability (4.64) can be computed without any further adaption, see 4.7(B,C). These parameters match the numerically retrieved parameters [SVKS05], shown in Fig.4.7(E,F). Similar to the CW metamaterial, the anti-resonance in the numerical calculations for the magnetic permeability is observed for resonance (2), i.e., the fundamental electric resonance, see [Fig.4.7(F)]. Summarizing the comparison between the multipole and the numerical modeling a good agreement can be achieved. For this purpose, the optical response in the multipole formalism is restricted to the two fundamental resonances,

---

[14]The fitting can be performed manually, since the effect of each parameter is quite distinct. Parameters can be found in [PCT+09]

i.e., the fundamental magnetic (1) and electric (2) modes, as initially adopted.

In the following, the nonlinear optical effects of these two fundamental LPP modes will be considered. Therefore the linear dispersion relation describing the wave propagation properties in the linear regime will be applied, while the nonlinearity will be treated as a perturbation rather than solving the nonlinearly coupled set of equations (4.58,4.59) exactly. The usually applied method for this procedure is the *slowly varying envelope approximation* (SVEA) [BC90, Boy92]. With this method the fast underlying oscillation $\propto \exp[ik(\omega)y]$ is separated from a slowly varying amplitude $A(y)$, which contains all information about the generation and depletion of the fundamental ($E_\omega = A_\omega(y)\exp[ik(\omega)y]$) and the second-harmonic ($E_{2\omega} = A_{2\omega}(y)\exp[ik(2\omega)y]$). Prior to plugging the SVEA ansatz into the complete set of equations (4.58,4.59) the following substitutions are performed for conveniance

$$\delta_\omega \;\equiv\; \frac{\omega^2}{c^2} + \omega^2\mu_0 p_\omega, \tag{4.65}$$

$$\beta_\omega \;\equiv\; \mu_0\left(\omega^2 q_\omega - i\omega m_\omega\right), \tag{4.66}$$

$$\psi_{\omega;2\omega,-\omega} \;\equiv\; \omega^2\mu_0 q_{\omega;2\omega,-\omega}, \tag{4.67}$$

$$\psi_{2\omega;\omega,\omega} \;\equiv\; 4\omega^2\mu_0 q_{2\omega;\omega,\omega}. \tag{4.68}$$

The set of equations (4.58,4.59) simplifies upon substituting Eqs.(4.65-4.68)

$$\left\{\frac{\partial^2}{\partial y^2} + \delta_\omega - \beta_\omega\frac{\partial}{\partial y}\right\}E_\omega e^{ik(\omega)y} \;=\; -\psi_{\omega;2\omega,-\omega}\frac{\partial}{\partial y}\left\{E_\omega^* E_{2\omega}e^{i[k(2\omega)-k(\omega)^*]y}\right\}, \tag{4.69}$$

$$\left\{\frac{\partial^2}{\partial y^2} + \delta_{2\omega} - \beta_{2\omega}\frac{\partial}{\partial y}\right\}E_{2\omega} e^{ik(2\omega)y} \;=\; -\psi_{2\omega;\omega,\omega}\frac{\partial}{\partial y}\left[E_\omega^2 e^{i2k(\omega)y}\right]. \tag{4.70}$$

Afterwards, the application of the SVEA ansatz to Eqs.(4.69,4.70) yields

$$\frac{\partial}{\partial y}A_\omega(y) \;=\; -\frac{\psi_{\omega;2\omega,-\omega}}{2ik(\omega)-\beta_\omega}\left\{A_{2\omega}(y)\frac{\partial}{\partial y}A_\omega(y)^* + A_\omega(y)^*\frac{\partial}{\partial y}A_{2\omega}(y) + i[k(2\omega)\right.$$
$$\left. -k^*(\omega)]A_\omega(y)^* A_{2\omega}(y)\right\}e^{i[k(2\omega)-k(\omega)^*-k(\omega)]y}, \tag{4.71}$$

$$\frac{\partial}{\partial y}A_{2\omega}(y) \;=\; -\frac{\psi_{2\omega;\omega,\omega}}{2ik(2\omega)-\beta_{2\omega}}\left[2A_\omega(y)\frac{\partial}{\partial y}A_\omega(y) + 2ik(\omega)A_\omega^2(y)\right]e^{i[2k(\omega)-k(2\omega)]y}. \tag{4.72}$$

Now, the set of equations (4.71,4.72) can be solved by standard routines. For this purpose, the ordinary differential equation solver `ODE45solve`, embedded in `MATLAB`, has been applied [SR97]. In order to describe the generation of the SH, the two initial values $A_\omega(0) = 1$ and $A_{2\omega}(0) = 0$ together with the dispersion relation with the underlying parameters from the linear response have been applied. Results are shown in Fig.4.8(A,B). For the evolution of the FF in Fig.4.8(A) a strong damping according to the increased imaginary part around resonances (1) and (2) is observed. Spectrally separated from these resonances, the FF propagates almost without losses, as intuitively expected. In turn, the SH is generated exactly at both resonance positions. In detail, the signal from resonance (1) is much stronger damped in comparison to the signal from resonance (2). The strong damping of the generated SH

**(A)** $|E_\omega|^2$ (normalized)

**(B)** $|E_{2\omega}|^2/|E_\omega|^2$

$\blacksquare$ $\Re[k_y(\omega)]$ $\cdots\cdots$ $\Im[k_y(\omega)]$

**(C)** UDPA $|E_\omega|^2$ (normalized)

**(D)** UDPA $|E_{2\omega}|^2/|E_\omega|^2$
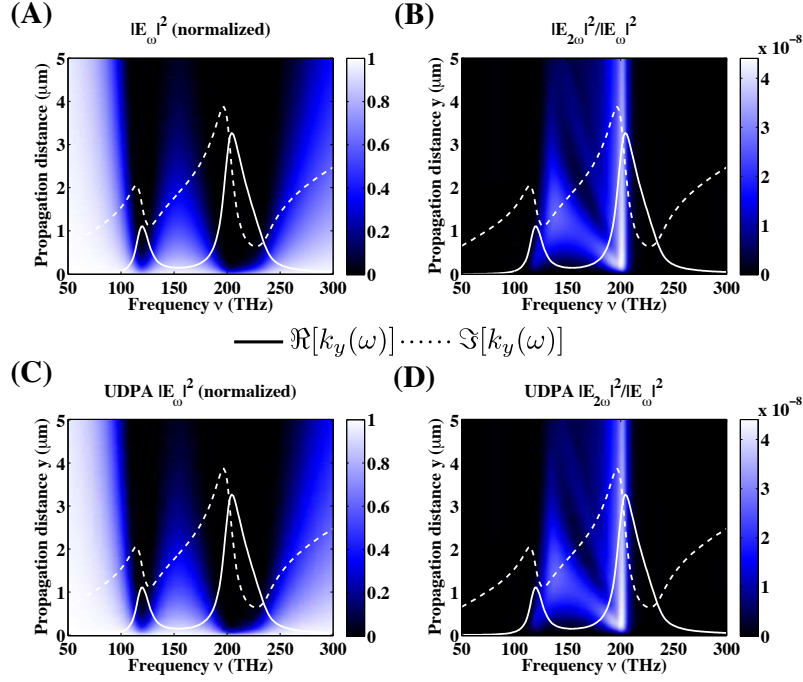
**Figure 4.8:** Numerical results for the evaluation of the normalized intensities $\propto |E|^2$ of the (A) FF and (B) the SH. The respective results are shown for the undepleted pump approximation in (C) and (D), respectively. In addition, the real (dashed line) and the imaginary part (solid line) of the dispersion relation are presented. It can be observed that the FF is damped at the resonances in the dispersion relation, while the generated SH is confined exactly to the two fundamental LPP resonances.

for resonance (1) can be easily explained. The SH generated by mode (1), propagates at the doubled frequency, i.e., at $\approx 220$ THz. At this frequency an enhanced imaginary part due to the presence of resonance (2) is still present, see Fig.4.8(A,B). Contrarily, the SH generated by mode (2) propagates at $\approx 400$ THz where the imaginary part is almost zero due to the absence of any further resonances. Thus, the SH for mode (1) appears to be much weaker than the respective SH from mode (1).

However, the overall conversion efficiency from FF to SH, i.e., $|E_{2\omega}|^2/|E_\omega|^2 \approx 10^{-8}$ is rather weak. Hence, the influence of the SHG on the fundamental can be neglected. This assumption is known as the *undepleted pump approximation* (UDPA) [Boy92, BC90] and can be expressed by the dropping of all spatial derivatives acting on $A_\omega(y)$. With this approximation and the before-mentioned initial value $A_{2\omega}(0) = 0$, Eq.(4.72) can be directly integrated

$$\frac{\partial}{\partial y} A_{2\omega}(y) = -\frac{\psi_{2\omega;\omega,\omega}}{2ik(2\omega) - \beta_{2\omega}} \left[ 2ik(\omega) A_\omega^2(y) \right] e^{i[2k(\omega) - k(2\omega)]y}, \tag{4.73}$$

$$A_{2\omega}(y) = \frac{\psi_{2\omega;\omega,\omega}}{2ik(2\omega) - \beta_{2\omega}} \frac{2k(\omega)}{2k(\omega) - k(2\omega)} A_\omega^2(y) \left\{ 1 - e^{i[2k(\omega) - k(2\omega)y]} \right\}. \tag{4.74}$$

If the undepleted pump approximation, i.e., Eq.(4.74), is applied to calculate $E_\omega(y)$ and $E_{2\omega}(y)$, as shown in Fig.4.8(C,D), one observes almost exactly the same results as for the numerical computation. The agreement between the numerical results and the UDPA calculations can be considered as a proof for the validity of the applied approximations as well as a check for the numerical simulations. Furthermore, the UDPA formalism in form of Eq.(4.73)

may be applied to introduce an effective quadratic nonlinear susceptibility tensor $\chi_{\text{eff}}^{(2)}(2\omega; \omega, \omega)$ [Boy92] for the SRR metamaterial investigated here

$$\chi_{\text{eff}}^{(2)}(2\omega; \omega, \omega) = \frac{4q_{2\omega;\omega,\omega} k(\omega) k(2\omega)}{\beta_{2\omega} - 2ik(2\omega)}. \tag{4.75}$$

With these final calculations the wave propagation in a quadratic nonlinear medium, where the nonlinearity arises due to multipolar moments, has been completed including the applied approximations. It has been shown that the required parameters to predict the nonlinear response can be determined by comparing any linear effective material response with the introduced multipole approach. Here, this has been achieved by a direct fitting of the analytical dispersion relation to a numerically calculated one. In general, this could have been similarly achieved by fitting to, e.g., the permittivity (4.63) or the permeability (4.64) as well. In contrast to section 4.1.2 the SRR metamolecules have been oriented uprightly, which causes that besides the electric dipole also second order moments are radiating.

Recently, the nonlinear optical response of SRR metamolecules has been subject of interest in its planar configuration [KWFL07, FLK⁺08]. In these works, a single layer of periodically arranged SRRs that have been oriented planar on the substrates was investigated. The observed SHG signal is expected to be much weaker, since only the electric field components parallel to the substrate interface contribute to the multipole nonlinearity. These components are typically included in the illumination as soon as a focussed illumination is applied, or the illumination is slightly tilted. Thus, the reported conversion efficiency of $|E_{2\omega}|^2/|E_\omega|^2 \approx 10^{-11}$ [FLK⁺08] is not contradicting with the results presented in this section. The single layer conversion efficiency for the SRR metamaterial investigated herein is $\approx 10^{-9}$. For an experimental proof and in order to further increase the measured SHG signal arising from second-order multipoles, an upright orientation of SRRs would be required. But in contrast to the planar orientation, the upright arrangement is a much more challenging task from the viewpoint of sample fabrication.

Summarizing this section, the linear response of metamaterials has been extended toward quadratic nonlinear optical effects. Most importantly, the appearance of second-order multipoles, being an essential ingredient in metamaterials, coincides with an additional nonlinear source. Thereby, the nonlinear optical properties are fully determined by the linear optical response. In the following section the nonlinear source term will be discussed in the framework of different existing and recently reported approaches applied for nonlinear studies involving metamaterials.

### 4.2.2 Comparison with other nonlinear approaches

As one of the most important references, *N. Bloembergen* the pioneer in nonlinear optics, mentioned the *quadrupolar nonlinearity* in his seminal work in 1965 [Blo65]. In this work *Bloembergen* considered the enhanced second harmonic signal observed by *Terhune et al.* [TMS62] who applied an additional electric DC (direct current) field to a calcite crystal with

inversion symmetry. The result of this additional field is a symmetry breaking which enhances quadratic nonlinear effects. These effects have been interpreted by a nonlinear effect that is induced by an additional quadrupole moment caused by the DC field. Moreover, *Bloembergen* mentioned in his book when writing down the averaged current density:

*...The volume averaged current density is usually expanded into a multipole series after the part due to convection currents has been splitt off*

$$\mathbf{J} = \mathbf{J}_{\text{cond}} + \frac{\partial}{\partial t}\mathbf{P} + c\nabla \times \mathbf{M} - \frac{\partial}{\partial t}(\nabla \cdot \hat{\mathbf{Q}}) + \ldots, \qquad \text{(CGS units)}, \qquad (4.76)$$

*...It is, nevertheless, a useful expansion if the volume can be divided into unit cells for which these moments can be calculated as successive approximations to* $\mathbf{J}$. *They all may contain nonlinear parts besides the linear parts...*[15]

Eq.(4.76) is very similar to Eq.(2.48) derived in section 2.1.1, but additionally with the electric dipole and quadrupole tensor considered in the current density as well. Since, the multipole moments can be either considered within the averaged current density or the electric displacement, as it has been described in section 2.1.1, this formulation is equivalent to the one applied in this work. Thus, it is indeed expected that as soon as second-order multipoles emerge, an additional quadratic nonlinear source term appears.

Finally, *Bloembergen* found that the quadrupole nonlinearity results in a nonlinear source term for the second harmonic according to [Blo65]

$$J_\alpha(2\omega) = 2i\omega \sum_{klm} \nabla_m \chi^{(2)}_{lkm\alpha} E_l(\omega) E_k(\omega). \qquad (4.77)$$

For a particular orientation, certain properties of the second-order nonlinear susceptibility tensor, and for linearly polarized light Eq.(4.77) can be simplified to

$$J_m(2\omega) = 2i\omega \chi^{(2)}_{\text{eff}}(2\omega; \omega, \omega) \sum_m \frac{\partial}{\partial r_m} \sum_{lk} E_l(\omega) E_k(\omega), \qquad (4.78)$$

$$J_x(2\omega) \equiv \psi_{2\omega;\omega,\omega} \frac{\partial}{\partial y}\left[E_x(\omega)\right]^2. \qquad (4.79)$$

Thus, for this particular case, the quadrupole source term exactly corresponds to the non-linear source term in Eq.(4.70). Hence, the multipole nonlinearity considered for the case of metamaterials in section 4.2.1 coincides with the one proposed by *Bloembergen*, as expected.

After recalling these historical issues an alternative procedure that has been recently applied to account for quadratic nonlinear effects in metamaterials will be compared to the multipole nonlinearity. This method is based on the *hydrodynamic theory of electrons* [FLK+08, ZHL+09] as it is typically applied in plasma physics [Fre07]. Taking into account both the electric and the magnetic field interactions in the Lorenz force (2.5) and taking into account a more sophisticated oscillator ansatz as it is described in [ZHL+09] yields the second order nonlinear

---

[15]In this section all cited equations have been written as they have been originally published for consistency.

source term

$$\frac{\partial}{\partial t}\mathbf{J}_{2\omega} = \epsilon_0\omega_{\mathrm{pl}}^2\mathbf{E}_{2\omega} - \omega_{\mathrm{coll}}\mathbf{J}_{2\omega} - \frac{\epsilon_0 e}{m}(\nabla \cdot \mathbf{E}_\omega)\mathbf{E}_\omega - \frac{e}{m}\mathbf{J}_\omega \times \mathbf{B}_\omega + \sum_{l=1}^{3}\frac{\partial}{\partial r_l}\frac{\mathbf{J}_\omega(J_\omega)_l}{e\eta}. \quad (4.80)$$

Besides the first two linear terms in Eq.(4.80) there are three nonlinear source terms. The third and the fourth[16] term account for the nonlinear contributions of the Lorenz force for the selected ansatz, while the last expression accounts for the *convective contribution*. This contribution is the result of local changes of electron momentum being induced by the external electric fields [FLK$^+$08]. *Feth et al.* investigated the effect of all these nonlinear contributions in nonlinear FDTD simulations, where they found that this last nonlinear source term is dominating over all others in Eq.(4.80) [FLK$^+$08].

In the following the last term in Eq.(4.80) will be considered in detail

$$\mathbf{J}_{2\omega} \quad \propto \quad \sum_{l=3}^{3}\frac{\partial}{\partial r_l}\frac{\mathbf{J}_\omega(J_\omega)_l}{e\eta}. \quad (4.81)$$

As it has been shown in the numerical simulations of the SRR in Fig.4.6(C), the SRR comprises currents in $x$- and $y$-direction, induced by an external electric field polarized in $x$-direction. Thus, one can substitute $(J_\omega)_x \propto (E_\omega)_x$ and $(J_\omega)_y \propto (E_\omega)_y$ in Eq.(4.81) which results in

$$(J_{2\omega})_x \quad \propto \quad \sum_{l=1}^{3}\frac{\partial}{\partial y}\Big[E_\omega\Big]^2, \quad (4.82)$$

and which is again mathematically equivalent to the nonlinear source term applied in Eq.(4.70) in the previous section. Hence, even though the nonlinear source terms predicted by the hydrodynamic electron model are physically different from the multipolar induced nonlinear effects, mathematically conform relations for the SHG could be obtained.

In conclusion, two methods have been shown to be consistent with the multipole nonlinearity, investigated in section 4.2.1. Thereby, the multipole approach has been shown to be conform with the quadrupolar nonlinearity predicted by *Bloembergen*. Secondly, the multipole nonlinearity provides mathematically the same nonlinear source terms as predictions from a hydrodynamic electron model that originates from a very different field of physics. Hence, all derivations performed in this chapter are not contradicting the other methods. Thus, the introduced formalism can be considered as an alternative way to understand and motivate the extraordinary intrinsic nonlinear properties of metamaterials from the viewpoint of simple electrodynamic considerations. As a very exceptional property of such a description, all nonlinear coefficients are directly accessible as soon as the linear response of the respective metamaterial has been described by the multipole method as well.

---

[16]The curl operator in the fourth term in reference [FLK$^+$08] is missing, but a correct version can be found in the detailed derivation, published later on [ZHL$^+$09].

## 4.3 Scattering patterns of isolated metamolecules

In this final chapter of part 4 the microscopic properties of isolated metamolecules will be considered in the framework of the multipole expansion. In contrast to the previous two sections, i.e., section 4.1 and 4.2, where macroscopic ensemble properties such as effective parameters or the dispersion relation have been determined, now the microscopic properties will be investigated. For this purpose, the near-field patterns of the SRR and the CW metamolecules will be investigated in this chapter. Thus, the near-fields of the respective metamolecule will be calculated and decomposed into their multipolar contributions up to the second order in the first section 4.3.1. With this technique it is possible to identify and quantify the impact of a particular multipolar contribution in the near-field patterns of an arbitrary metamolecule. Thereby, the connection between Mie theory and the multipole expansion series will be revealed. Lastly, in section 4.3.2 the influence of the required origin for the multipole expansion will be investigated. For simplicity, all these results are presented in two dimensions, but in general the introduced technique can be similarly extended toward three-dimensional metamolecules.

### 4.3.1 Multipole decomposition of the scattered field

Before the scattered fields of metamolecules will be decomposed into a combination of eigenfunctions of the free space, the general scattering properties of isolated two-dimensional objects will be briefly discussed. For this reason, apparently the most important analytical method in the field of nanoplasmonics, i.e., the *Mie theory* [Mie08] will be revisited. This method is one of the few rigorous methods that allows analytical calculations to exactly describe the light-matter interaction with particular types of scattering objects. Initially, the method has been introduced for spheres, but can be similarly applied to two-dimensional cylindrical scattering objects as well [BH83]. As it will be shown, the method makes use of a particular field expansion into a set of eigenfunctions. In the next step, it will be revealed how these eigenfunctions relate to the scattered field of multipole moments. This will finally allow to calculate the expansion coefficients that weight the impact of a particular eigenfunction, i.e., multipole expansion order. In the end, the introduced technique will be applied to calculate these expansion coefficients not for cylinders, but for two-dimensional metamolecules.

For the two-dimensional case the general three dimensional wave equation, e.g. Eq.(2.106), can be separated into two scalar equations for TE- and TM-polarization. Thus, for translational invariance in $z$-direction, the scalar wave equation in two dimensions can be found as [Jac75]

$$\Delta_{x,y} F_z(x,y) + k^2(\omega) F_z(x,y) = 0, \qquad \text{with } k^2(\omega) = \frac{\omega^2}{c^2}. \qquad (4.83)$$

In Eq.(4.83) $F_z(x,y)$ denotes the tangential component of either the electric field for TE (electric component out of plane) or the magnetic field for TM (magnetic component out of plane). For objects with cylindrical symmetry it is appropriate to transform Eq.(4.83) into cylindrical coordinates by substituting $x = R\cos(\phi)$ and $y = R\sin(\phi)$, with the radius

$R = \sqrt{x^2 + y^2}$. Thereby $\phi$ denotes the enclosed angle of the position vector with the $x$-axis. The wave equation (4.83) including these substitutions yields

$$\frac{1}{R}\frac{\partial}{\partial R}\left[R\frac{\partial}{\partial R}F_z(R,\phi)\right] + \frac{1}{R^2}\left[R\frac{\partial^2}{\partial\phi^2}F_z(R,\phi)\right] + k^2 F_z(R,\phi) = 0. \tag{4.84}$$

The resulting wave equation (4.84) corresponds to a Bessel-type differential equation, whose linearly independent solutions can be found as

$$F_z(R,\phi) = \sum_{m=-\infty}^{\infty} Z_m(kR)e^{-im\phi}. \tag{4.85}$$

In Eq.(4.85) the azimuthal part $Z_m(kR)$ can be represented by combinations of *Bessel functions* of the first kind $[J_m(kR)]$ and the second kind $[Y_m(kR)]$, while the angular dependence is described by an exponential function. Thus, any radiating field in a two-dimensional cylindrical basis that fulfills the *Sommerfeld radiation condition* [FM03] at infinity can be written as

$$F_{z,s}(R,\phi) = \sum_{m=-\infty}^{\infty} a_m i^m H_m^{(1)}(kR)e^{-im\phi}, \tag{4.86}$$

with $H_m^{(1)}(kR) = J_m(kR) + iY_m(kR)$ being the *Hankel functions* of the first kind and $a_m$ the expansion coefficients, termed Mie scattering coefficients of the respective expansion order $m$. With Eq.(4.86) any field outside a virtual cylinder that contains the entire scattering object can be described. This is possible, since the summation (4.86) is equivalent to a complete and orthogonal set of eigenfunctions weighted by the expansion coefficients $a_m$. Additionally, the scattered field in Eq.(4.86) always consists of two parts, i.e., the contributions from $m$ and $-m$. Hence, the scattered field $F_z(R,\phi)$ can be rewritten as

$$F_{z,s}(R,\phi) = \sum_{m=0}^{\infty}\left[a_m^+\psi_m^+(R,\phi,k) - a_m^-\psi_m^-(R,\phi,k)\right], \tag{4.87}$$

$$\psi_m^+(R,\phi,k) = i^m H_m^{(1)}(kR)\cos(m\phi), \tag{4.88}$$

$$\psi_m^-(R,\phi,k) = i^{m+1} H_m^{(1)}(kR)\sin(m\phi), \tag{4.89}$$

$$a_m^{\pm} = (a_m \pm a_{-m}), \tag{4.90}$$

taking advantage of the property $H_m^{(1)}(kR) = (-1)^m H_{-m}^{(1)}(kR)$, $\forall m \in \mathbb{Z}$ [AS72]. Now, Eq.(4.87) can be considered as a usual series expansion with respect to eigenfunctions of increasing order. These eigenfunctions $\psi_m^{\pm}(R,\phi,k)$ are simply products of radially and azimuthally varying functions. Regarding the azimuthal terms it can be seen from Eq.(4.87) that they split into two contributions that are $\pi/2$ phase-shifted indicated by the superscripts $\pm$. This is related to the fact that each expansion order is composed of two physically identical but azimuthally rotated contributions of order $m$. For realistic metamolecules the fundamental azimuthal part can be selected regarding the symmetries of the scattering ob-

**(A)** $|\psi_0(r, \phi, k)|$ **(B)** $|\psi_1^+(r, \phi, k)|$ **(C)** $|\psi_2^+(r, \phi, k)|$
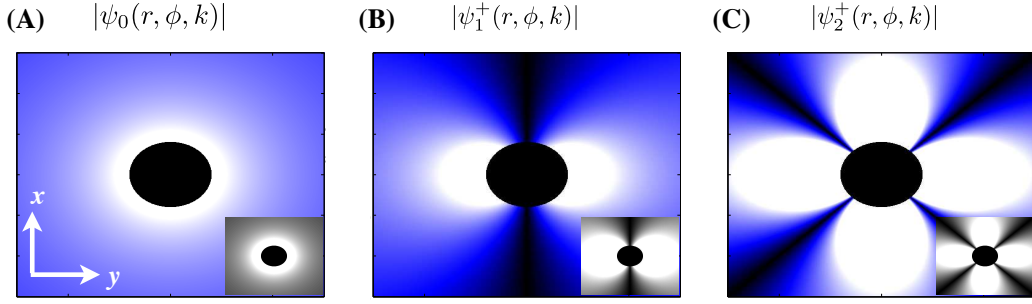
**Figure 4.9:** Evaluation of the eigenfunctions $|\psi_m^+(r, \phi, k)|$ for the first three orders, i.e., $m \in [0, 1, 2]$. (A) The eigenfunction for $m = 0$, (B) for $m = 1$, and (C) for $m = 2$. The insets show the magnetic field distribution $|B_z|$ for (A) the magnetic dipole moment, (B) electric dipole, and (C) the electric quadrupole moment. All moments are oriented in the $xy$-plane, as shown in Fig.2.3. The dark spot in the center of each plot is caused by the singularity of $\psi_m(0, \phi, k)$ as well as the multipole moments at the origin, see section 2.1.2.

ject; in general both linear independent contributions have to be considered for the respective order $m$. Having arrived at the final expansion, i.e., Eq.(4.87), the physics behind the underlying set of eigenfunctions has to be considered. As it may be deduced from Eqs.(4.88,4.89), they are related to Hankel functions of the first kind. However, it will be shown that each of these eigenfunctions can be assigned to a particular multipole order. To briefly motivate this, the eigenfunctions $\psi_{0,1,2}^+(R, \phi, k)$ have been evaluated and compared with the tangential magnetic fields $B_z(x, y)$ for the first- and second-order multipole moments in Fig.4.9. In order to calculate the respective fields for the multipole moments, the formalism derived in section 2.1.2 has been applied, i.e., Eqs.(2.58,2.67,2.74,2.78). For this comparison, primitive multipole moments have been assumed that are located in the $xy$-plane. The magnetic moment, see inset in Fig.4.9(A), can be associated to the eigenfunction of the order $m = 0$. Therefore, the underlying magnetic dipole moment has been induced by a ring current in the $xy$-plane, as it can be depicted from Fig.2.3 in section 2.1.2. For the computation of the electric dipole moment, as shown in the inset of Fig.4.9(B), a dipole oriented in $y$-direction has been applied. Finally, for the calculation of the electric quadrupole moment two oppositely directed electric dipoles have been assumed, as shown in Fig.2.3. The resulting magnetic fields are shown in the inset of Fig.4.9(C), which can be furthermore assigned to the eigenfunction of the order $m = 2$. In conclusion, an excellent qualitative agreement between the multipolar fields and the eigenfunctions applied in the series expansion (4.87) is obtained[17].

In the following, it will be shown that the qualitative agreement between $\psi_m^\pm(r, \phi, k)$ and the multipolar fields can be obtained rigorously as well. For this task, the three-dimensional multipolar fields have to be transformed into their two-dimensional representatives. Hence, the analytically found three-dimensional field components will be integrated along the $z$-axis.

---

[17]In contrast to the ordinary multipole expansion series, the second-order multipole moments, i.e., the electric quadrupole and magnetic dipole, are now discriminated by two different expansion orders ($m = 1$: magnetic dipole, and $m = 2$: electric quadrupole) in the series (4.87).

The vector potential for the electric dipole has been already derived in Eq.(2.67)

$$\mathbf{A}_{\mathrm{ED}}(\mathbf{r}, \omega) = -i\omega \frac{\mu_0}{4\pi} \frac{e^{ikr}}{r} \mathbf{p}.$$

The associated $z$-component of the magnetic field for an electric dipole moment in the $xy$-plane, i.e., $\mathbf{p} = p_x \mathbf{e}_x + p_y \mathbf{e}_y$, can be calculated with

$$\begin{aligned}
\mathbf{B}(\mathbf{r}, \omega) &= \nabla \times \mathbf{A}(\mathbf{r}, \omega), \\
B_{\mathrm{ED},z}(\mathbf{r}, \omega) &= -i\omega \frac{\mu_0}{4\pi} \frac{e^{ikr}}{r} \left[ p_y \left( iky - \frac{y}{r^2} \right) - p_x \left( ikx - \frac{x}{r^2} \right) \right].
\end{aligned} \tag{4.91}$$

The two-dimensional representation can be maintained by an integration along the $z$-axis of Eq.(4.91) which can be finally compared with Eq.(4.87) [PYM$^+$10, MP98]

$$\begin{aligned}
B_{\mathrm{ED},z}^{\mathrm{2D}}(x, y, \omega) &= \omega \frac{\mu_0 k}{4} \left[ \cos(\phi) p_x - \sin(\phi) p_y \right] H_1^{(1)}(kR) \tag{4.92} \\
&= H_1^{(1)}(kR) \left[ i a_1^+ \cos(\phi) - i^2 a_1^- \sin(\phi) \right], \tag{4.93} \\
a_1^+ &\equiv -i \frac{\omega \mu_0}{4} p_x, \qquad a_1^- \equiv -\frac{\omega \mu_0}{4} p_y. \tag{4.94}
\end{aligned}$$

Considering Eqs.(4.92-4.94), the connection between the electric dipole moment and the eigenfunctions $\psi_1^\pm(R, \phi, k)$ can be directly inferred. Thus, the electric dipole moments oriented along the $x$- and $y$-direction are proportional to the expansion coefficients $a_1^+$ and $a_1^-$, respectively. Strictly speaking, the expansion (4.87) for $m = 1$ can be physically interpreted by a decomposition into the fields of two electric dipole moments rotated by 90° ($\phi = \pi/2$). Very similar, this can be performed for the magnetic dipole ($m = 0$) and the electric quadrupole moment ($m = 2$) as well. Upon such an analysis, each multipole order can be related to a certain expansion coefficient $a_m^\pm$ [PYM$^+$10].

Having explored the physical background of the expansion, the remaining task is to calculate the expansion coefficients $a_m^\pm$ for arbitrary metamolecules. The knowledge about the determined coefficients will directly allow to quantify the participating multipole moments. As usual the expansion coefficients are calculated by evaluating the overlap integral between the respective eigenstate and the field distribution under consideration

$$a_m^\pm = \frac{\int_0^{2\pi} d\phi \int_{R_1}^{R_2} dR R F_z(R, \phi) \psi_m^{\pm *}(R, \phi, k)}{\int_0^{2\pi} d\phi \int_{R_1}^{R_2} dR R |\psi_m^\pm(R, \phi, k)|^2}. \tag{4.95}$$

With Eq.(4.95) it is possible to rigorously calculate the expansion coefficients $a_m^\pm$ for a given field distribution $F_z(R, \phi)$ on an annulus with the two radii $R_2$ and $R_1$. Beneficial for any calculations is the orthogonality of both the angular and the radial part of the overlap integration (4.95). Hence, it is enough to perform the overlap integration for a ring, rather than for the entire cross section. To prove the orthogonality, one can substitute $F_z(R, \phi)$ by a particular
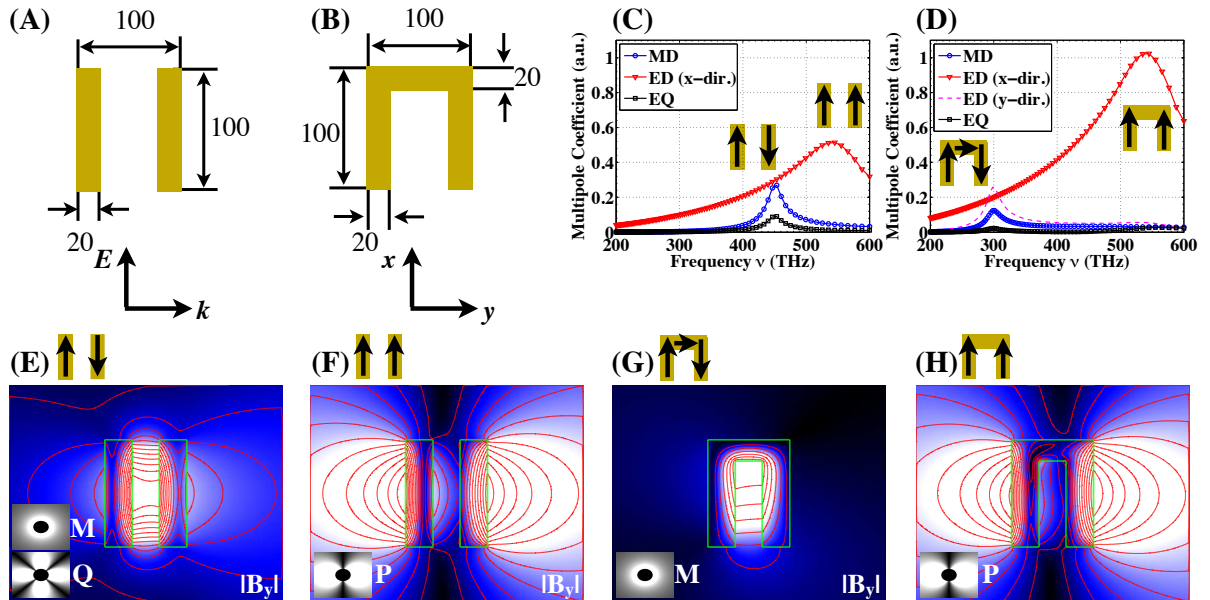
**Figure 4.10:** The illumination conditions, the orientation, and the definition of the geometrical parameters of (A) the CW and (B) the SRR metamolecule. The calculated Mie expansion coefficients ($a_m$), related to the magnetic dipole (MD), the electric dipole (ED) and the electric quadrupole (EQ) for (C) the CW and (D) the SRR metamolecule. Finally, the scattered magnetic fields for (E) the *magnetic* and (F) the *electric* resonance of the CW and the SRR in (G,H) are shown, respectively. The gray-scaled insets show the exact multipole magnetic field distributions as in Fig.4.9 to underline the similarities to the exact scattering field patterns.

eigenfunction of the order $l$, e.g., $\psi_l^+(R, \phi, k)$ according to Eq.(4.87), which yields[18]

$$\frac{\int_0^{2\pi} d\phi \int_{R_1}^{R_2} dRR\psi_l^+(R, \phi, k)\psi_m^{+*}(R, \phi, k)}{\int_0^{2\pi} d\phi \int_{R_1}^{R_2} dRR|\psi_m^+(R, \phi, k)|^2}$$
$$= \frac{\int_{R_1}^{R_2} dRRH_l^{(1)}(R, k)H_m^{(1)}(R, k)}{\int_0^{2\pi} d\phi \int_{R_1}^{R_2} dRR|\psi_m^+(R, \phi, k)|^2}i^{l-m}\int_0^{2\pi} d\phi\left[\cos(l\phi)\cos(m\phi)\right] = \delta_{ml}. \quad (4.96)$$

Thus, it is sufficient to evaluate the overlap integral at a fixed value of $R$ rather than on the annulus to obtain $a_m^\pm$. However, performing the integration on an annulus may be advantageous compared to the ring integration. The reason for this is that the numerical (or experimental) data for $F_z(R, \phi)$ is typically given on a discrete mesh. In general, this mesh is not aligned with the cylinder aligned around the scattering object and an appropriate interpolation may be required. Although a sufficiently fine grid improves the numerical stability of the ring integration, this issue can be circumvented if the annulus integration is performed.

Lastly, the developed formalism to retrieve the multipolar contributions will be applied for two metamolecules of interest, namely the CW and the SRR. The dimensions of both metamolecules are given in Fig.4.10(A,B).

---

[18]In Eq.(4.96) the overlap integration has been performed for the "+" (cosine) case. The overlap between the eigenfunctions $\psi_l^+$ and $\psi_m^-$ yields an additional $\delta_\pm$, due to the orthogonality of the sine and cosine functions.

Since LPP resonances in the metamolecules can only be excited for TM polarization the magnetic fields $B_z(x,y)$, representing $F_z(R,\phi)$ have been calculated numerically with `COMSOL` [COM10]. Rather than determining the multipolar contributions in the scattering patterns for a single frequency, the fields have been calculated over a frequency interval. This allows to compare and to visualize the different multipole contributions that are selectively excited for the characteristic resonance frequencies of LPP modes for the respective metamolecule, as described in the previous chapters.

For the CW metamolecule two resonances are obtained, indicated by the two peaks in Fig.4.10(C). The low-frequency resonance is dedicated to the magnetic, i.e., anti-symmetric, mode while the high-frequency resonance stems from the excitation of the electric, i.e., symmetric, mode. As expected from section 4.1.1, the anti-symmetric mode, indicated by the facing currents in the inset of Fig.4.10(C), coincides with the excitation of second-order multipoles. Consequently, the respective expansion coefficients $a_0$ and $a_2$ are dominating over the fundamental electric dipole moment $(a_1)$. In turn, the electric dipole moment has a clear maximum for the symmetric resonance, while second order multipoles are almost vanishing. A similar behavior can be observed for the SRR metamolecule in Fig.4.10(D). In addition to the CW structure, the SRR comprises a connecting wire in between. As it has been found in section 4.2.1, this wire results in an electric dipole moment in propagation direction for the anti-symmetric mode. Besides this additional electric dipole moment, the scattering response for the anti-symmetric mode is dominated by second-order multipoles. A closer examination shows that the electric quadrupole moment has an almost vanishing magnitude when compared with the magnetic dipole moment. This is different to the CW metamolecule where both the magnetic dipole moment and the electric quadrupole provide strong contributions. For the symmetric mode, analogously to the CW metamolecule, the optical response is dictated by the in-line excitation of the electric dipoles in the $x$-directed SRR arms.

In order to further illustrate the multipolar response of both metamolecules, the field patterns of the CW and the SRR are presented for the magnetic and the electric resonance positions in Fig.4.10(E-H). The magnetic fields at the electric resonance for both metamolecules are nicely described by the corresponding fields of an electric dipole, as shown in the gray-scaled insets in Fig.4.10(F,H), respectively. For the magnetic resonance, the fields of the CW metamolecule indicate a much stronger contribution from the electric quadrupole, see Fig.4.10(A). In turn, the SRR field distribution at the magnetic resonance seems to be dominated by the fields of a magnetic dipole, see Fig.4.10(G), which is consistent with the interpretation of Fig.4.10(C,D) from above.

In conclusion, a rigorous method has been presented to reveal the multipolar contributions in the scattering patterns of arbitrary metamolecules. In contrast to the multipole properties of an ensemble of metamolecules, this method is useful to investigate isolated metamolecules. With the developed formalism one can immediately determine the electric and magnetic properties of the isolated object. Hence, this method might be a suitable tool to determine electromagnetic properties of isolated metamolecules and provide a tool to tune the optical response of a metamolecule for a desired effect, e.g., to enhance the magnetic dipole

moment, etc. In addition, the connection between Mie theory and the multipole approach has been presented, where the multipole moments can be directly related to the eigensolutions of the two-dimensional wave equation.

### 4.3.2 Origin dependence for the multipole expansion

In this final section, the dependence on the origin for the applied multipole expansion, presented in the previous section 4.3.2 will be investigated. A general statement considering the origin dependence has been given by *R. E. Raab* and *O. L. de Lange*: *"...only the leading non-vanishing electric multipole moment is independent of the origin..."* [dLR05]. As an illustration for this property the electric quadrupole can be considered upon a spatial displacement according to $\bar{\mathbf{r}} = \mathbf{r} - \mathbf{d}$. Substituting this displacement into the molecular electric quadrupole moment (2.29) yields

$$
\begin{aligned}
(\bar{Q}_m)_{\alpha\beta} &= 3 \sum_{b(m)=1}^{N_{\text{bound}}} q_{b(m)} [r_{b(m)} - d_{b(m)}]_\alpha [r_{b(m)} - d_{b(m)}]_\beta \\
&= 3 \sum_{b(m)=1}^{N_{\text{bound}}} \left\{ q_{b(m)} [r_{b(m)}]_\alpha [r_{b(m)}]_\beta - q_{b(m)} [r_{b(m)}]_\alpha [d_{b(m)}]_\beta - q_{b(m)} [r_{b(m)}]_\beta [d_{b(m)}]_\alpha \right. \\
&\quad \left. + q_{b(m)} [d_{b(m)}]_\alpha [d_{b(m)}]_\beta \right\} \qquad \text{[substituting Eqs.(2.27,2.28)]} \\
&= (Q_m)_{\alpha\beta} - 3[p_m]_\alpha [d_{b(m)}]_\beta - 3[p_m]_\beta [d_{b(m)}]_\alpha + 3\tilde{q}_m [d_{b(m)}]_\alpha [d_{b(m)}]_\beta. \qquad (4.97)
\end{aligned}
$$

Hence, the electric quadrupole moment in Eq.(4.97) is independent of the origin $[(Q_m)_{\alpha\beta} = (\tilde{Q}_m)_{\alpha\beta}]$, if the total charge $\tilde{q}_m$ and the molecular electric dipole moment $p_m$ are vanishing. Thus, since all metamolecules investigated throughout this work are considered to be neutrally charged, the total charge can be safely neglected, i.e., $\tilde{q}_m = 0$. In turn, the electric dipole moment has a strong contribution in all metamolecules and in particular in the metamaterials investigated in the previous section 4.3.1, i.e., Fig.4.10(C,D). Consequently, the electric dipole moment should be independent of the origin of the expansion. In order to prove this issue, the center of the annulus for the overlap integration, i.e., Eq.(4.95) has been varied. The only restriction for such a variation is that the annulus entirely contains the metamolecule. The center positions of each annulus for the overlap integration with respect to the SRR metamolecule are shown in Fig.4.11(A). As it can be depicted, both second order multipole moments, i.e., the magnetic dipole [Fig.4.11(B)] and the electric quadrupole moment [Fig.4.11(D)] are clearly dependent on the choice of the origin. In turn, the electric dipole moment remains invariant upon all manipulations on the origin position. It can be concluded that the electric dipole moment is independent of the choice of the expansion origin and thus behaves as expected from above.

With the performed analysis, an important property regarding the multipole expansion has been revealed for the case of metamaterials, which concludes this chapter.
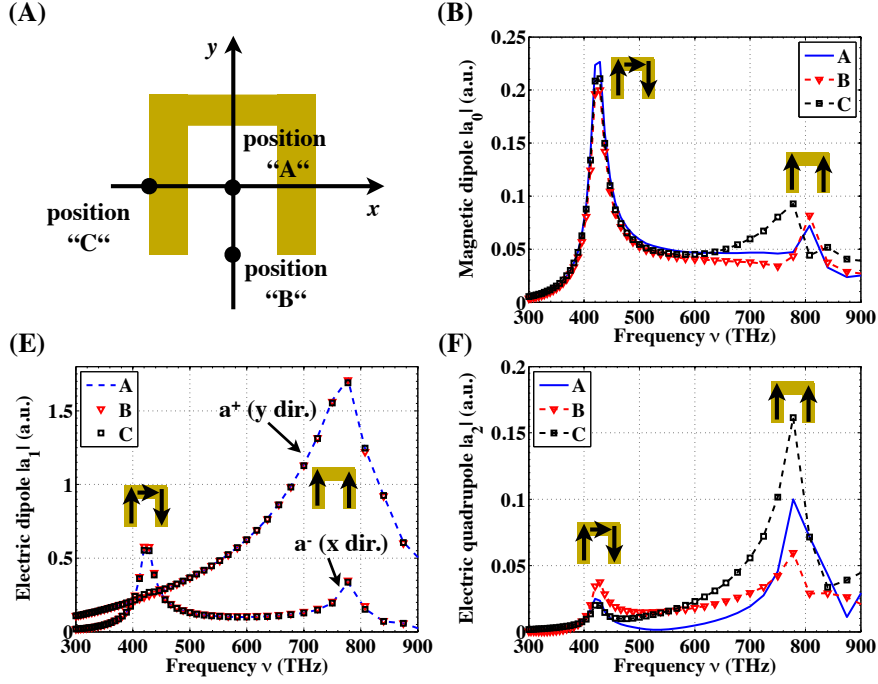
**Figure 4.11:** (A) The three investigated center positions for the annulus relative to the SRR meta-molecule under investigation. The retrieved expansion coefficients for (A) the magnetic dipole moment ($m = 0$), (C) the electric dipole moment ($m = 1$), and (D) the electric quadrupole moment ($m = 2$). As it can be depicted only the electric dipole, is inert against variations of the origin for the expansion series, which corresponds to the expected behavior for the leading multipole moment.

In summary of part 4, the concept of the multipole properties, as it has been known and widely applied for the case of electric dipole-type metamolecules, i.e., nanoantennas, etc., has been extended toward the description of more complex metamolecules. Therefore, second-order multipoles have been taken into account in order to describe effects such as optical magnetism, effective material properties, multipole-induced nonlinearity, as well as scattering properties of isolated metamolecules.

The major achievement in order to describe ensembles of metamolecules, i.e., metamaterials, is that the complex currents in the metamolecules can be represented by an appropriate carrier configuration. With such a procedure the multipole moments can be calculated and compared with experimental or numerical accessible quantities. As an example, this has been firstly performed for the CW metamolecule [PMC+08]. In the same manner the linear response of the SRR metamaterial can be described, whereas the second-order multipole response inherently induces quadratic nonlinear optical effects [PCT+09]. Thereby, the prediction of the nonlinear response can be completely performed on the basis of the parameters known from the linear material response, which is a first application of the method. A second possibility to apply the parameters that have been found for a particular metamolecule is to perform substantial geometrical modifications on the metamolecule. By considering these changes in the oscillator models, the optical response of modified metamolecules can be predicted as well. Therefore, modifications that change the character of the polarization eigenstates from linear to elliptical, have been investigated, whereas the optical response could be successfully predicted [PCT+10].

Since up to this point only ensemble, i.e., averaged or macroscopic, properties have been in-

vestigated, the microscopic response of isolated metamolecules has been the subject of the last chapter of this part. Thereby, the role of multipolar excitations within the scattering patterns of the metamolecules has been rigorously proven [PYM+10]. For this purpose metamolecules have been considered that were investigated in ensemble arrangements before. With this proposed method the individual strength of a certain multipole could be quantified, which verifies and finally reveals the presence of multipolar excitations in the considered metamaterials.

# 5 Summary and perspective

## Summary

The major focus of this work was devoted to the investigation of first- and second-order multipolar excitations in metal nanostructures. Hence, the investigation of the complex optical response of metal nanostructures that typically requires a three-dimensional, full-vectorial, numerical description including the material dispersion was performed in terms of the multipole expansion. Moreover, a microscopic model on the basis of coupled harmonic oscillators has been introduced to treat the carrier dynamics in complex metal nanostructures. This procedure is similar to the treatment of carriers and atoms in crystal lattices in solid state physics by simply considering the mutual interplay in terms of coupled oscillators to determine the dispersion relation of the lattice oscillations [Kit95]. This description allows for a simplified but intuitive microscopic understanding of localized plasmon-polariton resonances in terms of the oscillation eigenmodes of the coupled oscillator system. Upon excitation, the microscopic dynamics can be translated into macroscopic quantities, such as the polarization, the magnetization as well as the quadrupole density. Finally, this allows to describe the wave propagation inside such materials in a very consistent manner since the role of microscopic excitations can be directly related to the macroscopic response in terms of reflection and transmission coefficients as well as the effective material properties or the dispersion relation.

The advantage of such a modeling is that the multipole expansion can be applied for this carrier model. This allows for a physically thorough understanding and a simplification of the modeling by analytical calculations. Thus, in this work it has been shown, how textbook electrodynamics can be applied and modified to develop a qualitative and quantitative description of nanostructures.

Consequently, this work started by revisiting the electrodynamic principles of the multipole expansion as well as the rigorous numerical techniques that are required for an exact modeling. The most important result of this part is the understanding of the role of multipolar excitations in the transition from microscopic to macroscopic Maxwell's equations. These initial considerations allowed the application of the multipole expansion to describe metamaterials as effective materials with properties that are determined by the multipolar contributions of its intrinsic building blocks, i.e., the metamolecules. Secondly, it allowed to get a clear picture of the near-field properties of isolated metamolecules. In the next two parts of this thesis, both properties, i.e., the near-fields of isolated metamolecules as well as the effective material properties of ensembles, have been successively investigated for particular metamolecules exposing particular multipolar orders.

In the next part of this thesis, nanostructures exhibiting the first order, i.e., the electric dipole, mode were investigated. These nanostructures, or similarly termed nanoantennas, have been the result of a precise design with the aim to achieve several near-field enhancing features. For this purpose, arrays of rhomb-shaped nanoantennas have been developed

that simultaneously exhibit an off-resonant enhancement due to the lightning rod effect and a resonant enhancement due to the excitation of localized and propagating surface plasmon-polaritons. The propagating surface plasmon-polaritons take explicit advantage of the periodic arrangement and the dipolar properties of the isolated nanoantennas forming a metamaterial in the electric dipole limit. A simple description on the basis of the dipolar response of the nanoantennas and the transverse wavevector induced by the lattice allowed to describe the spectral behavior of the localized and the propagating plasmon-polaritons in consistency with the rigorous description. Moreover, experimental measurements of the far-field intensities of the fabricated samples agreed well with the rigorous numerical simulations and verified the theoretically predicted effects. Finally, the near-field enhancement of the doubly resonant nanoantenna arrays has been applied to measure the scattered Raman signals of the adsorbed crystal violet analyte. As a result, enhanced signals have been recorded due to the simultaneous presence of the resonant field enhancement at the excitation and the shifted Raman frequency by the two before-mentioned plasmonic excitations. The enhancement provided by the lightning rod effect could be measured on the basis on the polarization dependence of the excitation of the plasmonic resonances. But as expected, it is much weaker than for the resonant plasmon-polaritons. Furthermore, the polarization dependence of the Raman scattering could be used to illustrate the underlying physics of the enhancement process, i.e., the excitation of dipolar and localized surface plasmon-polaritons.

In the last part of this thesis, metamolecules possessing second-order multipole moments have been considered. Firstly, an oscillator model has been developed for a simplified analytical description of the inner carrier dynamics of a particular metamolecule, i.e., the cut-wire pairs. With the knowledge about these dynamics, the multipole moments associated with each metamolecule could be calculated and transformed into macroscopic quantities, such as the dispersion relation or the associated electric permittivity and magnetic permeability. For this purpose, the multipole model could be used to reproduce the numerically obtained effective parameters as well as the dispersion relation. Thus, the entire response could be described by the excitation of first- and second-order multipoles. In the following the effects due to a change in the polarization eigenstates from linear toward elliptical have been investigated by the same approach. Therefore the reflection and transmission coefficients of the split-ring resonator metamaterial have been described with the oscillator and multipole formalism. This matamaterial has linearly polarized eigenstates and again the effective parameters as well as the spectral reflection and transmission coefficients predicted numerically could be nicely reproduced with the multipole model. Now, particular modifications on the metamolecule were performed which led to a change in the polarization eigenstates from linear to elliptical. By simultaneously considering these changes in the oscillator model, it could be shown that besides the spectral reflectance and transmittance the effective material tensors could be predicted. With this step, it has been shown how the introduced model can be successfully applied to describe and predict the optical properties of different metamolecules which is a further application of the model beyond the possibility to use it as a parameter retrieval.

Furthermore, the split-ring resonator has been considered to investigate quadratic nonlinear

effects, solely described by second-order multipoles. Such a multipole nonlinearity has been mentioned already by *Bloembergen*, and could be simultaneously observed for metamaterials in this work. A comparison between an alternative approach, i.e., the hydrodynamic electron model, verified that the multipole nonlinearity produces exactly the same source terms. Very interestingly, on the basis of the multipole model all nonlinear effects can be determined as soon as the linear response of the investigated metamaterial is described. While up to this point only the far-field properties of ensembles of metamolecules, exhibiting also second-order moments, have been considered, the multipole properties of isolated metamolecules have been investigated lastly. Therefore, the near-field patterns of the before-mentioned split-ring resonator and the cut-wire metamolecules have been calculated numerically and afterwards rigorously decomposed into their multipolar contributions. With this approach, the excitation of first- and second-order multipoles could be rigorously proven. Furthermore, it could be shown, how such an approach is conform with the *Mie theory*, which is one of the most important rigorous and exact methods to describe light matter interactions with particular objects.

In conclusion, the role of multipolar excitations in metamaterials has been discussed. The main intention was to develop a versatile analytical model to describe the desired metamolecules' properties of interest. The major focus was to understand how microscopic optical properties of isolated metamolecules translate into the optical properties of an ensemble, i.e., a metamaterial. As the most important result of this thesis it could be shown that the multipole expansion provides an excellent tool for this purpose.

## Perspective

There are several important points raised by this work that might be subject of further research. First, the transition and the investigation of bulk metamaterials beyond single layers of metamolecules might be of interest [LLZG09, KZS05]. For extended bulk metamaterials also higher-order propagation modes can be important [MRGC+10] that might be described by the multipole formalism as well. Thus, the multipole formalism with its underlying connection between microscopic and macroscopic Maxwell's equations could contribute to the *homogenization procedure* [ST10, MS10] for metamaterials, being an important and fundamental research topic.

Second, the coupling of metamolecules is an important topic, since it can be used to create new optical properties by coupling two known metamolecules with an initially different response [LCZG10, PLG+10]. Therefore the coupling constant, introduced in this work could be subject of a more thorough physical investigation. Additionally, this method of coupling metamolecules might be a promising approach to describe a third-order multipolar response, i.e., electric octupoles and magnetic quadrupoles. Up to now, the wave propagation in media possessing such multipolar contributions has not been investigated.

Third, there is a strong development in the combination of metamaterials with gain materials [NFL+09, WPT+10, PHS10b, XDK+10] and quantum dots [TPO+10, MRL+10], etc.

[OSZ+09]. Therefore, the multipole formalism to describe the properties of individual meta-molecules as well as ensembles might be a valuable tool. In this context the interaction of a quantum system, for example a three level system, with the carrier dynamics of a single metamolecule might be a physically interesting topic. The entire carrier dynamics can then be transformed into the multipole contribution to describe the macroscopic wave propagation properties as well. Hence, the known physics of the interaction of discrete molecular energy levels and electrodynamic multipoles can be extended for the case of metamaterials.

Lastly, there are systems that provide a resonant field confinement which is not based on localized plasmon-polaritons. For such systems, the description by propagating surface plasmon-polaritons might be much more appropriate. First examples of such arrangement have been reported recently [PHS+10a] and might be an alternative approach to alter the wave propagation in artificial materials.

Strongly connected to such kind of delocalized excitations is the double fishnet metamaterial [ZFM+05, ZFP+05] whose plasmonic mechanisms are still subject of ongoing research [MRMMGV09]. The fishnet material consists of a metal film with periodically arranged rectangular voids . The entire fishnet metamaterial comprises two of such layers that are closely spaced, similar to the cut-wire metamolecule. Due to the transverse conductive connection of adjacent unit cells, the isolated unit cell can no longer be reduced to a confined structure as it was the case for the metamolecules investigated in this work. For such structures the models applied for the microscopic carrier dynamics have to be modified and it has to be checked if a truncation of the multipole expansion up to the second order is sufficient to appropriately describe the optical response.

## Acknowledgements

Jörg Petschulat,
January 10, 2011, Jena.

# 6 Zusammenfassung

Die vorliegende Arbeit beschäftigt sich mit der Wechselwirkung von Licht mit metallischen Partikeln. Die charakteristischen Längenskalen für die Partikelabmessungen liegen dabei im Subwellenlängenbereich. Bei optischen Frequenzen ist dies gleichbedeutend mit typischen Partikeldimensionen im Bereich von 10 bis wenigen 100 Nanometern. Eine Besonderheit bei der Wechselwirkung von elektromagnetischer Strahlung mit derartigen Nanopartikeln ist die Anregung von an der Oberfläche lokalisierten Plasmon-Polaritonen. Dabei handelt es sich um einen Hybridzustand aus kollektiver Ladungsträgerbewegung (Plasmon) und lokaler Feldverteilung (Polariton). Sowohl die Feldverteilung als auch die intrinsische Ladungsträgerdynamik solcher Anregungen lassen sich bei sehr kleinen Partikeln, wie etwa kleinen Metallkugeln [BH83], mit der Anregung eines induzierten elektrischen Dipols beschreiben [BAA08].

Ein wesentliches Ziel dieser Dissertation bestand darin, Effekte der elektrischen Dipolanregung in metallischen Nanopartikeln zu untersuchen. In Teil 3 dieser Arbeit wurden zwei definierende Eigenschaften dipolartiger Nanostrukturen erforscht. Zum einen ist dies die Verstärkung des elektromagnetischen Lokalfeldes in der Umgebung des Nanopartikels und zum anderen die Möglichkeit, mit Ensembles von Nanostrukturen ein effektives Medium, ein sogenanntes Metamaterial, mit einer gezielt manipulierbaren elektrischen Permittivität zu realisieren. Die Permittivität wird dabei allein durch die makroskopische Polarisation aller mikroskopischen Dipolmomente bestimmt. Besonders die Ensembleanordnung im Gitter mit hohem Füllfaktor war hierbei bedeutend, denn diese ermöglichte die Anregung von propagierenden Oberflächen-Plasmon-Polaritonen. Dabei war die Gitteranordnung essentiell, da diese die notwendige Existenzbedingung in Form des transversalen Gittervektors bereit stellte. Beide plasmonischen Effekte konnten im Rahmen einer ausführlichen Untersuchung sowohl theoretisch anhand von rigorosen Rechnungen und analytischen Modellen als auch experimentell durch Transmissionsmessungen im Fernfeld beobachtet und zugeordnet werden. Zuletzt wurden beide plasmonischen Effekte angewandt, um Nanopartikel-Substrate zu etablieren, die mit zwei getrennt voneinander kontrollierbaren plasmonischen Anregungen spezifisch auf die Anforderungen der oberflächenverstärkte Ramanstreuung zugeschnitten wurden. Es konnte gezeigt werden, dass beide Effekte, die Anregung der elektrischen Dipolmode, also des lokalisierten Oberflächenplasmon-Polaritons, als auch die des propagierenden Plasmon-Polaritons in einer Verstärkung der Ramanstreuung des Analytes Kristallviolett resultieren.

In Teil 4 dieser Arbeit wurde eine weitere Klasse von Nanopartikeln untersucht, deren Beschreibung die Berücksichtigung höherer Momente erforderlich macht. Diese ermöglicht neben der Beeinflussung der effektiven elektrischen Permittivität auch eine magnetische Wechselwirkung. Derartige Strukturen wurden erstmals 1999 von *J. B. Pendry* eingeführt [PHRS99]. Seit dieser Pionierarbeit wurde eine Vielzahl von verschiedenen Nanostrukturen untersucht, welche den Zugang zu völlig neuartigen Propagationseigenschaften im daraus aufgebauten Metamaterial zugänglich machten. Grundlegend bei den in diesem Teil der Arbeit durchge-

führten Untersuchungen war die Einführung eines mikroskopisches Modellsystems welches die real vorkommenden komplexen Ladungsträgerbewegungen berücksichtigt. In dieser Arbeit wurde ein System bestehend aus gekoppelten Oszillatoren zu Grunde gelegt, um die feldinduzierte Ladungsträgerdynamik in der Nanostruktur zu modellieren.

Diese Art der mikroskopischen Beschreibung wurde bereits für die Beschreibung der Nanostrukturen im elektrischen Dipollimit benutzt. In äquivalenter Weise wird diese Art der Modellierung auch verwendet, um natürlich vorkommende Materialien, aufgebaut aus realen Atomen, bzw. Molekülen, zu beschreiben. Besonders in der festkörpertheoretischen Beschreibung von atomaren Gittern werden als eine erste Näherung oftmals Systeme von gekoppelten Oszillatoren verwendet, um die Ensembleeigenschaften des gesamten Gitters zu bestimmen.

Basierend auf der Kenntnis dieser mikroskopischen Ladungsbewegungen in den untersuchten Nanostrukturen war es möglich die Multipolentwicklung anzuwenden, und dabei die mikroskopischen Eigenschaften der Nanostruktur in makroskopische Ensembleeigenschaften zu überführen. Auf der Basis dieser Methode wurden in der vorliegenden Arbeit verschiedene Nanostrukturen behandelt. Als erstes wurde die *Cut-Wire Struktur* [SZO01, SCC⁺05, DEW⁺05] erforscht, um die effektiven Propagationseigenschaften im zugehörigen Metamaterial zu bestimmen. Dabei wurden die im Modellsystem unbekannten Oszillatorparameter durch den Vergleich der Dispersionsrelationen aus dem Modell mit denen rigoroser Rechnungen ermittelt. Die zweite untersuchte Struktur war der sogenannte *Split-Ring Resonator* [LEW⁺04]. Es konnte auch hier gezeigt werden, dass die effektiven Materialparameter sowie die Reflexions- und Transmissionskoeffizienten an einem Film solcher Strukturen sehr gut durch das eingeführte Modell beschrieben werden können. In weiteren Untersuchungen konnte gezeigt werden, dass mit den einmal bestimmten Modellparametern auch Vorhersagen über die optische Response von Strukturen gemacht werden können, die Veränderungen in ihrer Geometrie erfahren haben. Selbst bei Modifikationen, die eine Änderung der Polarisationseigenzustände von linearer zu elliptischer Polarisation hervorrufen, konnten die Reflexions- und Transmissionskoeffizienten für die parallel und die kreuzpolarisierten Komponenten vorhergesagt werden.

Ein weiterer wichtiger Punkt stellte die Untersuchung nichtlinearer Effekte in Metamaterialien dar. Dabei wurden Nichtlinearitäten betrachtet, die einzig durch die Geometrie der beleuchteten Nanostrukturen induziert werden. Diese strukturelle Nichtlinearität wird einzig durch spezielle intrinsische Ladungsträgerbewegungen induziert, anders als nichtlineare Effekte, die etwa durch die Anwesenheit eines nichtlinearen Kristalls hervorgerufen werden können. Solche intrinsischen Nichtlinearitäten können mit Multipolmomenten zweiter Ordnung erfasst werden. Basierend auf diesem Verfahren konnte gezeigt werden, dass diese Beschreibung zu den gleichen Quelltermen führt, wie sie auch bei einer Methode vorkommen, die als hydrodynamisches Plasmamodell [FLK⁺08, ZHL⁺09] bezeichnet wird. Als besonderer Vorteil einer solchen Modellierung ist zu erwähnen, dass alle nichtlinearen Koeffizienten bereits aus den linearen Metamaterialeigenschaften folgen.

Den letzten Punkt der Arbeit bilden die Nahfeldeigenschaften einzelner Nanostrukturen. Bis zu diesem Zeitpunkt wurden stets makroskopische Propagationseigenschaften in Metamaterialien im Rahmen der Multipolmethode untersucht. Dabei wurde zwar implizit angenommen,

dass sich jede Nanostruktur des Metamaterials durch Multipolmomente beschreiben lässt, untersucht wurde jedoch immer nur die optische Response des Ensembles. Im letzten Punkt dieser Arbeit wurden auch die Strahlungseigenschaften einzelner Strukturen in Multipolmomente zerlegt. Diese Zerlegung der rigoros ermittelten Nahfelder konnte benutzt werden, um die Multipolmomente erster und zweiter Ordnung anhand der Feldverteilung in unmittelbarer Umgebung um die jeweilige Struktur eindeutig nachzuweisen. Dieser Schritt vervollständigt somit diese Arbeit, in dem gezeigt werden konnte, dass auch auf mikroskopischer Ebene Multipolmomente erster und zweiter Ordnung zur Beschreibung der optischen Eigenschaften von Nanostrukturen verwendet werden können.

Zusammenfassend konnte gezeigt werden, dass mit der Multipolentwicklung bis zur zweiten Ordnung sowohl die mikroskopischen als auch die makroskopischen optischen Eigenschaften von Metamaterialien in konsistenter Form beschrieben werden können. Zu Grunde liegt der dabei eingesetzten und sehr allgemeinen Methode ein spezielles mikroskopisches Modell zur Beschreibung der Ladungsträgerdynamik in der Struktur. In dieser Arbeit wurde dafür ein System gekoppelter Oszillatoren eingesetzt, welches allerdings auch durch andere Modelle oder Methoden ersetzt werden kann. Diese einfachen Annahmen reichten jedoch aus, um eine qualitative und quantitative Beschreibung der komplizierten Licht-Materie Wechselwirkung in den untersuchten Metamaterialien zu erhalten. Diese Art der Modellierung bestehend aus mikroskopischer Ladungsträgerbeschreibung und anschließender Multipolentwicklung ist ein wesentliches Resultat dieser Arbeit. Für die Erforschung der Metamaterialien stellt diese Methode ein physikalisches, analytisches und methodisch intuitives Werkzeug dar, um auch komplexere Strukturen verstehen oder gezielt entwerfen zu können.

# Ehrenwörtliche Erklärung

Ich erkläre hiermit ich ehrenwörtlich, dass ich die vorliegende Arbeit selbstständig, ohne unzulässige Hilfe Dritter und ohne Benutzung anderer als der hier genannten Hilfsmittel und Literatur angefertigt habe. Die aus anderen Quellen direkt oder indirekt übernommenen Daten und Konzepte sind unter Angabe der Quelle gekennzeichnet.

Die Arbeit wurde bisher weder im In- noch im Ausland in gleicher oder ähnlicher Form einer anderen Prüfungsbehörde vorgelegt.

Die geltende Promotionsordnung der Physikalisch-Astronomischen Fakultät ist mir bekannt. Ich versichere ehrenwörtlich, dass ich nach bestem Wissen die reine Wahrheit gesagt und nichts verschwiegen habe.


Jörg Petschulat                                           Jena, 10. Januar, 2011.

# 7 Curriculum Vitae

## Personel

| | |
|---|---|
| Name | Jörg Petschulat |
| Date of birth | February 12th 1981 |
| Place of birth | Zwickau |
| Nationality | German |
| Email | joerg.petschulat@gmail.com |

## Awards and honors

- Carl Zeiss Scholarship for PhD students

## Education

| | |
|---|---|
| • Abitur at the Gymnasium "Am Sandberg" in Wilkau Haßlau, Germany | 1999 |
| • Basic military service | 1999-2000 |
| • Basic studies in physics at the University of Technology Chemnitz, Germany | 2000-2002 |
| • Diploma in physics at the Friedrich-Schiller-Universität Jena, Germany | 2005 |
| • Summer school for nonlinear and quantum optics in Krøgerup, Denmark | 2006 |

## Positions and Jobs

| | |
|---|---|
| • Student assistant at the FSU Jena, basic practical tutor | 10/2002 - 02/2003 |
| • Voluntary internship at the Carl Zeiss Company | 02/2003 - 03/2003 |
| • Student assistant at the FSU Jena, Quantum Mechanics support | 04/2003 - 07/2003 |
| • Diploma student at the Fraunhofer Institute of Applied Optics and Precision Engineering Jena, Germany, diploma thesis: "Manufacturing, characterization and theoretical description of stochastic nanostructures (moth-eye structures)" | 11/2004 - 09/2005 |
| • PhD student at the FSU Jena with a two month break (parental leave) | since 12/2005 |

## Teaching

| | |
|---|---|
| • Seminar leader "Theoretical Optics" | summer term 2006 |
| • Seminar leader "Computational Physics" | winter term 2006/2007 |
| • Seminar leader "Classical Electrodynamics" | summer term 2007 |
| • Seminar leader "Computational Physics" | winter term 2007/2008 |
| • Seminar leader "Computational Photonics" | summer term 2009 |
| • Seminar leader "Computational Photonics" | summer term 2010 |

# Journal publications

• J. Petschulat, C. Helgert, M. Steinert, N. Bergner, C. Rockstuhl, F. Lederer, T. Pertsch, A. Tünnermann, and E.-B. Kley, *Plasmonic modes of extreme sub-wavelength nanocavities*,
Opt. Lett. **35**, 2693-2695 (2010).

• J. Petschulat, C. Menzel, C. Rockstuhl, A. Chipouline, A. Tünnermann, F. Lederer, and T. Pertsch, *A simple and versatile analytical approach for planar metamaterials*,
Phys. Rev. B **82**, 075102 (2010).

• J. Petschulat, J. Yang, C. Menzel, C. Rockstuhl, A. Chipouline, P. Lalanne, A. Tünnermann, F. Lederer, and T. Pertsch, *Understanding the electric and magnetic response*
*of isolated metaatoms by means of a multipolar field decomposition*,
Opt. Express **18**, 14454-14466 (2010).

• D. Cialla, J. Petschulat, R. Siebert, U. Hübner, H. Schneidewind, M. Zeisberger, R. Mattheis, T. Pertsch, M. Schmitt, R. Möller, and J. Popp, *Investigation on the second part of the electro-magnetic SERS enhancement and resulting fabrication strategies of anisotropic plasmonic arrays*,
Chem. Phys. Chem. **11**, 1918-1924 (2010).

• J. Petschulat, D. Cialla, N. Janunts, C. Rockstuhl, U. Hübner, R. Möller, H. Schneidewind, R. Mattheis, J. Popp, A. Tünnermann, F. Lederer, and T. Pertsch, *Doubly resonant optical nanoantenna arrays for polariation resoved measurements of surface-enhanced Raman scattering*,
Opt. Express *18*, 4184-4197 (2009), selected for Apr. 2010 issue in Virtual Journal for Biomedical Optics.

• J. Petschulat, A. Chipouline, T. Pertsch, and A. Tünnermann, C. Menzel, C. Rockstuhl, and F. Lederer, *Multipole nonlinearity of metamaterials*,
Phys. Rev. A **80**, 063828 (2009).

• D. Cialla, R. Siebert, U. Hübner, R. Möller, R. Mattheis, J. Petschulat, A. Tünnermann, T. Pertsch, B. Dietzeck, and J. Popp, *Ultrafast plasmon dynamics and evanescent field distribution of reproducible surface-enhanced Raman-scattering substrates*,
Anal. Bioanal. Chem. **384**, 1811-1818 (2009).

• U. Hübner, J. Petschulat, E. Pshenay-Severin, A. Chipouline, T. Pertsch, C. Rockstuhl, and F. Lederer, *Negative-index materials: Two approaches for nano-fabricated metamaterials*,
Microelectron. Eng. **86**, 1138-1141 (2009).

- J. Petschulat, A. Chipouline, T. Pertsch, and A. Tünnermann, C. Menzel, C. Rockstuhl, and F. Lederer, *Multipole approach to metamaterials*, Phys. Rev. A **78**, 043811 (2008), selected for Oct. 2008 issue of Virtual Journal of Nanoscale Science and Technology.
- C. Rockstuhl, T. Zentgraf, E. Pshenay-Severin, J. Petschulat, A. Chipouline, J. Kuhl, T. Pertsch, H. Giessen, and F. Lederer, *The origin of magnetic polarizability in metamaterials at optical frequencies - an electrodynamic approach*, Opt. Express **15**, 8871-8883 (2007).

# Patents

- *Security element*,
J. Petschulat, M. Rahm, M. Dichtl, M. Heim, T. Kämpfe, T. Pertsch, E.-B. Kley, H. Lochbihler, German Patent, DE-10-2007-061-979-A1, int. classification WO/ 2009/083151 (2009).
- *Multicolored Security element*,
J. Petschulat, T. Pertsch, E.-B. Kley, C. Helgert, H. Lochbihler, German Patent, DE-10-2009-012-300-A1.

# Bookchapters

- J. Petschulat, C. Rockstuhl, C. Menzel, A. Chipouline, A. Tünnermann, F. Lederer, and T. Pertsch, *Multipole Metamaterials*, (contributed bookchapter, submitted), appearing in *Plasmonics and Plasmonic Metamaterials: Analysis and Applications*.

# Conference contributions

- J. Petschulat, A. Chipouline, C. Menzel, C. Rockstuhl, A. Tünnermann, F. Lederer, and T. Pertsch, *Assembling Metamaterials: A building block approach for near-field and conductively coupled meta-molecules,* (Talk/Paper) Metamaterials 2010, Karlsruhe, Germany (2010).
- J. Petschulat, F. Setzpfandt, C. Menzel, A. Chipouline, C. Rockstuhl, A. Tünnermann, F. Lederer, and T. Pertsch, *Understanding optical activity and EIT analogues in optical metamaterials with an analytical multipole analysis*, (Poster/Paper) CLEO, San Jose, USA (2010).
- J. Petschulat, A. Chipouline, C. Menzel, C. Rockstuhl, A. Tünnermann, F. Lederer, and T. Pertsch, *Multipole Nonlinearity - An Additional Bulk Effect for Particular Metamaterials*, (Poster/Paper) Photonic Nanostructures (PhoNa) Kickoff Meeting, Jena, Germany (2010).

- J. Petschulat, A. Chipouline, C. Menzel, C. Rockstuhl, A. Tünnermann, F. Lederer, and T. Pertsch, *Multipole Metamaterials: A mesoscopic investigation towards effective linear and nonlinear optical material interaction*, (Talk/Paper) conference proceedings Frontiers in Optics 2009, San Jose, USA (2009).
- J. Petschulat, A. Chipouline, C. Menzel, C. Rockstuhl, A. Tünnermann, F. Lederer, and T. Pertsch, *Multipole induced nonlinearity of metamaterials*, (Talk/Paper) conference proceedings Metamaterials 2009, London, United Kingdom (2009).
- J. Petschulat, A. Chipouline, C. Menzel, C. Rockstuhl, A. Tünnermann, F. Lederer, and T. Pertsch, *Multipole Metamaterials*, (Talk/Paper) conference proceedings CLEO Europe-EQEC, Munich, Germany (2009).
- J. Petschulat, A. Chipouline, E. Pshenay-Severin, A. Tünnermann, T. Pertsch, C. Menzel, T. Paul, and F. Lederer, *Analytical modelling of linear and nonlinear properties of metamaterials based on multipole expansion*, (Talk/Paper) conference proceedings SPIE Europe, Prague, Czech Republic (2009).
- J. Petschulat, A. Chipouline, E. Pshenay-Severin, A. Tünnermann, T. Pertsch, C. Menzel, C. Rockstuhl, T. Paul, and Falk Lederer, *Linear and Nonlinear Properties of Metamaterials: Analytical Modelling Based on Multipole Expansion*, (Poster/Abstract) Nanometa 2009, Seefeld, Austria (2009).
- J. Petschulat, A. Tünnermann, T. Pertsch, D. Cialla, H. Schneidewind, U. Hübner, J. Popp, C. Rockstuhl, and Falk Lederer, *Tailored Plasmonic Nanoantennas for SERS*, (Poster/Abstract) Nanometa 2009, Seefeld, Austria (2009).
- J. Petschulat, K. Wielgo, N. Janunts, A. Csaki, N. Jahr, W. Fritzsche, R. Poehlmann, C. Rockstuhl, T. Pertsch, F. Lederer, J. Popp and A. Tünnermann, *The influence of metal nanoparticles on light transmission through nanoholes*, (Talk/Abstract) Near Field Optics 10, Buenos Aires, Argentinia (2008).
- J. Petschulat, C. Menzel, C. Rockstuhl, A. Chipouline , T. Pertsch, F. Lederer, and A. Tünnermann, *Multipole Properties of Metamaterials*, (Talk/Abstract) Near Field Optics 10, Buenos Aires, Argentinia (2008).
- J. Petschulat, C. Rockstuhl, C. Menzel, T. Paul, A. Chipouline, T. Pertsch, A. Tünnermann, F. Lederer, *Light Propagation and Effective Parameters of Nanowire Based Meta-materials: An Analytical Approach*, (Poster/Paper) CLEO, San Jose, USA (2008).
- J. Petschulat, C. Menzel, C. Rockstuhl, A. Chipouline, T. Pertsch, and F. Lederer, *The dispersion relation for metamaterials: An analytical approach*, (Talk/Paper) META 08 & NATO Advanced Research Workshop 08, Marakesh, Morocco (2008).
- J. Petschulat, C. Menzel, A. Chipouline, C. Rockstuhl, T. Pertsch, A. Tünnermann, F. Lederer, *Multipole Properties of Metamaterials*, (Talk/Paper) conference proceedings SPIE Europe, Straßburg, France (2008).

- J. Petschulat, N. Bergner, E.-B. Kley, C. Rockstuhl, T. Pertsch, and F. Lederer, *Negative Refractive Index and Fabry Perot Resonances in 2D Plasmonic Waveguide Systems*, (Poster) Periodic Nanostructures for Photonics Seminar, Bad Honnef, Germany (2008).
- J. Petschulat, C. Rockstuhl, R. Leitel, O. Stenzel, T. Pertsch, A. Tünnermann, *Plasmon resonances in disordered metal-PMMA structures*, (Talk/Abstract), Proceedings of the European Optical Society, Topical Meeting on Nanoplasmonics, Engelberg, Switzerland (2006)

# 8 Bibliography

[Abb73]        E. Abbe. Beiträge zur Theorie des Mikroskops und der mikroskopischen Wahrnehmung IV. Das optische Vermögen des Mikroskops. *Arch. Mikr. Anat.*, 9(1):456–468, 1873.

[AE06]         A. Alù and N. Engheta. Optical nanotransmission lines: Synthesis of planar left-handed metamaterials in the infrared and visible regimes. *Journ. Opt. Soc. Am. B*, 23(3):571–583, 2006.

[AKGQ09]    S. S. Acimovic, M. P. Kreuzer, M. U. Gonzalez, and R. Quidant. Plasmon near-field coupling in metal dimers as a step toward single-molecule sensing. *ACS Nano*, 3(5):1231–1237, 2009.

[AS72]         M. Abramowitz and I. A. Stegun. *Handbook of Mathematical Functions with Formulas, Graphs, and Mathematical Tables*. Dover Publications, 9th printing, New York, 1972.

[BAA08]       G. W. Bryant, F. J. G. De Abajo, and J. Aizpuruas. Mapping the plasmon resonances of metallic nanoantennas. *Nano Lett.*, 8(2):631–636, 2008.

[Bal08]        C. A. Balanis. *Modern Antenna Handbook*. Wiley, New York, 2008.

[BC90]         P. Butcher and D. Cotter. *The Elements of Nonlinear Optics*. Cambridge University Press, Cambridge, 1990.

[BCM83]       P. Barber, R. Chang, and H. Massoudi. Electrodynamic calculations of the surface-enhanced electric intensities on large Ag spheroids. *Phys. Rev. B*, 27(12):7251–7261, 1983.

[BD63]         A. Buckingham and R. Disch. The quadrupole moment of the carbon dioxide molecule. *Proc. R. Soc. Lond.*, 273(1353):275–289, 1963.

[BDE03]        W. L. Barnes, A. Dereux, and T. W. Ebbesen. Surface plasmon subwavelength optics. *Nature*, 424(6950):824–830, 2003.

[BDO+10]      M. Burresi, D. Diessel, D. Oosten, S. Linden, M. Wegener, and L. Kuipers. Negative-index metamaterials: Looking into the unit cell. *Nano Lett.*, 10(7):2480–2483, 2010.

[BdWPA10]   S. P. Burgos, R. de Waele, A. Polman, and H. A. Atwater. A single-layer wide-angle negative-index metamaterial at visible frequencies. *Nature Mat.*, 9(5):407–412, 2010.

[BFL+07]     K. Busch, G. Von Freymann, S. Linden, S. Mingaleev, L. Tkeshelashvili, and M. Wegener. Periodic nanostructures for photonics. *Phys. Rep.*, 444(3-6):101–202, 2007.

[BH83]       C. F. Bohren and D. R. Huffman. *Absorption and Scattering of Light by Small Particles.* Wiley, New York, 1983.

[Blo65]      N. Bloembergen. *Nonlinear Optics.* World Scientific, 4th Edt. Singapore, 1965.

[BMH+10]     I. Bergmair, M. Mühlberger, K. Hingerl, E. Pshenay-Severin, T. Pertsch, E. B. Kley, H. Schmidt, and R. Schöftner. 3D materials made of gold using nanoimprint lithography. *Microelectron. Eng.*, 87(5-8):1008–1010, 2010.

[Boa11]      A. Boardman. Pioneers in metamaterials: John Pendry and Victor Veselago. *J. Opt.*, 13(2):020401, 2011.

[BOK+09]     M. Burresi, D. Van Oosten, T. Kampfrath, H. Schoenmaker, R. Heideman, A. Leinse, and L. Kuipers. Probing the magnetic field of light at optical frequencies. *Science*, 326(5952):550–553, 2009.

[Boy92]      R. W. Boyd. *Nonlinear Optics.* Academic Press, San Diego, 1992.

[BPQL10]     P. Banzer, U. Peschel, S. Quabis, and G. Leuchs. On the experimental investigation of the electric and magnetic response of a single nano-structure. *Opt. Express*, 18(10):10905–10923, 2010.

[BSA86]      J. J. Burke, G. I. Stegeman, and T. Amir. Surface-polariton-like waves guided by thin lossy films. *Phys. Rev. B*, 33(8):5186–5201, 1986.

[BT07]       B. Bai and J. Turunen. Fourier modal method for the analysis of second-harmonic generation in two-dimensionally periodic structures containing anisotropic materials. *Journ. Opt. Soc. Am. B*, 24(5):1105–1112, 2007.

[BVDZ10]     J. Bouillard, S. Vilain, W. Dickson, and A. Zayats. Hyperspectral imaging with scanning near-field optical microscopy: Applications in plasmonics. *Opt. Express*, 18(16):16513–16519, 2010.

[BW99]       M. Born and E. Wolf. *Principles of Optics.* Cambridge, New York, 1999.

[Cas45]      H. B. G. Casimir. On Onsager's principle of microscopic reversibility. *Rev. Mod. Phys.*, 17(2,3):343–350, 1945.

[CFMW86]     K. T. Carron, W. Fluhr, M. Meier, and A. Wokaun. Resonances of two-dimensional particle gratings in surface-enhanced Raman scattering. *J. Opt. Soc. Am. B*, 3(3):430–440, 1986.

[CK98]        A. Campion and P. Kambhampati. Surface-enhanced Raman scattering. *Chem. Soc. Rev.*, 27(4):241–250, 1998.

[CKK+05]      B. K. Canfield, S. Kujala, M. Kauranen, K. Jefimovs, T. Vallius, and J. Turunen. Electromagnetic parameter retrieval from inhomogeneous metamaterials. *Appl. Phys. Lett.*, 86(18):183109, 2005.

[CME+08]      A. Christ, O. J. F. Martin, Y. Ekinci, N. A. Gippius, and S. G. Tikhodeev. Symmetry breaking in a plasmonic metamaterial at optical wavelength. *Nano Lett.*, 8(8):2171–2175, 2008.

[COM10]       COMSOL. Commercial software package for numerical simulations on the basis of finite element methods (fem). formerly known as FEMLAB. Costumers website www.comsol.com., 2010.

[CPH+10]      D. Cialla, J. Petschulat, U. Hübner, H. Schneidewind, M. Zeisberger, R. Mattheis, T. Pertsch, M. Schmitt, R. Möller, and J. Popp. Investigation on the second part of the electromagnetic SERS enhancement and resulting fabrication strategies of anisotropic plasmonic arrays. *Chem. Phys. Chem.*, 11(9):1918–1924, 2010.

[CSH+09]      D. Cialla, R. Siebert, U. Hübner, R. Möller, H. Schneidewind, R. Mattheis, J. Petschulat, A. Tünnermann, T. Pertsch, B. Dietzek, and J. Popp. Ultrafast plasmon dynamics and evanescent field distribution of reproducible surface-enhanced Raman-scattering substrates. *Anal. Bioanal. Chem.*, 394(7):1811–1818, 2009.

[DDLW10]      D. Diessel, M. Decker, S. Linden, and M. Wegener. Near-field optical experiments on low-symmetry split-ring-resonator arrays. *Opt. Lett.*, 35(21):3661–3663, 2010.

[DEW+05]      G. Dolling, C. Enrich, M. Wegener, J. F. Zhou, C. M. Soukoulis, and S. Linden. Cut-wire pairs and plate pairs as magnetic atoms for optical metamaterials. *Opt. Lett.*, 30(23):3198–3200, 2005.

[DGV10]       T. J. Davis, D. E. Gomez, and K. C. Vernon. Simple model for the hybridization of surface plasmon resonances in metallic nanoparticles. *Nano Lett.*, 10(7):2618–2625, 2010.

[dLR05]       O. L. de Lange and R. E. Raab. Traceless multipole moment densities and transformations in macroscopic electromagnetism. *Phys. Rev. E*, 71(3):036620, 2005.

[DLW09]       M. Decker, S. Linden, and M. Wegener. Coupling effects in low-symmetry planar split-ring resonator arrays. *Opt. Lett.*, 34(10):1579–1581, 2009.

[DVK+10]     J. Dorfmüller, R. Vogelgesang, W. Khunsin, C. Rockstuhl, C. Etrich, and K. Kern. Plasmonic nanowire antennas: Experiment, simulation, and theory. *Nano Lett.*, 10(9):3596–3603, 2010.

[DWSL07]     G. Dolling, M. Wegener, C. Soukoulis, and S. Linden. Negative-index meta-material at 780 nm wavelength. *Opt. Lett.*, 32(1):53–55, 2007.

[EB10]       S. Essig and K. Busch. Generation of adaptive coordinates and their use in the Fourier Modal Method. *Opt. Express*, 18(22):23258–23274, 2010.

[ELG+98]     T. W. Ebbesen, H. J. Lezec, H. F. Ghaemi, T. Thio, and P. A. Wolff. Extraordinary optical transmission through sub-wavelength hole arrays. *Nature*, 391(6668):667–669, 1998.

[ETG10]      R. Esteban, T. V. Teperik, and J. J. Greffet. Optical patch antennas for single photon emission using surface plasmon resonances. *Phys. Rev. Lett.*, 104(2):026802, 2010.

[FDMMM09]    A. Fernández-Domínguez, E. Moreno, and L. Martín-Moreno. Terahertz wedge plasmon polaritons. *Opt. Lett.*, 34(13):2063–2065, 2009.

[FDMMMGV09]  A. Fernández-Domínguez, E. Moreno, L. Martín-Moreno, and F. García-Vidal. Guiding terahertz waves along subwavelength channels. *Phys. Rev. B*, 79(23):233104, 2009.

[FDT10]      RSoft FullWave FDTD. Part of the RSoft design suite. Costumers website www.rsoftdesign.com., 2010.

[FHM74]      M. Fleischmann, P. Hendra, and A. J. McQuillan. Raman spectra of pyridine adsorbed at a silver electrode. *Chem. Phys. Lett.*, 26(2):163–166, 1974.

[FKH+10]     N. Feth, M. König, M. Husnik, K. Stannigel, J. Niegemann, K. Busch, M. Wegener, and S. Linden. Electromagnetic interaction of split-ring resonators: The role of separation and relative orientation. *Opt. Express*, 18(7):6545–6554, 2010.

[FLK+08]     N. Feth, S. Linden, M. W. Klein, M. Decker, F. B. P. Niesler, Y. Zeng, W. Hoyer, J. Liu, S. W. Koch, J. V. Moloney, and M. Wegener. Second-harmonic generation from complementary split-ring resonators. *Opt. Lett.*, 33(17):1975–1977, 2008.

[FM03]       L. B. Felsen and N. Marcuvitz. *Radiation and Scattering of Waves*. Wiley, New Jersey, 2003.

[FNDM09]     A. M. Funston, C. Novo, T. J. Davis, and P. Mulvaney. Plasmon coupling of gold nanorods at short distances and in different geometries. *Nano Lett.*, 9(4):1651–1658, 2009.

[Fre07] J. Freidberg. *Plasma Physics and Fusion Energy.* Cambridge University Press, Cambridge, 2007.

[FSD08] Y. Fang, N.-H. Seong, and D. Dlott. Measurement of the distribution of site enhancements in surface-enhanced Raman scattering. *Science*, 321(5887):388–392, 2008.

[FSZ+07] V. A. Fedotov, A. S. Schwanecke, N. I. Zheludev, V. V. Khardikov, and S. L. Prosvirnin. Asymmetric transmission of light and enantiomerically sensitive plasmon resonance in planar chiral nanostructures. *Nano Lett.*, 7(7):1996–1999, 2007.

[GAB+99] S. Gresillon, L. Aigouy, A. C. Boccara, J. C. Rivoal, X. Quelin, C. Desmarest, P. Gadenne, V. A. Shubin, A. K. Sarychev, and V. M. Shalaev. Experimental observation of localized optical excitations in random metal-dielectric films. *Phys. Rev. Lett.*, 82(22):4520–4523, 1999.

[GHMG10] Y. Gu, L. Huang, O. J. F. Martin, and Q. Gong. Resonance fluorescence of single molecules assisted by a plasmonic structure. *Phys. Rev. B*, 81(19):193103, 2010.

[GKM10] B. Gallinet, A. M. Kern, and O. J. F. Martin. Accurate and versatile modeling of electromagnetic scattering on periodic nanostructures with a surface integral approach. *Journ. Opt. Soc. Am. A*, 27(10):2261–2271, 2010.

[GN80] J. Gersten and A. Nitzan. Electromagnetic theory of enhanced Raman scattering by molecules adsorbed on rough surfaces. *J. Chem. Phys.*, 73(7):3023–3037, 1980.

[GN81] J. Gersten and A. Nitzan. Spectroscopic properties of molecules interacting with small dielectric particles. *J. Chem. Phys.*, 75(3):1139–1152, 1981.

[GPR92] E. B. Graham, J. Pierrus, and R. E. Raab. Multipole moments and Maxwell's equations. *J. Phys. B*, 25:4673–4684, 1992.

[Gri09] N. I. Grigorchuk. Theory for absorption of ultrashort laser pulses by spheroidal metallic nanoparticles. *Phys. Rev. B*, 80(15):155456, 2009.

[GT92] P. M. Goorjian and A. Taflove. Direct time integration of Maxwell's equations in nonlinear dispersive media for propagation and scattering of femtosecond electromagnetic solitons. *Opt. Lett.*, 17(3):180–182, 1992.

[GV09] H. Giessen and R. Vogelgesang. Glimpsing the weak magnetic field of light. *Science*, 326(5952):529–530, 2009.

[GVMMP05]   F. Garcia-Vidal, L. Martin-Moreno, and J. B. Pendry. Surfaces with holes in them: New plasmonic metamaterials. *J. Opt. A: Pure Appl. Opt.*, 7(2):S97–S101, 2005.

[HBS+08]   U. Hübner, R. Boucher, H. Schneidewind, D. Cialla, and J. Popp. Microfabricated SERS-arrays with sharp-edged metallic nanostructures. *Microelectron. Eng.*, 85(8):1792–1794, 2008.

[HES05]   A. P. Hibbins, B. R. Evans, and J. R. Sambles. Experimental verification of designer surface plasmons. *Science*, 308(5722):670–672, 2005.

[HKF+08]   M. Husnik, M. W. Klein, N. Feth, M. König, J. Niegemann, K. Busch, S. Linden, and M. Wegener. Absolute extinction cross-section of individual magnetic split-ring resonators. *Nature Photon.*, 2(10):614, 2008.

[HMR+09]   C. Helgert, C. Menzel, C. Rockstuhl, E. Pshenay-Severin, E.-B. Kley, A. Chipouline, A. Tünnermann, F. Lederer, and T. Pertsch. Polarization-independent negative-index metamaterial in the near infrared. *Opt. Lett.*, 34(5):704–706, 2009.

[Jac75]   J. D. Jackson. *Classical Electrodynamics*. Wiley, New York, 1975.

[JAN06]   Z. Jacob, L. V. Alekseyev, and E. Narimanov. Optical hyperlens: Far-field imaging beyond the diffraction limit. *Opt. Express*, 14(18):8247–8256, 2006.

[JC72]   P. B. Johnson and R. W. Christy. Optical constants of the noble metals. *Phys. Rev. B*, 6(12):4370–4279, 1972.

[Jin93]   J. Jin. *The Finite Element Method in Electromagnetism*. Wiley, New York, 1993.

[KBN10]   M. König, K. Busch, and J. Niegemann. The discontinuous Galerkin time-domain method for Maxwell's equations with anisotropic materials. *Photon. Nanostruct.: Fundam. Appl.*, 8(4):303–309, 2010.

[Kit95]   C. Kittel. *Introduction to Solid State Physics*. Wiley, New York, 1995.

[KKH10]   T. Kosako, Y. Kadoya, and H. F. Hofmann. Directional control of light by a nano-optical Yagi-Uda antenna. *Nature Photon.*, 4(5):312–315, 2010.

[KKK+05]   N. Katsarakis, G. Konstantinidis, A. Kostopoulos, R. S. Penciu, T. F. Gundogdu, M. Kafesaki, E. N. Economou, T. Koschny, and C. M. Soukoulis. Magnetic response of split-ring resonators in the far-infrared frequency regime. *Opt. Lett.*, 30(11):1348–1350, 2005.

[KMK06]   K. Kneipp, M. Moskovits, and H. Kneipp. *Surface-enhanced Raman Scattering*. Springer, Berlin, 2006.

[KWFL07]   M. W. Klein, M. Wegener, N. Feth, and S. Linden. Experiments on second- and third-harmonic generation from magnetic metamaterials. *Opt. Express*, 15(8):5238–5247, 2007.

[KYF+09]   A. Kinkhabwala, Z. Yu, S. Fan, Y. Avlasevich, K. Muellen, and W. E. Moerner. Large single-molecule fluorescence enhancements produced by a bowtie nanoantenna. *Nature Photon.*, 3(11):654–657, 2009.

[KZS05]   T. Koschny, L. Zhang, and C. M. Soukoulis. Isotropic three-dimensional left-handed metamaterials. *Phys. Rev. B*, 71(12):121103(R), 2005.

[LBB+09]   M. Losurdo, M. Bergmair, G. Bruno, D. Cattelan, C. Cobet, A. Martino, K. Fleischer, Z. Dohcevic-Mitrovic, N. Esser, M. Galliet, R. Gajic, D. Hemzal, K. Hingerl, J. Humlicek, R. Ossikovski, Z. V. Popovic, and O. Saxl. Spectroscopic ellipsometry and polarimetry for materials and systems analysis at the nanometer scale: state-of-the-art, potential, and perspectives. *J. Nanopart. Res.*, 11(7):1521–1554, 2009.

[LBC+81]   P. F. Liao, J. G. Bergman, D. S. Chemla, A. Wokaun, J. Melngailis, W. Hawryluk A, and N. P. Economou. Surface-enhanced Raman scattering from microlithographic silver particle surfaces. *Chem. Phys. Lett.*, 82(2):355–359, 1981.

[LBLX86]   J. R. Lombardi, R. L. Birke, T. Lu, and J. Xu. Charge transfer theory of surface enhanced Raman spectroscopy: Herzberg-Teller contributions. *J. Chem. Phys.*, 84(8):4174–4180, 1986.

[LCXX10]   G. Li, L. Cai, F. Xiao, and A. Xu. Theoretical reexamination of the cross conversion between surface plasmon polaritons and quasi-cylindrical waves. *Opt. Lett.*, 35(19):3162–3164, 2010.

[LCZG10]   H. Liu, J. X. Cao, S. N. Zhu, and H. Giessen. Lagrange model for the chiral optical properties of stereometamaterials. *Phys. Rev. B*, 81(24):241403, 2010.

[Leo06]   U. Leonhardt. Optical conformal mapping. *Science*, 312(5781):1777–1780, 2006.

[LEW+04]   S. Linden, C. Enkrich, M. Wegener, J. Zhou, T. Koschny, and C. M. Soukoulis. Magnetic response of metamaterials at 100 terahertz. *Science*, 306(5700):1351–1353, 2004.

[LGF+08]   N. Liu, H. Guo, L. Fu, S. Kaiser, H. Schweizer, and H. Giessen. Three-dimensional photonic metamaterials at optical frequencies. *Nature Mat.*, 7(1):31–37, 2008.

[Lie03]      L. Lie. Fourier modal method for crossed anisotropic gratings with arbitrary permittivity and permeability tensors. *J. Opt. A: Pure Appl. Opt.*, 5:345–355, 2003.

[LL85]       L. D. Landau and E. M. Lifschitz. *Elektrodynamik der Kontinua*. Akademie-Verlag, Berlin, 1985.

[LL08]       H. Liu and P. Lalanne. Microscopic theory of the extraordinary optical transmission. *Nature*, 452(7188):728–731, 2008.

[LLX+07]     Z. Liu, H. Lee, Y. Xiong, C. Sun, and X. Zhang. Far-field optical hyperlens magnifying sub-diffraction-limited objects. *Science*, 315(5819):1686, 2007.

[LLZG09]     N. Liu, H. Liu, S. Zhu, and H. Giessen. Stereometamaterials. *Nature Photon.*, 3(3):157–162, 2009.

[LW82]       P. F. Liao and A. Wokaun. Lightning rod effect in surface enhanced Raman scattering. *J. Am. Chem.*, 76(1):751–752, 1982.

[MAMMGV06]   S. A. Maier, S. R. Andrews, L. Martín-Moreno, and F. García-Vidal. Terahertz surface plasmon-polariton propagation and focusing on periodically corrugated metal wires. *Phys. Rev. Lett.*, 97(17):176805, 2006.

[MCS+10]     S. Mahajan, R. M. Cole, J. D. Speed, S. H. Pelfrey, A. E. Russell, P. N. Bartlett, S. M Barnett, and J. J. Baumberg. Understanding the surface-enhanced Raman spectroscopy "background". *J. Phys. Chem. C*, 114(16):7242–7250, 2010.

[MEM+05]     P. Mühlschlegel, H. J. Eisler, O. J. F. Martin, B. Hecht, and D. W. Pohl. Resonant optical antennas. *Science*, 308(5728):1607–1609, 2005.

[MG81]       M. G. Moharam and T. K. Gaylord. Coupled-wave analysis of reflection gratings. *Appl. Phys.*, 20:240–244, 1981.

[Mie08]      G. Mie. Beiträge zur Optik trüber Medien, speziell kolloidaler Metallösungen. *Ann. Phys.*, 25(3):377–445, 1908.

[MN53]       P. Mazur and B. R. A. Nijboer. On the statistical mechanics of matter in an electromagnetic field. *Physica*, 19:971–986, 1953.

[Mos85]      M. Moskovits. Surface-enhanced spectroscopy. *Rev. Mod. Phys.*, 57(3):783–826, 1985.

[MP98]       O. J. F. Martin and N. Piller. Electromagnetic scattering in polarizable backgrounds. *Phys. Rev. E*, 58(3):3909–3915, 1998.

[MPR⁺10]   C. Menzel, T. Paul, C. Rockstuhl, T. Pertsch, S. Tretyakov, and F. Lederer. Validity of effective material parameters for optical fishnet metamaterials. *Phys. Rev. B*, 81(3):035320, 2010.

[MRGC⁺10]   D. Mogilevtsev, E. Reyes-Gómez, S. B. Cavalcanti, C. A. A. De Carvalho, and L. E. Oliveira. Plasmon polaritons in photonic metamaterial superlattices: Absorption effects. *Phys. Rev. E*, 81(4):047601, 2010.

[MRL⁺10]   N. Meinzer, M. Ruther, S. Linden, C. M. Soukoulis, G. Khitrova, J. Hendrickson, J. D. Olitsky, H. M. Gibbs, and M. Wegener. Arrays of Ag split-ring resonators coupled to InGaAs single-quantum-well gain. *Opt. Express*, 18(23):24140–24151, 2010.

[MRMMGV09]   A. Mary, S. Rodrigo, L. Martín-Moreno, and F. García-Vidal. Holey metal films: From extraordinary transmission to negative-index behavior. *Phys. Rev. B*, 80(16):165431, 2009.

[MS10]   D. Morits and C. R. Simovski. Electromagnetic characterization of planar and bulk metamaterials: A theoretical study. *Phys. Rev. B*, 82(16):165114, 2010.

[NE97]   S. Nie and S. R. Emory. Probing single molecules and single nanoparticles by surface-enhanced Raman scattering. *Science*, 275(5303):1102–1106, 1997.

[NFL⁺09]   F. B. P. Niesler, N. Feth, S. Linden, J. Niegemann, J. Gieseler, K. Busch, and M. Wegener. Second-harmonic generation from split-ring resonators on a GaAs substrate. *Opt. Lett.*, 34(13):1997–1999, 2009.

[NH06]   L. Novotny and B. Hecht. *Principles of Nano-Optics*. Cambridge Press, New York, 2006.

[NKS⁺07]   J. Nelayah, M. Kociak, O. Stephan, F. J. Garcia de Abajo, M. Tence, L. Henrard, D. Taverna, I. Pastorizia-Santos, L. M. Liz-Marzan, and C. Colliex. Mapping surface plasmons on a single metallic nanoparticle. *Nature Phys.*, 3(5):348–353, 2007.

[NMCFD⁺10]   M. Nesterov, D. Martin-Cano, A. Fernandez-Dominguez, E. Moreno, L. Martin-Moreno, and F. J. Garcia-Vidal. Geometrically induced modification of surface plasmons in the optical and telecom regimes. *Opt. Lett.*, 35(3):423–425, 2010.

[NMMB07]   N.-A. P. Nicorovici, G. W. Milton, R. C. McPhedran, and L. C. Botten. Quasistatic cloaking of two-dimensional polarizable discrete systems by anomalous resonance. *Opt. Express*, 15(10):6314–6323, 2007.

[Nol02]   W. Nolting. *Grundkurs Theoretische Physik: Elektrodynamik*. Springer, Heidelberg, 2002.

[Nov06]      L. Novotny. Effective wavelength scaling for optical antennas. *Phys. Rev. Lett.*, 98:266802, 2006.

[Ons31]      L. Onsager. Reciprocal relations in irreversible processes. I. *Phys. Rev.*, 37(4):405–426, 1931.

[ORI⁺10]     A. F. Oskooi, D. Roundy, M. Ibanescu, P. Bermel, J. D. Joannopoulos, and S. G. Johnson. MEEP: A flexible free-software package for electromagnetic simulations by the FDTD method. *Comp. Phys. Comm.*, 181(3):687–702, 2010.

[OSZ⁺09]     R. F. Oulton, V. J. Sorger, T. Zentgraf, R. M. Ma, C. Gladden, L. Dai, G. Bartal, and X. Zhang. Plasmon lasers at deep subwavelength scale. *Nature*, 461(7264):629–632, 2009.

[PC85]       R. H. Price and R. J. Crowley. The lightning-rod fallacy. *Am. J. Phys.*, 53(9):843–848, 1985.

[PCT⁺09]     J. Petschulat, A. Chipouline, A. Tünnermann, T. Pertsch, C. Menzel, C. Rockstuhl, and F. Lederer. Multipole nonlinearity of metamaterials. *Phys. Rev. A*, 80(6):063828, 2009.

[PCT⁺10]     J. Petschulat, A. Chipouline, A. Tünnermann, T. Pertsch, C. Menzel, C. Rockstuhl, T. Paul, and F. Lederer. Simple and versatile analytical approach for planar metamaterials. *Phys. Rev. B*, 82(7):075102, 2010.

[Pen00]      J. B. Pendry. Negative refraction makes a perfect lens. *Phys. Rev. Lett.*, 85(18):3966–3969, 2000.

[Pera]       Perkin Elmer company. *Instrument manual for the Perkin Elmer Lambda 950 spectrometer.*

[Perb]       PerkinElmer. For further information see instruments description available at the supplier homepage: www.perkinelmer.com.

[Per63]      P. S. Pershan. Nonlinear optical properties of solids: Energy considerations. *Phys. Rev.*, 130(3):919–929, 1963.

[PFMZ09]     N. Papasimakis, V. A. Fedotov, K. Marinov, and N. I. Zheludev. Gyrotropy of a metamolecule: Wire on a torus. *Phys. Rev. Lett.*, 103(9):093901, 2009.

[PFZ11]      E. Plum, V. A. Fedotov, and N. I. Zheludev. Asymmetric transmission: A generic property of two-dimensional periodic patterns. *J. Opt.*, 13(2):024006, 2011.

[PHRS99]     J. B. Pendry, A. J. Holden, D. J. Robbins, and W. J. Stewart. Magnetism from conductors and enhanced nonlinear phenomena. *IEEE Trans. Microwave Theory Tech.*, 47(11):2075–2084, 1999.

[PHS+10a]    J. Petschulat, C. Helgert, M. Steinert, N. Bergner, C. Rockstuhl, F. Lederer, T. Pertsch, A. Tünnermann, and E.-B. Kley. Plasmonic modes of extreme subwavelength nanocavities. *Opt. Lett.*, 35(16):2693–2695, 2010.

[PHS10b]     E. Poutrina, D. Huang, and D. R. Smith. Analysis of nonlinear electromagnetic metamaterials. *New J. Phys.*, 12(9):093010, 2010.

[PHSY96]     J. B. Pendry, A. J. Holden, W. J. Stewart, and I. Youngs. Extremely low frequency plasmons in metallic mesostructures. *Phys. Rev. Lett.*, 76(25):4773–4776, 1996.

[PLF+09]     E. Plum, X.-X Liu, V. A. Fedotov, Y. Chen, D. P. Tsai, and N. I. Zheludev. Metamaterials: Optical activity without chirality. *Phys. Rev. Lett.*, 102(11):113902, 2009.

[PLG+10]     D. A. Powell, M. Lapine, M. V. Gorkunov, I. V. Shadrivov, and Y. S. Kivshar. Metamaterial tuning by manipulation of near-field interaction. *Phys. Rev. B*, 82(15):155128, 2010.

[PMC+08]     J. Petschulat, C. Menzel, A. Chipouline, C. Rockstuh, A. Tünnermann, F. Lederer, and T. Pertsch. Multipole approach to metamaterials. *Phys. Rev. A*, 78(4):043811, 2008.

[PMMGV04]    J. Pendry, L. Martin-Moreno, and F. Garcia-Vidal. Mimicking surface plasmons with structured surfaces. *Science*, 305(5685):847–848, 2004.

[PSSH+10]    E. Pshenay-Severin, F. Setzpfandt, C. Helgert, U. Hübner, C. Menzel, A. Chipouline, C. Rockstuhl, A. Tünnermann, F. Lederer, and T. Pertsch. Experimental determination of the dispersion relation of light in metamaterials by white-light interferometry. *J. Opt. Soc. Am. B*, 27(4):660–666, 2010.

[PWAB10]     A. Pors, M. Willatzen, O. Albrektsen, and S. I. Bozhevolnyi. From plasmonic nanoantennas to split-ring resonators: Tuning scattering strength. *J. Opt. Soc. Am. B*, 27(8):1680–1687, 2010.

[PYM+10]     J. Petschulat, J. Yang, C. Menzel, C. Rockstuhl, A. Chipouline, P. Lalanne, A. Tünnermann, F. Lederer, and T. Pertsch. Understanding the electric and magnetic response of isolated metaatoms by means of a multipolar field decomposition. *Opt. Express*, 18(14):14454–14466, 2010.

[PZ09]       S. L. Prosvirnin and N. I. Zheludev. Analysis of polarization transformations by a planar chiral array of complex-shaped particles. *J. Opt. A: Pure Appl. Opt.*, 11(7):074002, 2009.

[PZD+09]    E. Plum, J. Zhou, J. Dong, V. A. Fedotov, T. Koschny, C. M. Soukoulis, and N. I. Zheludev. Metamaterial with negative index due to chirality. *Phys. Rev. B*, 79(3):035407, 2009.

[Rae88]     H. Raether. *Surface Plasmons*. Springer, Berlin, 1988.

[Ram05]     S. A. Ramakrishna. Physics of negative refractive index materials. *Rep. Prog. Phys.*, 68(2):449–521, 2005.

[RBME07]    E. C. Le Ru, E. Blackie, M. Meyer, and P. G. Etchegoin. Surface enhanced Raman scattering enhancement factors: A comprehensive study. *J. Phys. Chem. C*, 111(37):13794–13803, 2007.

[Rem06]     R. F. Remis. Stability of FDTD on nonuniform grids for Maxwell's equations in lossless media. *J. Comput. Phys.*, 218(2):594–606, 2006.

[Rit57]     R. H. Ritchie. Plasma losses by fast electrons in thin films. *Phys. Rev.*, 106(5):874–881, 1957.

[RLE+06]    C. Rockstuhl, F. Lederer, C. Etrich, T. Zentgraf, J. Kuhl, and H. Giessen. On the reinterpretation of resonances in split-ring-resonators at normal incidence. *Opt. Express*, 14(19):8827–8836, 2006.

[Rus70]     G. Russakoff. A derivation of the macroscopic Maxwell equations. *Am. J. Phys.*, 38(10):1188–1195, 1970.

[SCC+05]    V. M. Shalaev, W. Cai, U. K. Chettiar, H.-K. Yuan, A. K. Sarychev, V. P. Drachev, and A. V. Kildishev. Negative index of refraction in optical metamaterials. *Opt. Lett.*, 30(24):3356–3358, 2005.

[SE06]      A. Salandrino and N. Engheta. Far-field subdiffraction optical microscopy using metamaterial crystals: Theory and simulations. *Phys. Rev. B*, 74(7):075103, 2006.

[SFS+05]    P. J. Schuck, D. P. Fromm, A. Sundaramurthy, G. S. Kino, and W. E. Moerner. Improving the mismatch between light and nanoscale objects with gold bowtie nanoantennas. *Phys. Rev. Lett.*, 94(1):017402, 2005.

[SFVK09]    I. Sersic, M. Frimmer, E. Verhagen, and A. F. Koenderink. Electric and magnetic dipole coupling in near-infrared split-ring metamaterial arrays. *Phys. Rev. Lett.*, 103(21):213902, 2009.

[SFW+02]    C. Soennichsen, T. Franzl, T. Wilk, G. Von Plessen, J. Feldmann, O. Wilson, and P. Mulvaney. Drastic reduction of plasmon damping in gold nanorods. *Phys. Rev. Lett.*, 88(7):77402, 2002.

[Sha07]      V. M. Shalaev. Optical negative-index metamaterials. *Nature Photon.*, 1(1):41–48, 2007.

[SHD07]     I. I. Smolyaninov, Y.-J. Hung, and C. C. Davis. Magnifying superlens in the visible frequency range. *Science*, 315(5819):1699–1701, 2007.

[Sla64]       J. C. Slater. Atomic radii in crystals. *J. Chem. Phys.*, 41(10):3199–3204, 1964.

[SLHC01]   E. Silberstein, P. Lalanne, J.-P. Hugonin, and Q. Cao. Use of grating theories in integrated optics. *J. Opt. Soc. Am. A*, 18(11):2865–2875, 2001.

[SMJ$^+$06]   D. Schurig, J. J. Mock, B. J. Justice, S. A. Cummer, J. B. Pendry, A. F. Starr, and D. R. Smith. Metamaterial electromagnetic cloak at microwave frequencies. *Science*, 314(5801):977–980, 2006.

[SPM$^+$09]   R. Singh, E. Plum, C. Menzel, C. Rockstuhl, A. K. Azad, R. A. Cheville, F. Lederer, W. Zhang, and N. I. Zheludev. Terahertz metamaterial with asymmetric transmission. *Phys. Rev. B*, 80(15):153104, 2009.

[SPV$^+$00]   D. R. Smith, W. J. Padilla, D. C. Vier, S. C. Nemat-Nasser, and S. Schultz. Composite medium with simultaneously negative permeability and permittivity. *Phys. Rev. Lett.*, 84(18):4184–4187, 2000.

[SR97]       L. F. Shampine and M. W. Reichelt. The MATLAB ODE suite. *SIAM J. Sci. Comput.*, 18(1):1–22, 1997.

[SSS01]      R. A. Shelby, D. R. Smith, and S. Schultz. Experimental verification of a negative index of refraction. *Science*, 292(5514):77–79, 2001.

[ST10]        C. R. Simovski and S. A. Tretyakov. On effective electromagnetic parameters of artificial nanostructured magnetic materials. *Photon. Nanostruct.: Fundam. Appl.*, 8(4):254–263, 2010.

[Sto97]       M. I. Stockman. Inhomogeneous eigenmode localization, chaos, and correlations in large disordered clusters. *Phys. Rev. E*, 56(6):6494–6507, 1997.

[SVKS05]   D. R. Smith, D. C. Vier, T. Koschny, and C. M. Soukoulis. Electromagnetic parameter retrieval from inhomogeneous metamaterials. *Phys. Rev. E*, 71(3):036617, 2005.

[SZO01]      Y. Svirko, N. Zheludev, and M. Osipov. Layered chiral metallic microstructures with inductive coupling. *Appl. Phys. Lett.*, 78(4):498–500, 2001.

[Taf95]       A. Taflove. *Computational Electrodynamics: The Finite-Difference Time-Domain Method*. Artech House, London, 1995.

[TMS62]     R. W. Terhune, P. D. Maker, and C. M. Savage. Optical harmonic gernation in calcite. *Phys. Rev. Lett.*, 8(10):404–406, 1962.

[TPdA+06]   T. V. Teperik, V. V. Popov, F. J. Garcia de Abajo, M. E. Abdelsalam, and P. N. Bartlett. Strong coupling of light to flat metals via a buried nanovoid lattice: The interplay of localized and free plasmons. *Opt. Express*, 14(5):1965–1972, 2006.

[TPO+10]    K. Tanaka, E. Plum, J. Ou, T. Uchino, and N. I. Zheludev. Multifold enhancement of quantum dot luminescence in plasmonic metamaterials. *Phys. Rev. Lett.*, 105(22):227403, 2010.

[Tre05]     S. A. Tretyakov. Research on negative refraction and backward-wave media: A historical perspective. *EPFL Latsis Symposium, Lausanne*, 2005.

[TSJ02]     S. Tretyakov, A. Shivola, and B. Jancewicz. Onsager-Casimir principle and the constitutive relations of bi-anisotropic media. *J. Electromagn. Waves Appl.*, 16(4):573–578, 2002.

[TSS09]     E. Tatartschuk, E. Shamonina, and L. Solymar. Plasmonic excitations in metallic nanoparticles: Resonances, dispersion characteristics and near-field patterns. *Opt. Express*, 17(10):8447–8460, 2009.

[TW97]      J. Turunnen and F. Wyrowski. *Diffractive Optics*. Akademie Verlag, Berlin, 1997.

[Ves68]     V. G. Veselago. The electrodynamics of substances with simultaneously negative values of $\epsilon$ and $\mu$. *Sov. Phys. Usp.*, 10(4):509–514, 1968.

[VH02]      T. Vallius and M. Honkanen. Reformulation of the Fourier modal method with adaptive spatial resolution: Application to multilevel profiles. *Opt. Express*, 10(1):24–34, 2002.

[VZZ+08]    J. Valentine, S. Zhang, T. Zentgraf, E. Ulin-Avila, D. A. Genov, G. Bartal, and X. Zhang. Three-dimensional optical metamaterial with a negative refractive index. *Nature*, 455(7211):376–379, 2008.

[WAM+08]    C. R. Williams, S. R. Andrews, S. A. Maier, A. I. Fernandez-Dominguez, L. Martin-Moreno, and F. J. Garcia-Vidal. Highly confined guiding of terahertz surface plasmon polaritons on structured metal surfaces. *Nature Photon.*, 2(3):175–179, 2008.

[WPT+10]    S. Wuestner, A. Pusch, K. L. Tsakmakidis, J. M. Hamm, and O. Hess. Overcoming losses with gain in a negative refractive index metamaterial. *Phys. Rev. Lett.*, 105(12):127401, 2010.

[XDK+10]    S. Xiao, V. P. Drachev, A. V. Kildishev, X. Ni, U. K. Chettiar, H.-K. Yuan, and V. M. Shalaev. Loss-free and active optical negative-index metamaterials. *Nature*, 466(7307):735–738, 2010.

[Yan66]    C. C. Yan. Can the macroscopic Maxwell equations be obtained from the microscopic Maxwell-Lorentz equations by performing averages? *Found. Phys.*, 14(3):302–307, 1966.

[Yee66]    K. S. Yee. Numerical solution of initial boundary value problems involving Maxwell's equations in isotropic media. *IEEE Trans. Antenn. Propag.*, 25(3):491–502, 1966.

[ZCZ99]    F. Zheng, Z. Chen, and J. Zhang. A finite-difference time-domain method without the courant stability conditions. *IEEE Microw. Guid. Wave Lett.*, 9(11):441–443, 1999.

[ZDU+08]    X. Zhang, M. Davanco, Y. Urzhumov, G. Shvets, and S. R. Forrest. From scattering parameters to snell's law: A subwavelength near-infrared negative-index metamaterial. *Phys. Rev. Lett.*, 101(26):267401, 2008.

[ZDW+09]    J. Zhou, J. Dong, B. Wang, T. Koschny, M. Kafesaki, and C. M. Soukoulis. Negative refractive index due to chirality. *Phys. Rev. B*, 79(12):121104(R), 2009.

[ZFM+05]    S. Zhang, W. Fan, K. J. Malloy, S. R. Brueck, N. C. Panoiu, and R. M. Osgood. Near-infrared double negative metamaterials. *Opt. Express*, 13(13):4922–4930, 2005.

[ZFP+05]    S. Zhang, W. Fan, N. C. Panoiu, K. J. Malloy, R. M. Osgood, and S. R. J Brueck. Experimental demonstration of near-infrared negative-index metamaterials. *Phys. Rev. Lett.*, 95(13):137404, 2005.

[ZHL+09]    Y. Zeng, W. Hoyer, J. Liu, S. W. Koch, and J. V. Moloney. Classical theory for second-harmonic generation from metallic nanoparticles. *Phys. Rev. B*, 79(23):235109, 2009.

[ZHSM10]    W. Zhang, L. Huang, C. Santschi, and O. J. F. Martin. Trapping and sensing 10 nm metal nanoparticles using plasmonic dipole antennas. *Nano Lett.*, 10(3):1006–1011, 2010.

[ZNG09]    S. V. Zhukovsky, A. V. Novitsky, and V. M. Galynsky. Elliptical dichroism: Operating principle of planar chiral metamaterials. *Opt. Lett.*, 34(13):1988–1990, 2009.

# 9 List of Figures

XXVIII

*From a long view of the history of mankind - seen from, say, ten thousand years from now, there can be little doubt that the most significant event of the 19th century will be judged as Maxwell's discovery of the laws of electrodynamics.*

R. P. Feynman, *The Feynman Lectures on Physics, Vol. II, 1964.*